SLAC–345
UC–34D
(E)

HADRONIC DECAYS OF THE D_s MESON*

Steven R. Wasserbaech

Stanford Linear Accelerator Center
Stanford University
Stanford, California 94309

June 1989

Prepared for the Department of Energy
under contract number DE–AC03–76SF00515

* Ph.D. thesis.

Abstract

The D_s^+ (formerly F^+) is the lowest-lying pseudoscalar meson containing charm and anti-strange quarks. Evidence for this state was first reported in 1977, although more recent observations disagree with some of the early results. Since 1983 the weakly decaying D_s^+ has been observed in many experiments. Relative branching fractions have been measured for many non-leptonic decay modes, including $D_s^+ \to \phi\pi^+$, $\phi\pi^+\pi^+\pi^-$, $\bar{K}^{*0}K^+$, and $f_0(975)\pi^+$. The absolute branching fractions are estimated in high energy e^+e^- annihilation from the observed numbers of reconstructed D_s^+ decays and the expected D_s^+ production cross section. The lowest-lying vector $c\bar{s}$ meson, the D_s^{*+}, has also been seen in its decay to γD_s^+.

Weak decays of the heavy quark and lepton flavors are relevant to the development of the Standard Model of both the electroweak and the strong interactions. The Weinberg-Salam theory has been enormously successful in describing electroweak processes. However, the theory of strong interactions is complicated by the phenomenon of color confinement, which leads to the breakdown of perturbation theory at low energies (long distances). Measurements of charmed particle weak decays are useful for determining the parameters of the Standard Model and for testing phenomenological models which include strong effects. Information about exclusive

charm branching fractions is also important for the study of bottom particles.

In this thesis hadronic decays of the D_s^+ meson are studied in a sample of e^+e^- annihilation events at a center-of-mass energy of 4.14 GeV. The data were collected with the Mark III detector at the SPEAR storage ring of the Stanford Linear Accelerator Center. Production of D_s^+ at this energy is found to be dominated by the reaction $e^+e^- \to D_s^{*\pm}D_s^{\mp}$. The D_s^+ and D_s^{*+} masses are measured, and the cross section $\times$ branching fractions for $D_s^+ \to \phi\pi^+$ and $D_s^+ \to \bar{K}^{*0}K^+$ are obtained. A search is made for fully reconstructed $e^+e^- \to D_s^{*\pm}D_s^{\mp}$ events in a large number of final states. No significant evidence for such events is found, allowing limits to be established on the absolute branching fractions for $D_s^+ \to \phi\pi^+$, $\eta\pi^+$, and $\eta'\pi^+$.

Acknowledgements

The analysis of Section 4.2 was performed in conjunction with Walter Toki and Tim Freese.

I would like to thank my many colleagues in the Mark III Collaboration, past and present, who made this work possible by designing, building, and maintaining the experiment, by writing and taking care of the software, and by establishing a very pleasant environment in which to work.

I am grateful to my advisor, Walter Toki, for giving me many opportunities to develop my skills, and for providing the guidance I needed to keep things in perspective and stay on the right track. Thanks for everything.

Dennis Wisinski, Karen Heidenreich, and Ramon Berger get special recognition for taking good care of our data and keeping us all on line. (In line?)

I has been a pleasure to work with Tim Freese, Peter Kim, Dale Pitman, Bill Wisniewski, Al Odian, Basil Tripsas, Arla Li, Gregory Dubois, Usha Mallik, Tim Bolton, Wolfgang Stockhausen, Bill Lockman, Fritz DeJongh, Christoph Grab, Larry Parrish, Rafe Schindler, Bill Wadley, Effie Clewis, Lupé Salgado, Sharon Haynes, and many others!

Also, thanks to Tim Freese for running all those REPROCs.

Thanks to my parents, Rudi and Johanna, for all they've done to make this possible.

Above all I would like to thank my wife, Renée, for her patience, generosity, and love.

The Mark III Collaboration, 1980–89

J. Adler, Z. Bai, R.M. Baltrusaitis, J.J. Becker, G.T. Blaylock, H. Bledsoe, T. Bolton, J.-C. Brient, T.E. Browder, J.S. Brown, K.O. Bunnell, M. Burchell, T.H. Burnett, R.E. Cassell, D. Coffman, V. Cook, D.H. Coward, H. Cui, S. Dado, F. DeJongh, C. Del Papa, D.E. Dorfan, J. Drinkard, G.P. Dubois, A.L. Duncan, G. Eigen, K.F. Einsweiler, B.I. Eisenstein, R. Fabrizio, D. Favart, T. Freese, C. Gatto, G. Gladding, C. Grab, F. Grancagnolo, B. Haber, R.P. Hamilton, J. Hauser, C.A. Heusch, D.G. Hitlin, D. Hutchinson, J.M. Izen, P.C. Kim, J. Kohlmeier, L. Köpke, J. Labs, A.D. Li, W.S. Lockman, H. Lubatti, U. Mallik, C.G. Matthews, A.I. Mincer, R. Mir, P.M. Mockett, K. Moriyasu, L. Moss, R.F. Mozley, A. Nappi, B. Nemati, A. Odian, L. Parrish, R. Partridge, J. Perrier, D. Pitman, S.A. Plaetzer, J.D. Richman, M. Roco, J.R. Roehrig, J. Rothberg, J.J. Russell, H.F.-W. Sadrozinski, M. Scarlatella, T.L. Schalk, R.H. Schindler, A. Seiden, C. Simopoulos, J.C. Sleeman, D.B. Smith, A.L. Spadafora, I.E. Stockdale, W. Stockhausen, J.J. Thaler, W. Toki, B. Tripsas, Y. Unno, F. Villa, M.Z. Wang, S. Wasserbaech, A. Wattenberg, A.J. Weinstein, N. Wermes, S. Weseler, H.-J. Willutzki, D.E. Wisinski, W.J. Wisniewski, G. Wolf, R. Xu, Y. Zhu

California Institute of Technology, Pasadena, CA 91125
University of California at Santa Cruz, Santa Cruz, CA 95064
University of Illinois at Urbana-Champaign, Urbana, IL 61801
University of Iowa, Iowa City, IA 52242
Stanford Linear Accelerator Center, Stanford, CA 94309
University of Washington, Seattle, WA 98195

Contents

List of Tables

List of Figures

1
Introduction

1.1 The Standard Model

The remarkable theoretical advances of the past thirty years have led to the development of the Standard Model of electromagnetic, weak, and strong interactions. The elementary particles of the model are the quarks, leptons, and gauge bosons; their electromagnetic and weak interactions are well described in a single unifying gauge field theory. The strong forces are also treated within the framework of gauge theory. However, the mutual interactions of the massless gluons lead to a breakdown of perturbation theory at low energies which is detrimental to the predictive powers of the model.

The foundation of the Standard Model is the hypothesis that the vast collection of observed hadron states is generated by combinations of a small number of quark flavors: up, down, strange, charm, and bottom. The discovery of a sixth, evidently very heavy quark flavor, top, is (still) eagerly anticipated. The quarks are fractionally charged: $+\frac{2}{3}$ for u, c, t and $-\frac{1}{3}$ for d, s, b. In addition there are three families of integer-charged leptons, particles which do not participate in the strong interactions.

The Standard Model of electroweak interactions[1–3] is a local gauge theory based on the symmetry group $SU(2) \times U(1)$. In this model, the gauge fields W_μ^1, W_μ^2, W_μ^3 of $SU(2)$ and B_μ of $U(1)$ mix to produce the physical γ, Z^0, and $W^\pm$ boson fields. Left-handed quark and lepton fields form $SU(2)$ ("weak isospin") doublets:

$$\psi_i = \begin{bmatrix} \nu_e \\ e^- \end{bmatrix}_L, \quad \begin{bmatrix} \nu_\mu \\ \mu^- \end{bmatrix}_L, \quad \begin{bmatrix} \nu_\tau \\ \tau^- \end{bmatrix}_L, \quad \begin{bmatrix} u \\ d' \end{bmatrix}_L, \quad \begin{bmatrix} c \\ s' \end{bmatrix}_L, \quad \begin{bmatrix} t \\ b' \end{bmatrix}_L,$$

while the right-handed fermions are $SU(2)$ singlets. The weak quark eigenstates d', s', b' are related to the mass eigenstates d, s, b by the Kobayashi-Maskawa (K-M) matrix $\mathbf{V}$[4]:

$$\begin{bmatrix} d' \\ s' \\ b' \end{bmatrix} = \begin{bmatrix} V_{ud} & V_{us} & V_{ub} \\ V_{cd} & V_{cs} & V_{cb} \\ V_{td} & V_{ts} & V_{tb} \end{bmatrix} \begin{bmatrix} d \\ s \\ b \end{bmatrix}.$$

Assuming three quark generations, the following 90% confidence intervals for the moduli of the elements of $\mathbf{V}$ have been measured[5]:

$$\begin{bmatrix} 0.9748\text{–}0.9761 & 0.217\text{–}0.223 & 0.003\text{–}0.010 \\ 0.217\text{–}0.223 & 0.9733\text{–}0.9754 & 0.030\text{–}0.062 \\ 0.001\text{–}0.023 & 0.029\text{–}0.062 & 0.9980\text{–}0.9995 \end{bmatrix}.$$

The mixing of the first two quark generations was originally parametrized by a single angle,[3,6] now referred to as the Cabibbo angle. Charmed meson decays involving V_{cd} or V_{us} are said to be "Cabibbo suppressed," *i.e.*, the rates are reduced by roughly the factor $\tan^2 \theta_C = 0.05$ compared to the corresponding allowed decays.

In the "minimal" model, a complex doublet of Higgs fields is introduced to "spontaneously break" the $SU(2)$ symmetry of the Lagrangian and induce the $W^\pm$ and Z^0 masses (as well as the fermion masses), while preserving the renormalizability of the theory.[7] This construction implies the existence of a yet-unseen scalar state, the Higgs boson, whose mass is not predicted by the theory.

The $W^{\pm}$ coupling to fermions, the charged-current interaction, is described by the Lagrangian density

$$L_{CC} = -\frac{g}{2\sqrt{2}} \sum_i \bar{\psi}_i \gamma^\mu (1-\gamma^5)(T^+ W_\mu^+ + T^- W_\mu^-)\psi_i,$$

where g is the $SU(2)$ gauge coupling constant and $T^{\pm}$ are the weak isospin raising and lowering operators. That is, the W^+ couples to $e^+\nu_e$, $u\bar{d}'$, and so on. The $(1-\gamma^5)$ or $V-A$ (vector – axial-vector) structure selects only left-handed fermions (or right-handed anti-fermions).

The weak neutral-current interaction is characterized by the Lagrangian density

$$L_{NC} = -\frac{g}{2\cos\theta_W} \sum_i \bar{\psi}_i \gamma^\mu (V^i - A^i\gamma^5)\psi_i Z_\mu,$$

where is θ_W is the W_μ^3-B_μ mixing angle, and the vector and axial couplings V^i, A^i are different for u- and d-type quarks and charged and neutral leptons. It is important to note that the theory contains no first-order flavor-changing neutral currents.

The electroweak theory is a masterwork of theoretical physics, accurately describing such diverse phenomena as electromagnetism, nuclear beta decay, τ decays, and neutrino scattering. Its unqualified success was made even more impressive with the discovery in 1983 of the $W^{\pm}$ and Z^0 bosons—at the predicted masses.[8]

The gauge theory of strong interactions in the Standard Model is Quantum Chromodynamics (QCD). In this theory the quarks are assumed to carry "color charge" of three possible values. The idea that each quark flavor comes in three colors was first introduced to remove the apparent violation of Fermi statistics by the three u quarks in the $J=\frac{3}{2}$ ground state Δ^{++} baryon. The existence of three quark colors is also required to explain the observed cross section for $e^+e^- \rightarrow$ hadrons.

The strong interactions are mediated by eight types of massless gluons which couple to color. The Lagrangian is symmetric under SU(3) transformations among the three colors. Gluons themselves carry color; the gluon-gluon interactions lead to an effective QCD coupling constant α_s which is smaller at short distances ("asymptotic freedom" at higher momentum transfer Q^2), and hence to confinement of colored objects at low energies (such as within hadrons).[9] The leading-order dependence of α_s on Q^2 is given by

$$\alpha_s(Q^2) = \frac{12\pi}{(33 - 2n_f)\ln(Q^2/\Lambda^2)},$$

where n_f is the number quark flavors with mass less than Q, and the parameter $\Lambda \sim 200\,\mathrm{MeV}$ is determined from experiment. At the charm mass scale, $\alpha_s \sim 0.3$.[5] At lower Q^2 the coupling becomes too strong for perturbation methods to be used in the calculation of matrix elements.

1.2 Weak Decays of Charmed Mesons

The existence of the fourth quark flavor, charm, was first hypothesized in 1964.[10] The four-quark model was further developed to explain the observed suppression of second-order flavor-changing weak neutral currents, *e.g.* in $K_L^0 \to \mu^+\mu^-$.[3] The charmonium resonances J/ψ and $\psi(3685)$ were discovered in 1974,[11,12] and the charmed D^0 and D^+ mesons less than two years later.[13] Observation of the third ($c\bar{s}$) member of the expected $SU(3)$ triplet of charmed pseudoscalar states,[3,10,14] the D_s^+ meson (formerly the "F^+"), was first announced in 1977 by the DASP Collaboration.[15] Four $D_s^+ \to \eta\pi^+$ decays* (with negligible background) were seen in association with

* Throughout this thesis, reference to a particle state also implies reference to its charge conjugate.

low energy photons. The events were interpreted as $e^+e^- \to D_s^* D_s$, $D_s^* \to \gamma D_s$, where the D_s^* is the lowest-lying $c\bar{s}$ vector meson. A D_s mass of $2030 \pm 60\,\mathrm{MeV}/c^2$ was measured. However, the reported enhancement in the $e^+e^- \to \eta X$ cross section at $\sqrt{s} = 4.4\,\mathrm{GeV}$ was not confirmed.[16] The first undisputed observation of the D_s^+ was made by CLEO[17] in 1983; the mass was found to be $1970 \pm 5 \pm 5\,\mathrm{MeV}/c^2$.

Early predictions of the weak decay properties of $c\bar{q}$ mesons were based on the assumption that the $\bar{q}$ is simply a spectator to the $c \to s'W^+$ transition. In this picture the *external W-emission* diagram [Fig. 1.1(a)] is expected to dominate. The virtual W^+ can yield $e^+\nu_e$, $\mu^+\bar{\nu}_\mu$, or $u\bar{d}'$ (in three colors). The *internal W-emission* process [Fig. 1.1(b)] was expected to be suppressed because color matching of the quark lines is required for the formation of hadrons. The *flavor annihilation* diagrams of Fig. 1.1(c) and (d) are helicity suppressed at the light quark-W vertex. It follows that the lifetimes of the D^0, D^+, and D_s^+ should be roughly equal, with semi-electronic branching fractions of about 20% for each. The experimental results

$$\tau(D^0) \cong \tau(D_s^+) \cong 0.4\,\tau(D^+)$$

and

$$B(D^0 \to e^+X) = 7.7 \pm 1.1\%$$

$$B(D^+ \to e^+X) = 19.2\,^{+2.3}_{-1.6}\%$$

lead us to consider refinements to the simple spectator model.

Hard gluon exchange leads to important modifications of the amplitudes for the weak decay diagrams. The effective coupling strength is modified, and an effective flavor-changing neutral current is induced by the gluon interactions. This leads to a substantial amplitude for diagram (b) in which the quark colors are automatically matched. For example, the decay $D^0 \to \bar{K}^0\pi^0$ is observed at a comparable rate to

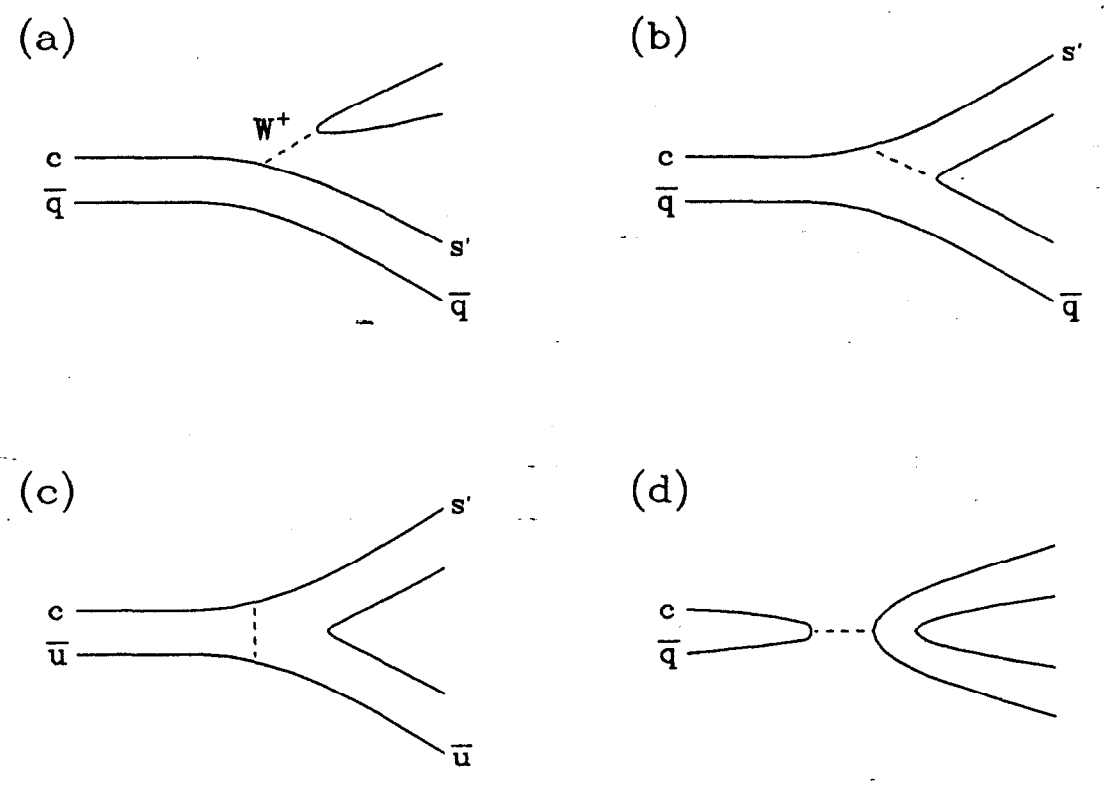

Figure 1.1 Charm weak decay processes: (a) external W-emission, (b) internal W-emission, (c) W-exchange (D^0 only), and (d) W-annihilation (D^+ and D_s^+ only). Gluon lines are not shown.

$D^0 \to K^-\pi^+$, although a suppression factor of 18 is estimated by color counting. However, these short-distance corrections should have the same effect for D^0, D^+, and D_s^+: an enhancement in the non-leptonic transition rates.

An important contribution to the lifetime differences is likely to come from destructive interference in the amplitudes for some D^+ modes.[18,19] For example, the decay $D^+ \to \bar{K}^0\pi^+$ may proceed through both types of diagrams, (a) and (b),

whereas $D^0 \to K^-\pi^+$ and $\bar{K}^0\pi^0$ have only one or the other diagram. The hard gluon corrections yield opposite algebraic signs for the two coefficients, so some cancellation is expected to occur in D^+ modes of this type. Indeed, the partial rates for $D^0 \to K^-\pi^+$ and $\bar{K}^0\pi^0$ are roughly three times larger than for $D^+ \to \bar{K}^0\pi^+$.

The *flavor annihilation* diagrams of Fig. 1.1(c) and (d) may also be partly responsible for the enhancement of the D^0 and D_s^+ decay rates, since the annihilation diagram for the D^+ is Cabibbo suppressed. The helicity suppression could be removed by QCD effects. However, no unambiguous evidence has been found for a non-spectator process occurring at a substantial rate. The decay $D^0 \to \bar{K}^0\phi$ was suggested as a signature for flavor annihilation[20] and later observed with nearly a 1% branching fraction,[21] but the possibility exists that this channel arises from final state interactions in an ordinary spectator decay mode.[19,22] The D_s^+ annihilation decays to $\rho^0\pi^+$ and $\omega\pi^+$ are not observed,[23–25] suggesting that non-spectator processes are not predominantly responsible for the observed lifetime differences.

1.3 D_s^*-D_s Mass Difference

The mass difference between vector and pseudoscalar $q_1\bar{q}_2$ states may be predicted from the spin-spin contact potential

$$\begin{aligned} \Delta V &= \frac{8\pi\alpha_s}{9}\frac{\vec{\sigma}_1\cdot\vec{\sigma}_2}{m_1 m_2}\,|\psi(0)|^2\,, \\ M(1^-) - M(0^-) &\cong \langle 1^-|\Delta V|1^-\rangle - \langle 0^-|\Delta V|0^-\rangle \\ &\cong \frac{32\pi\alpha_s}{9m_1m_2}\,|\psi(0)|^2 \equiv \frac{C}{m_1m_2}. \end{aligned}$$

Using the quark masses $m_u = 0.39\,\mathrm{GeV}/c^2$, $m_s = 0.51\,\mathrm{GeV}/c^2$, $m_c = 1.6\,\mathrm{GeV}/c^2$,

and assuming C to be constant, we expect

$$M(D_s^{*+}) - M(D_s^+) = \frac{m_u m_s}{m_c m_s}[M(K^{*0}) - M(K^0)] = 97\,\mathrm{MeV}/c^2.$$

However, for a linear confining potential, $|\psi(0)|^2 \propto m_1 m_2/(m_1+m_2)$,[26] which leads to

$$M(1^-) - M(0^-) \propto \frac{1}{m_1 + m_2}$$

or

$$M^2(1^-) - M^2(0^-) \sim \text{constant},$$

neglecting the mass dependence of α_s. This yields the prediction

$$M(D_s^{*+}) - M(D_s^+) = \frac{m_u + m_s}{m_c + m_s}[M(K^{*0}) - M(K^0)] = 170\,\mathrm{MeV}/c^2.$$

By considering the dependence of α_s on Q^2, and using particular forms for the potential, the mass difference

$$M(D_s^{*+}) - M(D_s^+) = 132 \pm 6\,\mathrm{MeV}/c^2$$

is obtained.[27]

The D_s^{*+} is expected to decay predominantly to γD_s^+[14]; the $\pi^0 D_s^+$ channel is forbidden by isospin conservation (if not by energy conservation). Throughout this thesis I assume $B(D_s^{*+} \to \gamma D_s^+) = 100\%$.

1.4 Experimental Status of the D_s^+ and D_s^{*+} in 1985

In this section I review the D_s and D_s^* experimental results which were available at the time the Mark III Collaboration began its D_s^+ program in 1985. As mentioned earlier, the D_s^+ was reliably identified in 1983. As of fall 1985, the D_s^+ had been

observed in the final states $\phi\pi^+$,[17,28,29,30] $\phi\pi^+\pi^+\pi^-$,[31] and inclusive $K^+K^-\pi^+$.[32,33] The only relative branching fraction measurement was[31]

$$B(D_s^+ \to \phi\pi^+\pi^+\pi^-)/B(D_s^+ \to \phi\pi^+) = 1.11 \pm 0.37 \pm 0.28\,.$$

Further evidence for the D_s^* was reported in 1984 by ARGUS[29] and TPC.[33] The decay $D_s^{*+} \to \gamma D_s^+$ was reconstructed in both experiments. The measurements of $M(D_s^*) - M(D_s)$ were $144 \pm 9 \pm 7\,\mathrm{MeV}/c^2$ and $139.5 \pm 8.3 \pm 9.7\,\mathrm{MeV}/c^2$, respectively. These results are consistent with the prediction of Reference 27.

1.5 Objectives

The objectives of the Mark III run of 1985–86 at $\sqrt{s} = 4.14\,\mathrm{GeV}$ included:

1. confirmation of the D_s^{*+},
2. precise measurement of the D_s^+ and D_s^{*+} masses,
3. measurement of σB for as many D_s^+ decay modes as possible.

The continuous D_s^+ momentum spectrum arising from $e^+e^- \to D_s^{*+}D_s^{*-}$ is not favorable for isolating D_s^+ decays or measuring the D_s^{*+} mass. The center-of-mass energy for the run was therefore selected, based on the available information, to be above threshold for $e^+e^- \to D_s^{*\pm}D_s^{\mp}$ ($\sim 4.08\,\mathrm{GeV}$), but below threshold for $e^+e^- \to D_s^{*+}D_s^{*-}$ ($\sim 4.22\,\mathrm{GeV}$). The earlier D_s^{*+} mass measurements were indeed confirmed by our results.

The experimental apparatus is described in Chapter 2. Chapter 3 contains several analysis topics, including the data sample, the event reconstruction procedure, checks of detector performance, and event simulation. The $D_s^+ \to \phi\pi^+$ mode was used to accomplish the first two of our objectives; these results are detailed in

Chapter 4. A measurement of $D_s^+ \to \bar{K}^{*0}K^+$ is shown in Chapter 5. A study of absolute D_s^+ hadronic branching fractions is described in Chapter 6. The results and conclusions are given in Chapter 7.

2
The Mark III Detector

2.1 The Mark III Detector at SPEAR

SPEAR

The Mark III detector occupies the west interaction region of the e^+e^- storage ring SPEAR* at the Stanford Linear Accelerator Center. Construction of SPEAR was completed in 1972.[35] The layout of the ring is shown in Fig. 2.1. The machine was designed to operate in the 3 to 5 GeV center-of-mass energy range. An upgrade to the RF accelerating system was made in 1974 to increase the energy limit to 8 GeV. "Mini-β" optics[36] were installed in 1984, but the expected four-fold increase in luminosity was not achieved.

Electrons and positrons are supplied by the two-mile linear accelerator for injection into SPEAR. Kicker magnets are used to momentarily deform the orbit of the stored beam while new particles are deposited into the same RF "bucket." One species is injected at a time. Under good conditions, the beams could be "topped off" in 5 minutes. The data collection runs were typically three hours long.

---

* The Stanford Positron-Electron Asymmetric Ring was originally designed to have an ovoid shape, with the spacing between the two interaction points not equal to half the ring circumference. See Reference 34.

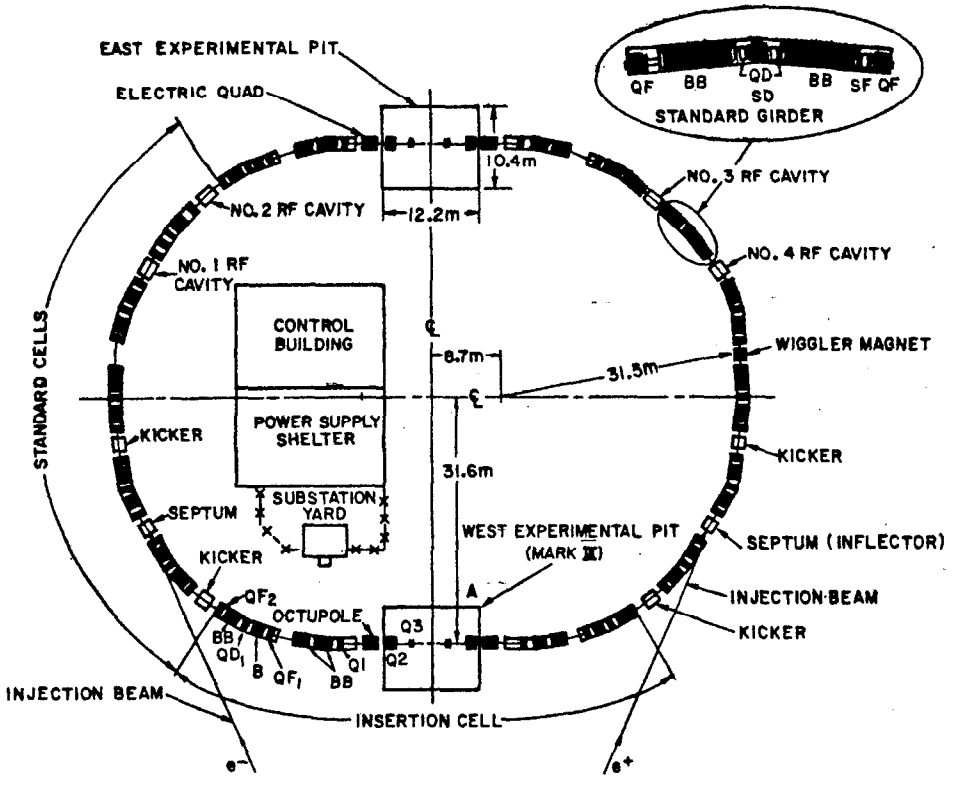

Figure 2.1 The Stanford Positron-Electron Asymmetric Ring. The circumference of the machine is 234 m.

Online luminosity estimates are obtained by counting small-angle (~ 30 mrad) Bhabha scattering events with tungsten/scintillator shower counters which are installed on the beam pipe in the east interaction region of SPEAR.† During the 1985–86 Mark III running cycle at $\sqrt{s} = 4.14$ GeV, a peak luminosity of 3×10^{30} cm^{-2}s^{-1} was achieved with beam currents of 12–15 mA.

The e^+e^- center-of-mass energy is calculated from the magnetic field of a reference bend magnet which is located in the SPEAR power supply shelter. This reference magnet is identical to the magnets in the ring, and is connected in series

† A similar set of counters in the west interaction region were not usable because of radiation damage to the light pipes. For cross section measurements the integrated luminosity is determined from large-angle Bhabha and dimuon events observed in the Mark III detector.

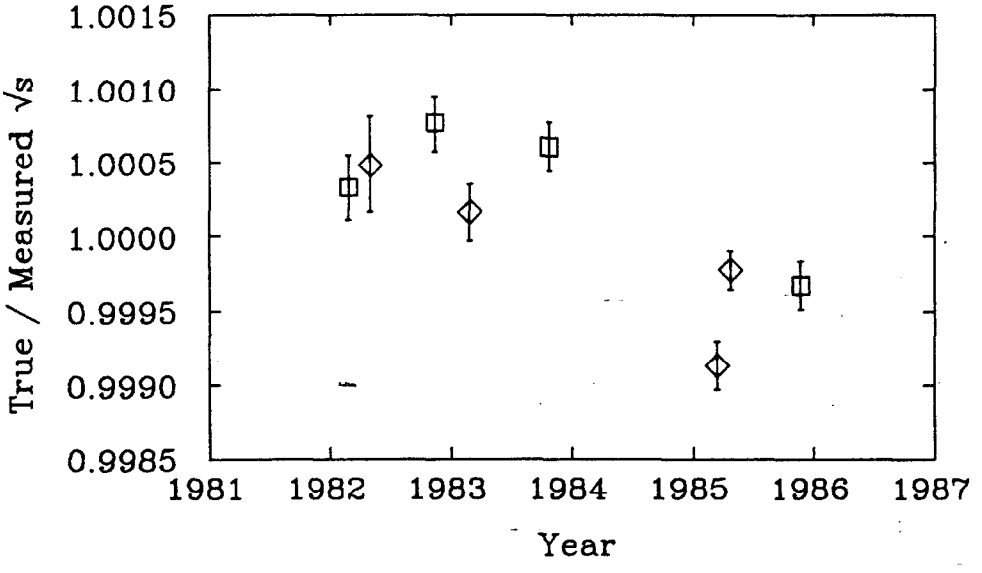

Figure 2.2 True / Measured SPEAR center-of-mass energy from scans of the J/ψ (diamonds) and $\psi(3685)$ (squares).

with them. A long rectangular coil is rotated back and forth within the reference magnet and the induced current is integrated over each half-turn. Variations in the orbit size (measured with beam position monitors) and the fields of corrector bend magnets are accounted for in the determination of the center-of-mass energy. The calibration of the energy scale is based on energy scans over the J/ψ and $\psi(3685)$ resonances. During such a scan the e^+e^- hadronic cross section is monitored online with the Mark III detector to determine the flip-coil reading which corresponds to the well-measured resonance masses.[5] The scan results since 1982 are plotted in Fig. 2.2. In 1984 the flip-coil electronics failed. After the repairs a new energy scale was found. During the 1985 J/ψ run the calibration suddenly changed again. No explanation for this was found, and stable readings on the resonance were obtained before and after the change. The last two scans in the plot are used to determine the relationship between the true and measured center-of-mass energy for the 1985–86

run, assuming the linear relationship

$$\sqrt{s_{\rm true}} = a_0 + a_1\sqrt{s_{\rm meas}}.$$

There is no significant evidence for $a_0 \neq 0$. A correction of $+0.08 \pm 0.36\,\mathrm{MeV}$ is applied to the flip-coil energy to account for the measured variations in magnetic field *vs.* current for the SPEAR bend magnets relative to the reference bend.[37] The result of the calibration is

$$\sqrt{s_{\rm true}} = 2.01\,\mathrm{MeV} + 0.99915\sqrt{s_{\rm meas}}.$$

The mean center-of-mass energy for the data set was 4.1392 GeV, with a systematic uncertainty of $\pm 1.7\,\mathrm{MeV}$ and an RMS deviation of 0.9 MeV.

The Mark III Detector

The Mark III detector is a descendent of the illustrious SLAC-LBL ("Mark I") spectrometer which was operated at SPEAR from 1973 to 1976. The Mark III design is optimized for the study of charm physics in e^+e^- annihilation in the 3 to 5 GeV energy range. The detector features large solid angle coverage for charged and neutral tracks, good particle identification capabilities, and high efficiency for detecting low energy photons. Installation at SPEAR was completed in 1981.

The Mark III detector is a conventional solenoidal spectrometer.[38] End and side views of the apparatus are shown in Figs. 2.3 and 2.4. The beams are carried through the interaction region in a beryllium pipe 15 cm in diameter, with 1.5 mm thick walls. A small trigger chamber surrounding the beam pipe was inoperative during the collection of the data sample under study. A new vertex detector[39] has since been installed in its place. Charged particles are tracked in the main

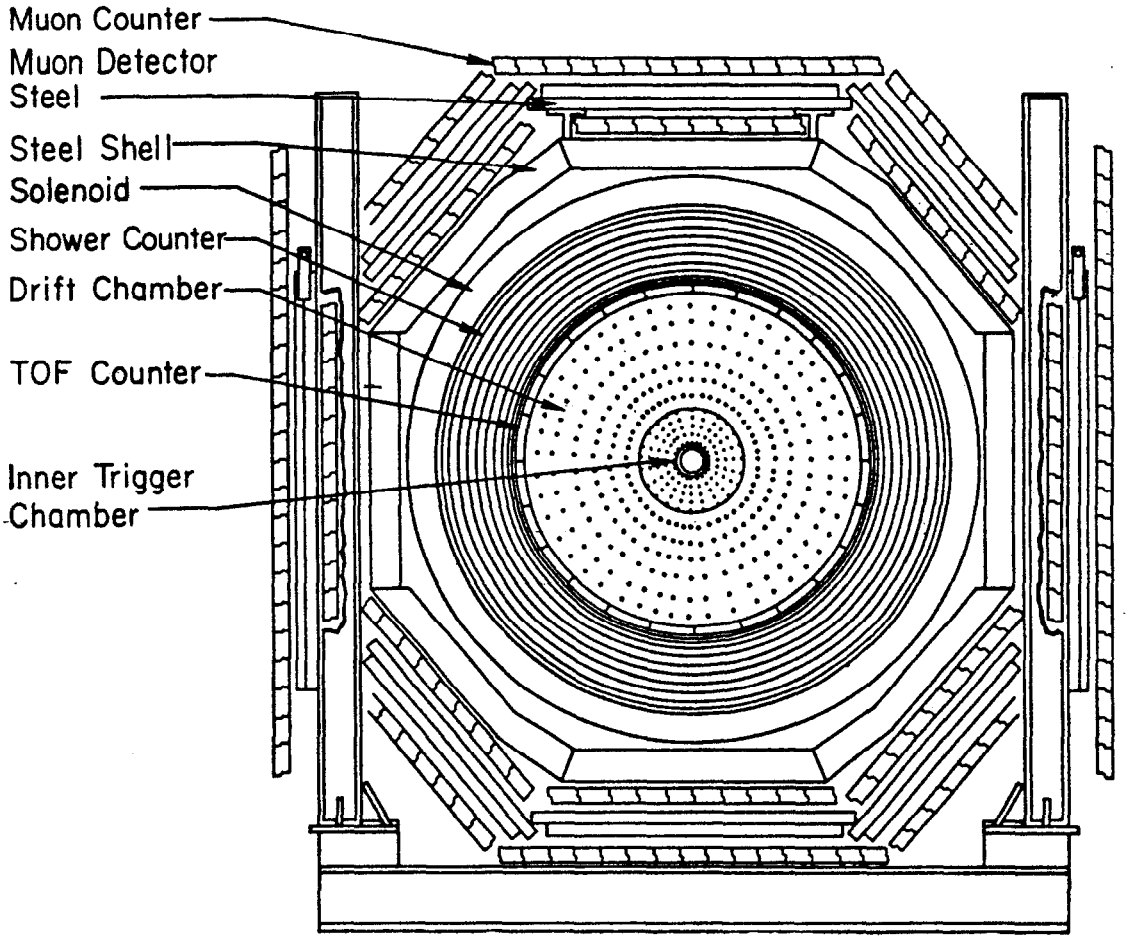

Figure 2.3 End view of the Mark III detector.

drift chamber.[40] Particle identification is derived from time of flight (TOF) measurements provided by a system of scintillation counters outside of the main drift chamber.[41] Electromagnetic calorimeters are found beyond the TOF system and on the endcaps.[42] These components are located within an aluminum coil which produces a 0.4 T solenoidal magnetic field for measuring charged track momenta. The outermost detector component is the muon detection system, which consists of two layers of proportional tubes separated by steel plates to absorb hadrons. Data acquisition is managed by a VAX 11/780 computer. "Brilliant" analog-to-digital

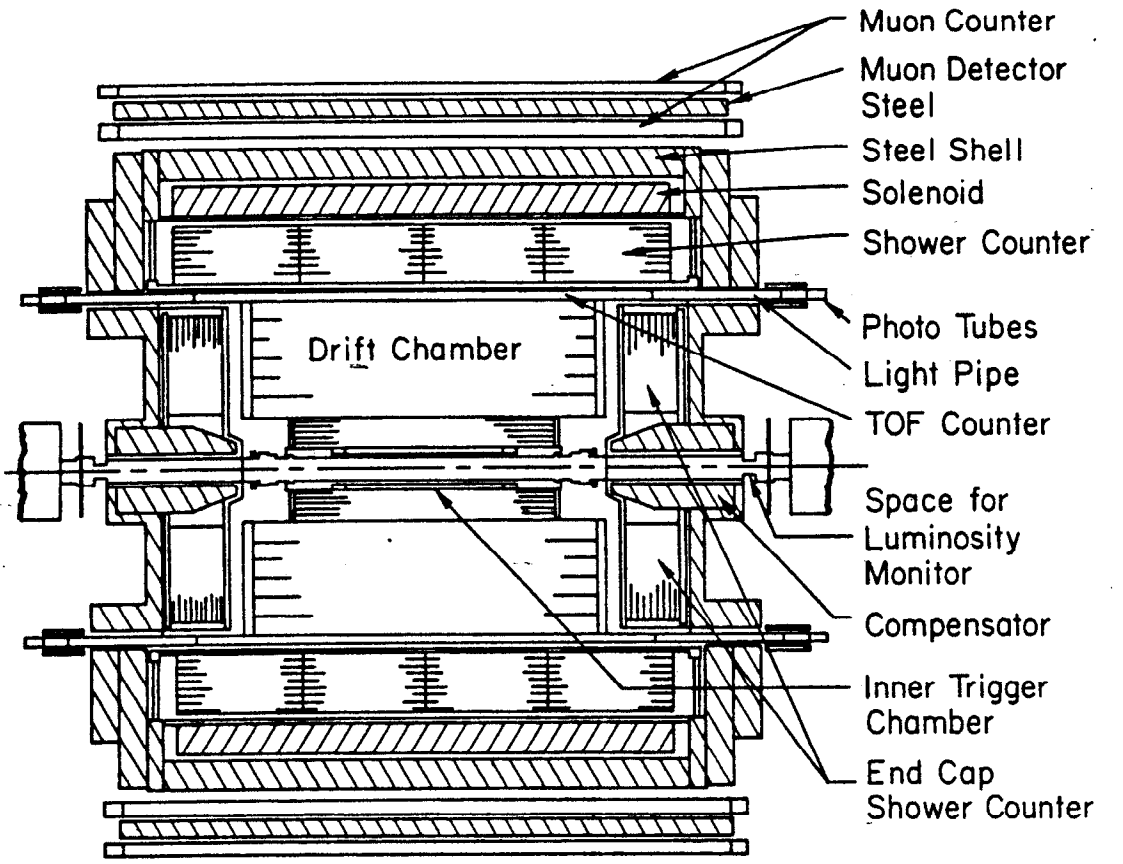

Figure 2.4 Side view of the Mark III detector.

converter modules (BADCs) are used to digitize signals from the various detector components and to apply pedestal and gain corrections to the data before delivery to the VAX. A hardware trigger system generates interrupts for logging events to tape, while rejecting cosmic ray and beam-gas scattering backgrounds to minimize dead time.[43] Samples of the incoming events are analyzed online to provide continuous monitoring of the operation of detector.

Detailed descriptions of the major components are given in the following sections. Detector performance is discussed in Chapter 3.

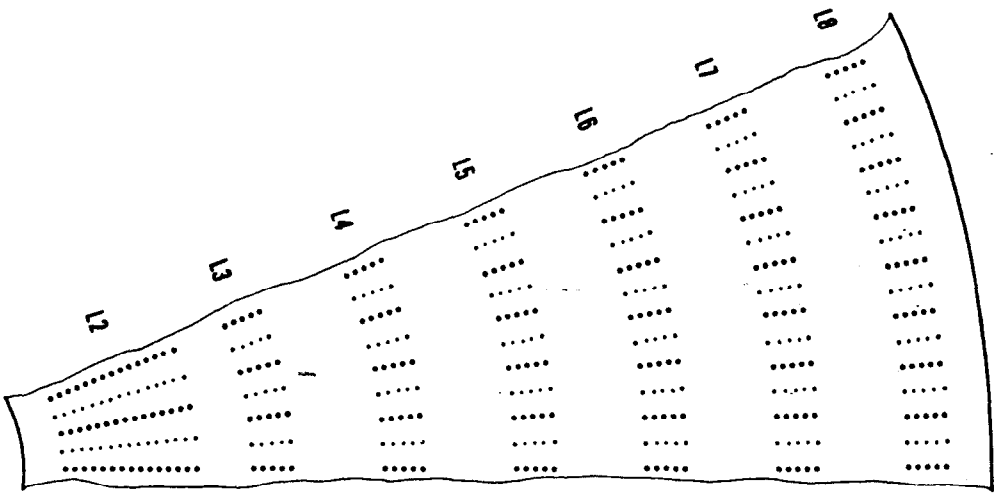

Figure 2.5 One of sixteen identical sectors of an endplate of the main drift chamber, showing the arrangement of the layers of cells. Field wires are shown as large dots, sense wires as small dots, and guard wires as open circles.

2.2 Main Drift Chamber

The main drift chamber consists of seven layers of tracking cells, covering a solid angle of 85% of 4π sr. The arrangement of the cells has a sixteen-fold azimuthal symmetry; a section of a chamber endplate is shown in Fig. 2.5. The layers are numbered (inner to outer) from 2 to 8. (The deceased trigger chamber was referred to as layer 1.) Sense wires are located between 18.4 and 108.6 cm from the beam axis, providing up to 30 drift time measurements for tracking. The length of the chamber is 1.78 m in layer 2, and 2.34 m in layers 3 through 8. The outside diameter is 2.29 m. The number of cells in layer n is $16 \times n$.

Layer 2 cells each contain twelve instrumented sense wires. Pulse heights on these wires are measured in addition to the drift times, providing energy loss measurements for particle identification. This information is not used in this thesis

because of the modest resolution: 3σ π-K separation is achieved only for $p < 0.4\,\mathrm{GeV}/c$.

Cells in layers 3 through 8 are 5.3 cm wide and contain three sense wires each. Layers 4 and 6 are stereo layers, inclined to the beam axis by +7.7 and −9.0 degrees, permitting reconstruction of charged track momenta in three dimensions.

Each cell in the chamber contains two grounded stainless steel guard wires 57 μm in diameter which help to shape the drift field. In layers 2, 3, 5, and 7 these wires are used to provide supplemental z measurements* by charge division.

Sense wires are 20 μm diameter tungsten. The drift fields are established with 175 μm diameter BeCu field wires maintained at negative high voltage. For the 1985–86 data cycle the chamber was filled with a gas mixture of 88.4% argon, 9.5% CO_2, 1.9% methane, and 0.2% water vapor. The gas gain was 2×10^4 in layer 2 and 2×10^5 in the outer layers.

To resolve the left-right ambiguity in the trajectories of tracks through the cells, sense wires are staggered by $\delta = \pm 400\,\mu$m ($\pm 150\,\mu$m in layer 2) in ϕ relative to the cell centerline. The quantity Δ is then used to determine which side of the cell was traversed:

$$\Delta \equiv V_{\mathrm{drift}}\,[(t_1 + t_3)/2 - t_2]\,,$$

where $V_{\mathrm{drift}} \sim 50\,\mu$m/ns and t_1, t_2, t_3 denote the measured drift times for a track passing the three sense wires of the cell. For tracks which do not cross the cell centerline we expect $\Delta = \pm 2\,|\delta|$. A histogram of Δ for layer 3 cells is shown in

---

* The Mark III coordinate system is defined as follows. The origin is at the interaction point. The $+x$-axis points toward the center of the ring (east). The $+y$-axis points upward. The $+z$-axis is along the e^+ beam direction (south). The polar angle θ and the azimuthal angle ϕ are defined in the usual way relative to the Cartesian coordinate axes. The dip angle λ is defined as $\pi/2 - \theta$.

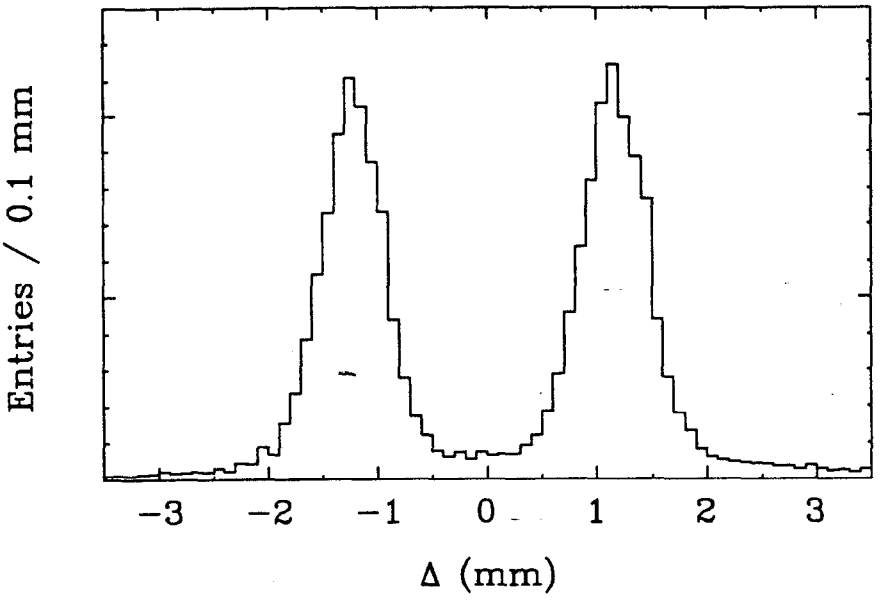

Figure 2.6 $\Delta \equiv V_{\rm drift}\,[(t_1 + t_3)/2 - t_2]$ distribution, showing separation of tracks passing on the left and right sides of the cells.

Fig. 2.6. The left-right ambiguity is easily resolved; the separation of the peaks is increased by the electrostatic interaction of the wires. The observed smearing corresponds to a tracking resolution of 235 μm per wire.

The drift chamber timing electronics are calibrated approximately three times daily during data taking. This involves pulsing each channel at various delay times and fitting a quadratic form to the measured time values. The relations so derived are then applied online to event data by the BADCs. Zero-times are obtained by fitting an error function shape to the raw time distribution for each wire. Time-to-distance relations for each of the 30 cylindrical layers of wires are derived from the residuals of helix fits to Bhabha scattering events.

The field of the solenoidal magnet was mapped before installation of the other

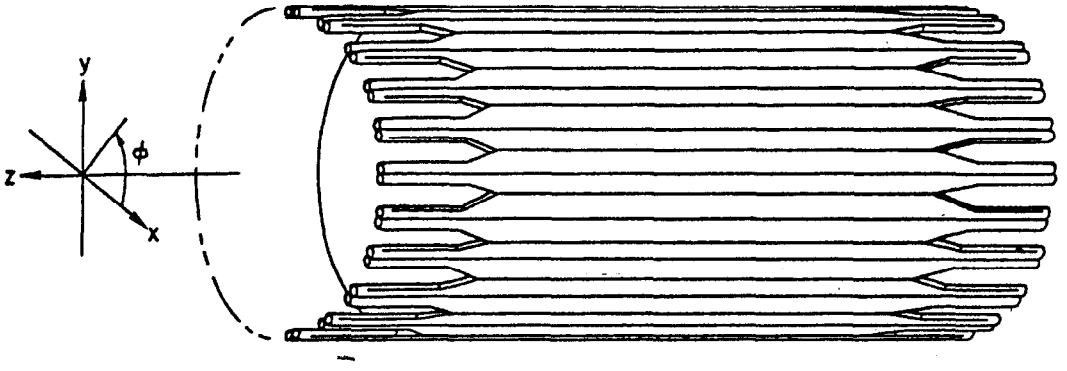

Figure 2.7 Time of flight scintillation counters and light guides.

detector components. Small corrections to the momentum scale are made, based on studies of $J/\psi \to p\bar{p}$, $K^0_S \to \pi^+\pi^-$, and $D \to \bar{K}\pi$, $\bar{K}\pi\pi$, $\bar{K}\pi\pi\pi$ from data taken since the mini-β installation in 1984.† The momentum scale uncertainty is 0.1%.

2.3 Time of Flight System

The time of flight system consists of 48 scintillation counters at a distance of 1.2 m from the beam axis, covering a solid angle of 80% of 4π. The scintillating material in each counter is 317.5 cm long, 15.6 cm wide, and 5.1 cm thick. Ultraviolet-transmitting plexiglass light guides join the scintillators to photomultiplier tubes located at each end, outside of the magnet iron. Fig. 2.7 shows the configuration of the counters surrounding the main drift chamber.

Phototube pulse times are simultaneously measured using two different thresholds. The beam-crossing time, derived from pick-off electrodes in the beam pipe near

† An NMR probe, located outside the barrel shower counter, is used to set the solenoid current. Changes made to the focusing and compensating magnets in 1984 altered the relationship between the field strengths at the origin and at the probe, necessitating a new offline calibration.

the detector, is used as the timing reference. The total charges of the pulses is also measured. A pulser is used to calibrate the timing electronics. Bhabha scattering events are used to determine (for each counter) the zero-times and the coefficients relating charge and z position to the measured time. Such a calibration is performed for blocks of runs corresponding to one to two days of data collection.

2.4 Electromagnetic Calorimeters

The barrel and endcap electromagnetic shower counters subtend a total of 94% of 4π sr. Each unit consists of 24 layers of proportional tubes separated by 0.28 cm (0.5 radiation length) Pb sheets. Pulse heights from the inner six layers are read out separately, while the remainder of the layers are summed radially in six groups of three. All wires are instrumented at both ends for position measurements along the wires by charge division. A gas mixture of 80% argon and 20% methane is used.

The barrel shower counter [Fig. 2.8] is located inside the magnet coil to maximize its efficiency for detecting low energy photons. It is constructed on an aluminum spool 3.85 m long and 2.52 m in diameter. The active region covers $|\cos\theta| < 0.76$. Each layer is divided azimuthally by aluminum I-beams into 320 proportional cells. The lead sheets which separate the layers are supported by five equally spaced aluminum bands 1.27 cm tall (radially) and 2.67 cm wide (axially) in each layer. These "ribs" are slotted to carry tensioned stainless steel straps which hold each layer together.

The endcap counters are mounted on 2.2 m diameter steel doors which fill the ends of the detector. The underside of each door is slotted to permit installation over the beamline; separate calorimeter modules fill the region below the beamline.

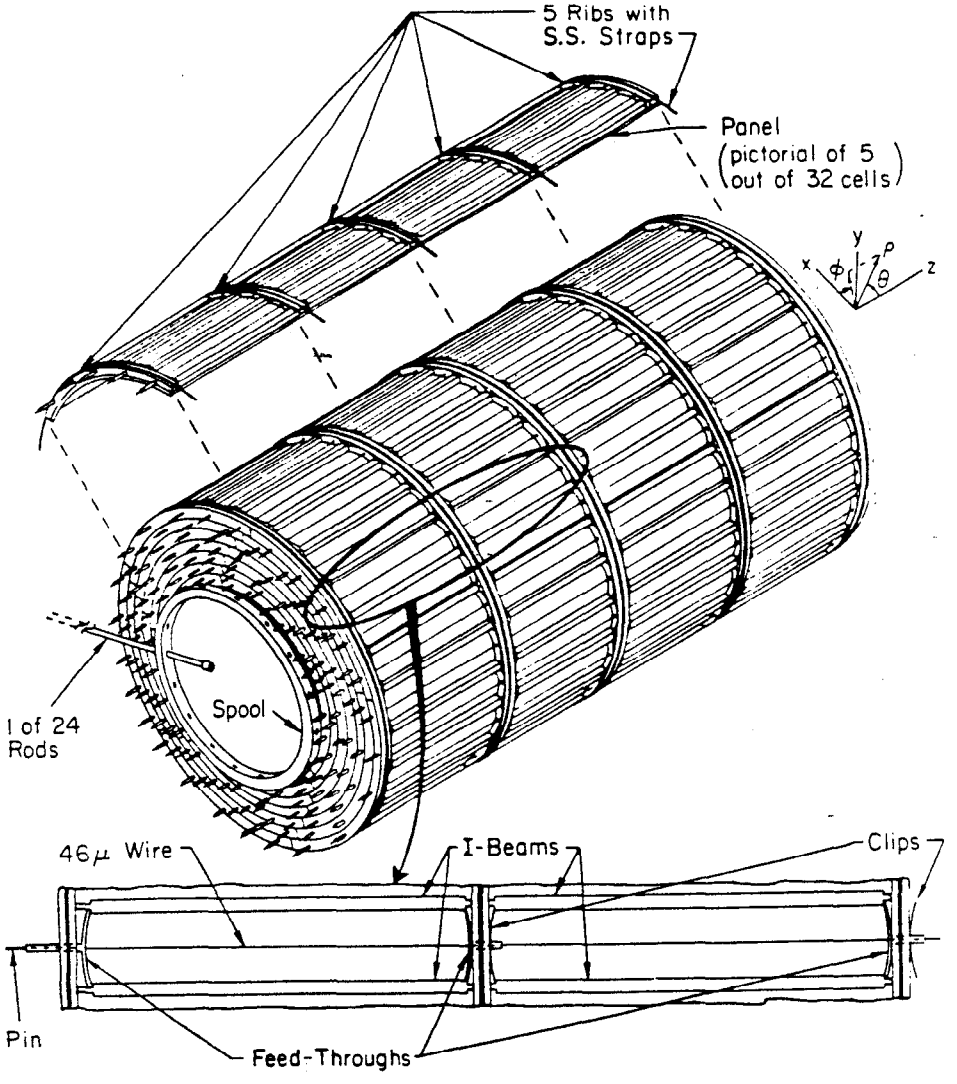

Figure 2.8 Barrel electromagnetic calorimeter.

The proportional cells are made from rectangular aluminum tubes, with each layer containing 94 vertical cells. The cell width of 2.84 cm subtends ~ 15 mrad at the interaction point.

The shower counter electronics are calibrated approximately three times daily

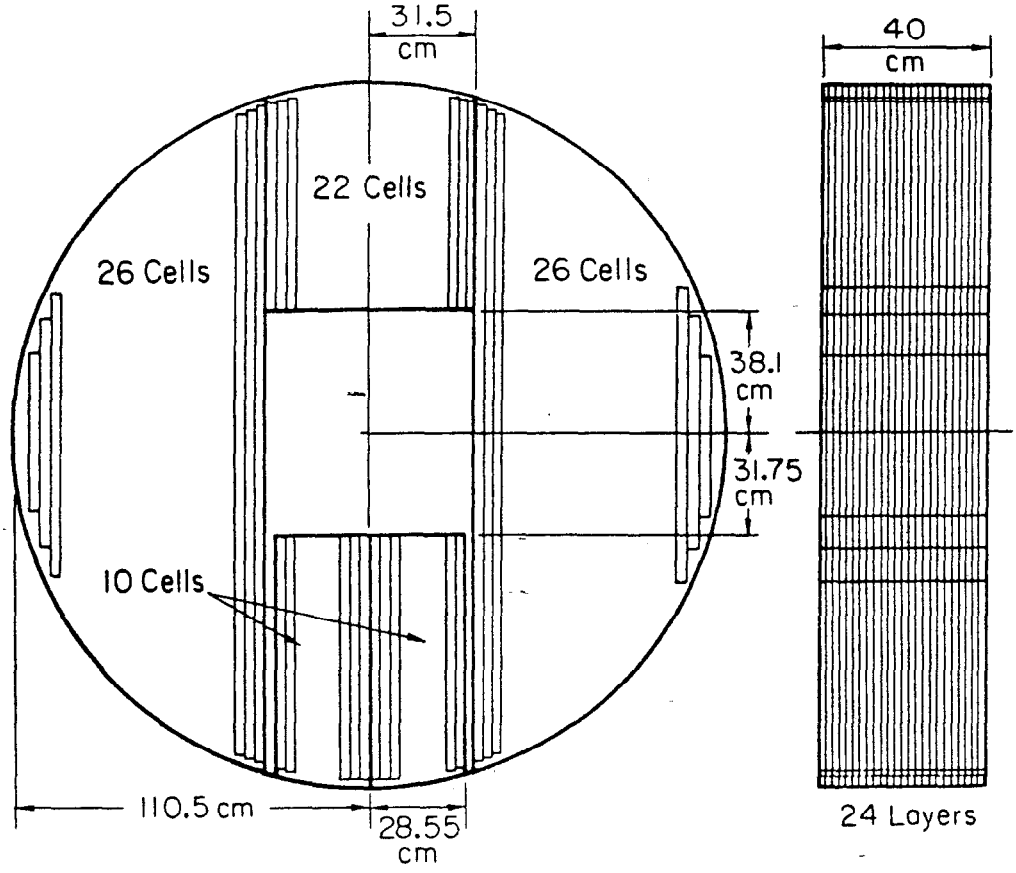

Figure 2.9 Endcap electromagnetic calorimeter.

by injecting pulses of particular amplitudes into the amplifier of each channel. In addition, the pedestals are measured before each data collection run. Gas gain corrections for pressure and temperature are applied. Adjustment of the absolute energy scale as a function of position along the sense wires is done using Bhabha scattering events [Fig. 2.10]. Allowance is made for different gains of the two batches of gas which were used during the 1985–86 run.

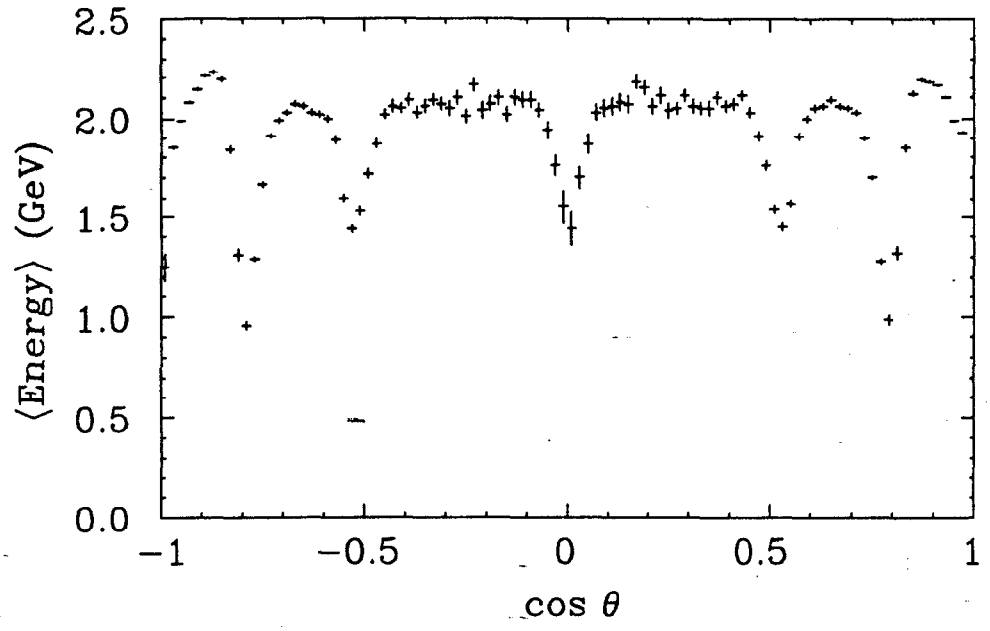

Figure 2.10 Mean reconstructed shower counter energy E *vs.* $\cos\theta$ for $e^{\pm}$ tracks in Bhabha scattering events. Showers near the edges of the endcaps ($|\cos\theta| \sim 0.8$) are not completely contained in the sensitive volume. The other depressions are caused by the ribs in the barrel.

2.5 Muon Detection System

In this thesis, the muon detection system is used to isolate dimuon events for various detector checks and for determining the total integrated luminosity of the data set. The system consists of 1080 proportional tubes 5 cm in diameter and 4.2 m long. The tubes are arranged in two layers, covering a solid angle of 65% of 4π sr. Charge division is used to measure the z positions of muon hits.

2.6 Event Trigger

The trigger system uses drift chamber and TOF information in a two level scheme. The following description applies to the configuration used in 1985–86.

The beam crossing rate at SPEAR is 1.28 MHz = 1/(780 ns). The first level decision must be made within 590 ns after a beam crossing to allow time for the detector electronics to be reset prior to the next crossing. Information from the main drift chamber cannot be used at this stage because of the long charge collection time.* The first level is satisfied if at least one TOF counter is struck. Cosmic ray rejection is improved by using the "Cruz Box." This device contains chronotron circuits[38] for identifying coincidences between the phototubes at the ends of each counter, using a narrower time window (40 ns) than could otherwise be used without loss of efficiency for annihilation events. The TOF requirement is effective for rejection of beam-gas interactions, which usually do not yield tracks of sufficient momentum to reach the TOF system. The Cruz Box coincidence rate was typically 5 to 15 kHz.

If the first level condition is met, the detector electronics are held through the next beam crossing. During the next 780 ns interval, a hardware logic system is used to search for tracks in the main drift chamber [Fig. 2.11]. Programmable logic array integrated circuits are used to identify coincidences between track segments in layer 2 and hit cells in layers 3 and 5, considering all possible patterns for tracks with momentum greater than 50 MeV/c. For high efficiency, only two of the three wires in each cell are required to be hit. If two or more tracks are found in the main drift chamber the second trigger level is satisfied, a computer interrupt is generated, and further triggers are inhibited while the event is logged to tape (typically 30 ms).

⋆ Layer 1 was formerly used to provide crude tracking information for the first trigger level.

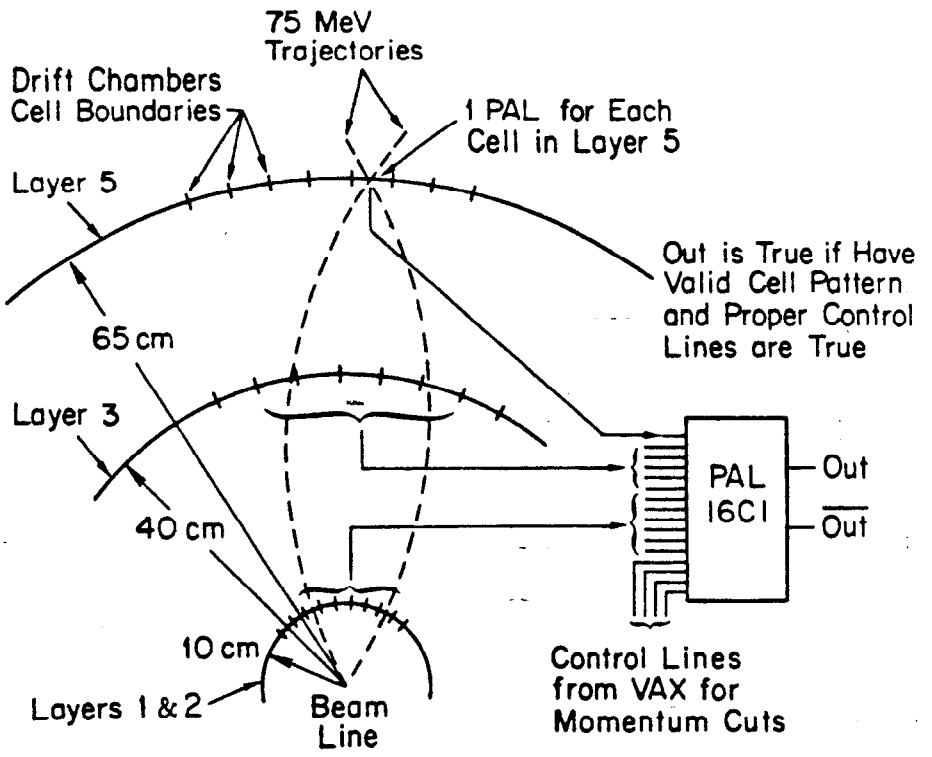

Figure 2.11 Schematic of trigger track finding logic. In 1985–86 the inner track segments were formed from layer 2 hits only.

The second level trigger rate was ~ 3 Hz, dominated by beam-gas interactions and cosmic rays. The hadronic event rate was < 0.05 Hz. The total dead time is around 10%, with the first level trigger contributing less than 1%.

For the last third of the 1985–86 data sample, an endcap Bhabha trigger was available. This provided a useful sample of events for calibration and checks of the endcap shower counters. The acceptance for Bhabha scattering events in the endcaps was otherwise very low, since the normal trigger requires the $e^{\pm}$ tracks to reach layer 5 of the drift chamber.

3
Data Sample, Event Reconstruction, and Event Simulation

3.1 Characteristics of e^+e^- Annihilation at 4.14 GeV

The e^+e^- annihilation cross section in the 4 GeV region is dominated by $c\bar{c}$ resonances and by $u\bar{u}$, $d\bar{d}$, and $s\bar{s}$ continuum production. The total hadronic cross section at $\sqrt{s} = 4.14\,\text{GeV}$ is ~ 20–$25\,\text{nb}$,[5] including 5 nb for $e^+e^- \to D\bar{D}$, $D^*\bar{D}$, and $D^*\bar{D}^*$.[44,45] Non-resonant D production (*e.g.*, $e^+e^- \to D\bar{D}\pi$) is not observed.[46] The cross section for D_s production is expected to be $\sim 1\,\text{nb}$.[47]

D_s Production Kinematics

At $\sqrt{s} = 4.14\,\text{GeV}$, D_s mesons are only produced in the final states $D_s^+D_s^-$ and $D_s^{*\pm}D_s^{\mp}$, or possibly in $D_s^+D_s^-\pi^0$. To study the relative cross sections for these production processes (and to reduce backgrounds), we use the recoil mass (or "missing mass") from a reconstructed D_s candidate:

$$M_{\text{rec}}^2 = [\sqrt{s} - E]^2 - \vec{p}^{\,2}, \tag{3.1}$$

where E and $\vec{p}$ are the energy and momentum of the D_s candidate. For a D_s from $e^+e^- \to D_s^+D_s^-$ the recoil mass would be equal to the D_s mass. For non-resonant $D_s^+D_s^-\pi^0$ production the recoil mass would have a smooth distribution between

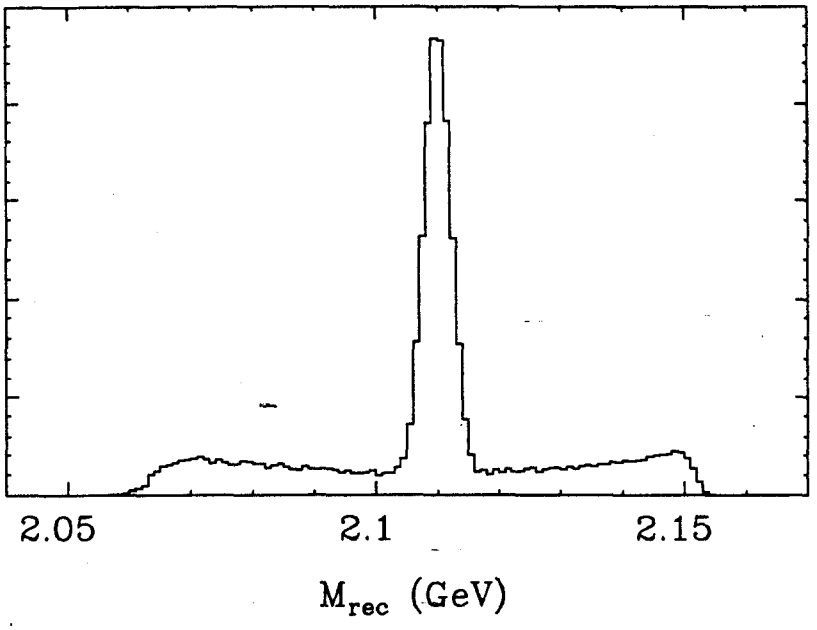

Figure 3.1 Distribution of $M_{\rm rec}$ from $e^+e^- \to D_s^{*\pm}D_s^{\mp}$. Detector acceptance and resolution are not included. The width of the primary peak reflects the SPEAR beam energy spread.

$M(D_s) + M(\pi^0) = 2.10\,\mathrm{GeV}/c^2$ and $\sqrt{s} - M(D_s) = 2.17\,\mathrm{GeV}/c^2$. The reactions

$$e^+e^- \to D_s^{*\pm}D_s^{\mp}, \tag{3.2}$$

$$D_s^{*\pm} \to \gamma D_s^{\pm}, \tag{3.3}$$

yield the D_s recoil mass spectrum shown in Fig. 3.1. The $D_s^{\mp}$ produced in (3.2) is referred to as *primary*, while the $D_s^{\pm}$ produced in (3.3) is referred to as *secondary*. The primary $D_s^{\mp}$ is produced with a fixed momentum of $0.35\,\mathrm{GeV}/c$, while the secondary $D_s^{\pm}$ is produced with momentum between 0.18 and $0.47\,\mathrm{GeV}/c$.

The recoil mass resolution for reconstructed D_s decays can be improved by replacing the measured E in equation (3.1) with $\sqrt{M^2 + \vec{p}^2}$, where M is the nominal D_s mass:

$$M_{\rm cr}^2 = \left[\sqrt{s} - \sqrt{M^2 + \vec{p}^2}\right]^2 - \vec{p}^2. \tag{3.4}$$

The quantity $M_{\rm cr}$ is referred to as the *constrained recoil mass.* This is different from the *beam constrained mass*, which is used for an even greater improvement in mass resolution in studies of $\psi(3770) \to D\bar{D}$ and $\Upsilon(4S) \to B\bar{B}$.

To estimate the resolution of $M_{\rm cr}$ relative to $M_{\rm rec}$, I make the approximation that the measurement errors on E and p are uncorrelated. This questionable hypothesis is confirmed by Monte Carlo simulation, with $\sigma(E) \cong \sigma(p)$. The fact that $\beta(D_s) \ll 1$ implies that the direction of $\vec{p}$ is not strongly correlated with the directions of the daughter kaon and pion momenta, so the correlation between E and p is also small.* Now

$$2M_{\rm rec}\, dM_{\rm rec} = -2E_{\rm rec}\, dE - 2p\, dp$$

so

$$\begin{aligned}\sigma(M_{\rm rec}) &\cong \left[\left(\frac{E_{\rm rec}}{M_{\rm rec}}\right)^2 + \left(\frac{p}{M_{\rm rec}}\right)^2\right]^{\frac{1}{2}} \sigma(p) \\ &\cong \sigma(p),\end{aligned}$$

where $E_{\rm rec}$, $M_{\rm rec}$, and p are evaluated for $D_s^* D_s$ events. For the constrained recoil mass we obtain

$$\begin{aligned}2M_{\rm cr}\, dM_{\rm cr} &= -2\left[\frac{E_{\rm rec}}{E} + 1\right] p\, dp \\ \sigma(M_{\rm cr}) &\cong \left[\frac{E_{\rm rec}}{E} + 1\right] \frac{p}{M_{\rm rec}} \sigma(p) \\ &\cong \frac{1}{3}\sigma(p),\end{aligned}$$

or

---

* Errors on E arise from errors on the magnitudes of the individual track momenta. The resulting errors on p can have the same or the opposite sign, since the individual momenta are added as vectors. After combining all tracks there is little correlation between E and p.

$$\sigma(M_{\rm cr}) \cong \frac{1}{3}\sigma(M_{\rm rec}).$$

This result agrees with the Monte Carlo simulation, which gives $\sigma(M_{\rm cr}) = 5\,{\rm MeV}/c^2$ and $\sigma(M_{\rm rec}) = 13\,{\rm MeV}/c^2$ for $D_s^+ \to \phi\pi^+$.

3.2 Mark III Data Sample at $\sqrt{s} = 4.14\,{\rm GeV}$

Between 1982 and 1985 the Mark III experiment collected data samples at various center-of-mass energies, corresponding to 5.8×10^6 produced J/ψ's, 1.5×10^5 $\psi(3685)$'s, and 48000 $\psi(3770) \to D\bar{D}$ events. Following an energy scan over the $\psi(3685)$ resonance, and several weeks of low luminosity and unstable detector operation, acquisition of data at $\sqrt{s} = 4.14\,{\rm GeV}$ was begun in earnest on 19 December 1985. The running period was terminated on 28 February 1986.

Offline studies revealed an intermittent tracking problem in the main drift chamber. For parts of certain runs the reconstructed $e^{\pm}$ momenta from Bhabha scattering events were shifted by $\pm 400\,{\rm MeV}/c$ from the nominal value, while the remainder of the run seemed normal. This phenomenon resulted from a zero-time shift in a portion of layer 2. Because each cell of layer 2 contains 12 sense wires on a radial line, a zero-time error can have a dramatic effect on measured track curvatures, with the direction of the momentum shift being opposite for + and − tracks and for tracks passing on the left and right sides of the layer 2 cell. Several such episodes were found offline, but it was not possible to isolate the cause of the problem in the hardware. Approximately 6% of the data sample was eliminated from consideration due to this and other minor misfortunes. The purified dataset corresponds to a total integrated luminosity of $6.30 \pm 0.46\,{\rm pb}^{-1}$. The luminosity determination is described below.

Determination of Total Integrated Luminosity

The luminosity determination was made using large-angle Bhabha scattering and dimuon events observed with the Mark III detector. The following selection criteria were used for both analyses. Events are required to contain two helix-fitted tracks of opposite charge. Each track must have momentum $> 0.8\,\mathrm{GeV}/c$, distance of closest approach to the z axis $< 6\,\mathrm{mm}$, and TOF information.* Further requirements are: time-of-flight difference $|t_+ - t_-| < 1.5\,\mathrm{ns}$; $|\cos\theta_0| < 0.5$, where θ_0 is the polar angle of the vector $\hat{p}_+ - \hat{p}_-$ (selection of large-angle events), and $\hat{p}_+ \cdot \hat{p}_- \leq -0.85$. The loose colinearity cut is used so that radiative events are readily accepted. No requirement against neutral showers is imposed. The detection efficiencies are determined by Monte Carlo simulation of $e^+e^- \rightarrow e^+e^-(\gamma)$ and $e^+e^- \rightarrow \mu^+\mu^-(\gamma)$.

To select Bhabha scattering events, one additional cut is imposed: each track must deposit at least 0.8 GeV in the shower counter. A total of 104470 candidate events were found in the purified data sample. A correction of 1030 ± 500 events is added to account for the rib in the barrel shower counter at $z = 0$. This number is estimated from the $\cos\theta_0$ distribution of the accepted events. Monte Carlo Bhabha events were generated with $|\cos\theta| < 0.6$ for both electrons. The cross section for scattering into this angular range is found (by the event generator) to be 36.0 nb. The efficiency of the detector and cuts for these events is 0.51 ± 0.04, where the systematic part of the error is estimated by varying the cuts. The trigger efficiency for two track events is taken to be 0.96 ± 0.03.[48] An additional factor of 0.99 is included in the efficiency because of a temporary trigger hardware problem which

* A TOF measurement is not accepted if the phototubes of the struck counter yield times which are inconsistent with the measured track z position.

caused two track events to be lost while not significantly affecting the detection of higher multiplicity events.[49] The total integrated luminosity is

$$\mathcal{L} = \frac{104470 + 1030}{0.51 \times 0.96 \times 0.99 \times 36.0\,\mathrm{nb}} = 6.03 \pm 0.58\,\mathrm{pb}^{-1} \qquad \text{(Bhabhas)}.$$

A systematic uncertainty of 5% is included for the cross section calculation in each channel. The statistical error is negligible.

Dimuon events are selected by requiring each track to deposit less than 0.8 GeV in the shower counter, and to be detected in both layers of the muon system. The data sample contains 10148 candidates. In this case the Monte Carlo simulation (with no restriction on the *generated* $\cos\theta$) gave a cross section of 6.62 nb and an efficiency of 0.248 ± 0.014. The total integrated luminosity is

$$\mathcal{L} = \frac{10148}{0.248 \times 0.96 \times 0.99 \times 6.62\,\mathrm{nb}} = 6.50 \pm 0.54\,\mathrm{pb}^{-1} \qquad \text{(dimuons)}.$$

The statistical error of 1% has been added in quadrature to the other errors.

The ratio of the Bhabha and dimuon luminosities thus determined is 0.93 ± 0.09, where common errors have been omitted. The errors which only affect the Bhabha analysis total $0.47\,\mathrm{pb}^{-1}$. The errors which only affect the dimuon analysis total $0.40\,\mathrm{pb}^{-1}$. The systematic errors which affect both analyses total 5.6%. The measurements were combined by weighting them according to the independent errors. The total error is the corresponding combination of the independent errors, with the common systematic error added in quadrature. The final result is

$$\mathcal{L} = 6.30 \pm 0.46\,\mathrm{pb}^{-1}.$$

This result is $\sim 30\%$ larger than that derived from the luminosity monitor in the east interaction region (a pleasant surprise). By considering small portions of the data sample, a slow decline of the efficiency of that device is seen.

3.3 Event Reconstruction

In this section I describe how the reconstructed sample of hadronic events is obtained from the data tapes written at SPEAR.

The raw data sample contains $\sim 10^7$ events and occupies approximately 350 tapes (6250 bpi, 2400 ft each; ~ 150 miles total). Before reconstruction the events are processed through a filter program which uses raw detector information to reject beam-gas scattering and cosmic ray events. This reduced the number of events to be reconstructed to $\sim 4 \times 10^6$.

The reconstruction package finds and measures charged tracks in the main drift chamber, and performs a fit to locate the event vertex position. Energy loss corrections and single-track fits to the beam axis are performed for various particle mass hypotheses. Energy loss measurements from layer 2 are processed for particle identification. Showers in the electromagnetic calorimeters are reconstructed, and an attempt is made to associate charged tracks with the showers they induced. Finally, TOF and muon system hits are analyzed and linked with reconstructed tracks. The resulting track measurements for each event are saved on tape along with the raw detector data. Reconstruction requires ~ 0.25 s of CPU time (IBM 3081) per hadronic event. Bhabha scattering and dimuon events are extracted from this data sample for luminosity determination and detector performance studies.

A post-filter program is used to examine the reconstructed event information and select hadronic events for D and D_s analyses. The purified hadron-filtered sample contains 296000 events. A compressed version of this set occupies eight standard (38K bpi) tape cartridges.

Further details on the filter, reconstruction, and hadron filter are given in the following sections.

3.4 Filter

The event filter program[50] uses information from various detector systems to remove uninteresting events from the data sample prior to reconstruction. TOF and muon system information is used to reject obvious cosmic rays and identify dimuon events. The total energy deposited in the calorimeters, the number of showers, and the asymmetry in the energy flow* allow classification of hadronic events, Bhabhas, cosmic rays, and "junk." A fast track finding algorithm for the main drift chamber (see Section 3.5) is also used to ensure that high multiplicity events are not discarded.

3.5 Reconstruction Algorithm

Main Drift Chamber Reconstruction

The first stage of track finding uses a fast and efficient algorithm[51] which emulates the track finding hardware of the trigger. The pattern of hit drift chamber cells in the axial layers (2, 3, 5, 7, and 8) is compared digitally to a "dictionary" which contains all possible hit patterns produced by real tracks with $p_{xy} > 50\,\mathrm{MeV}/c$. Left-right ambiguities are resolved using timing information from triplets of sense wires (see Chapter 2). Tracks in the $r\phi$-plane are identified from the local direction and curvature of track segments within individual cells. A fast circle fitter is used to provide accurate starting parameters for the full helix fit, and if necessary to

* Asymmetry $\equiv |(\Sigma E_i \hat{r}_i)/\Sigma E_i|$, where E_i and $\hat{r}_i$ are the energy and direction unit vector of the ith shower.

remove confusion caused by possibly erroneous information or overlapping tracks. When possible, z information from the stereo drift chamber layers (4 and 6) is then associated with the $r\phi$ tracks; both layers were used for 81% of the reconstructed $r\phi$ tracks in the 4.14 GeV data sample. A preliminary determination of the event vertex position is made using these tracks. When one of the stereo layer hits is not present on a track because of inefficiency or because the track exits through one end of the chamber, the event vertex position is used for a z measurement on the track (16% of the $r\phi$ tracks). If no stereo hit is available, the event vertex is used in conjunction with endcap shower counter hits (2%) or with drift chamber charge division ($< 1\%$) to provide z information. Approximately 1% of the $r\phi$ tracks could not be reconstructed in three dimensions.

Finally the track momentum is determined from the measured drift times and the positions of the hit sense wires. The momentum measurement is accomplished by means of an iterative fit to a series of linked helices. Residuals are computed by propagating tracks from layer to layer through the magnetic field, which is assumed to be homogeneous over the length of each step. The five track parameters determined by the helix fit are ϕ = azimuthal direction of $\vec{p}$ at point of closest approach to the z-axis, $\kappa \equiv 1/p_{xy}$, $s \equiv \tan\lambda$, $\xi = x\sin\phi - y\cos\phi$ = signed distance of closest approach to z-axis, and $\eta = z$ position at closest approach point.

The momentum resolution of the drift chamber is expected to be $\Delta p/p \sim 0.015\sqrt{1+p^2}$, where p is in GeV/c. The resolution for muons from $e^+e^- \to \mu^+\mu^-$ is predicted in a Monte Carlo simulation to be 65 MeV/c, while the observed resolution is 91 MeV/c [Fig. 3.2].† Figures 3.3 and 3.4 show comparisons of data and

† The distributions shown in this chapter are not exactly Gaussian; the quoted resolutions

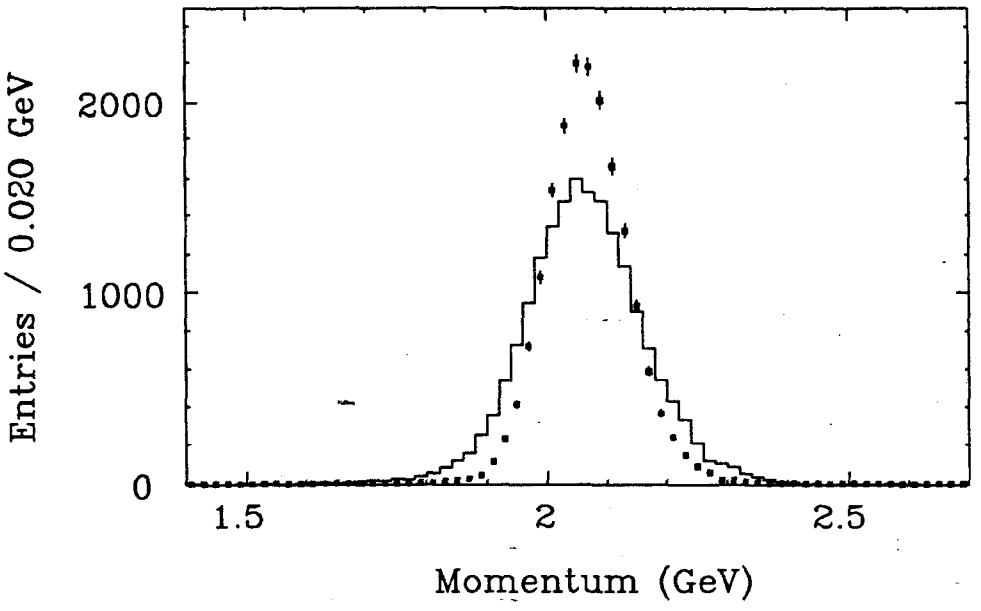

Figure 3.2 Measured momentum for dimuon events, data (histogram) and Monte Carlo (points). Back-to-back dimuons are chosen to reject radiative events.

Monte Carlo distributions of track direction measurements. In Fig. 3.3 is plotted $\tan\lambda_+ + \tan\lambda_-$. The observed distributions correspond to single-track $\tan\lambda$ resolutions of 0.011 for data and 0.008 for Monte Carlo. The quantity $\phi_+ - \phi_- - \pi$ [Fig. 3.4] measures the acollinearity of the muon tracks in the xy-plane. The corresponding ϕ resolutions are 1.9 mrad for data and 1.6 mrad for Monte Carlo. One concludes that the zero-times, time-to-distance relationships, and/or chamber survey are not accurately determined; these parameters are assumed to be precisely known in the Monte Carlo. However, the high momentum tracks in dimuon events are more sensitive to errors of this type than are the hadrons in charm events. Figure 3.5 shows

are FWHM/2.35. Dimuon events for the checks in this section are taken from the 1985–86 data set. Events are required to have two oppositely charged tracks identified as muons by the muon detection system and each depositing less than 350 MeV in the calorimeters. No neutral showers are allowed. To reject cosmic ray muons, the TOF difference $|t_+ - t_-|$ is required to be less than 4 ns.

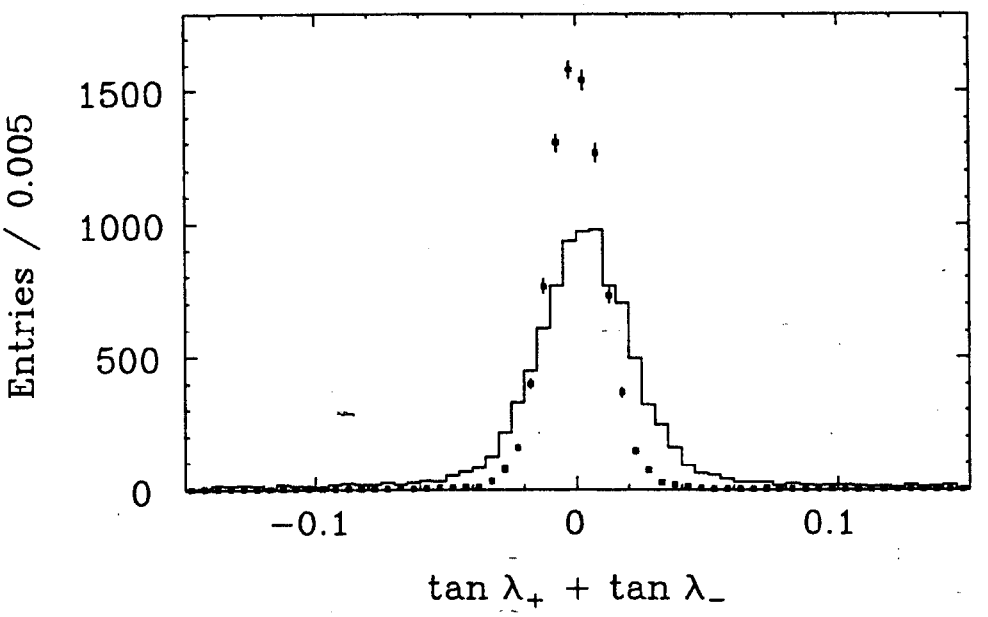

Figure 3.3 $\tan\lambda_+ + \tan\lambda_-$ for dimuon events, data (histogram) and Monte Carlo (points).

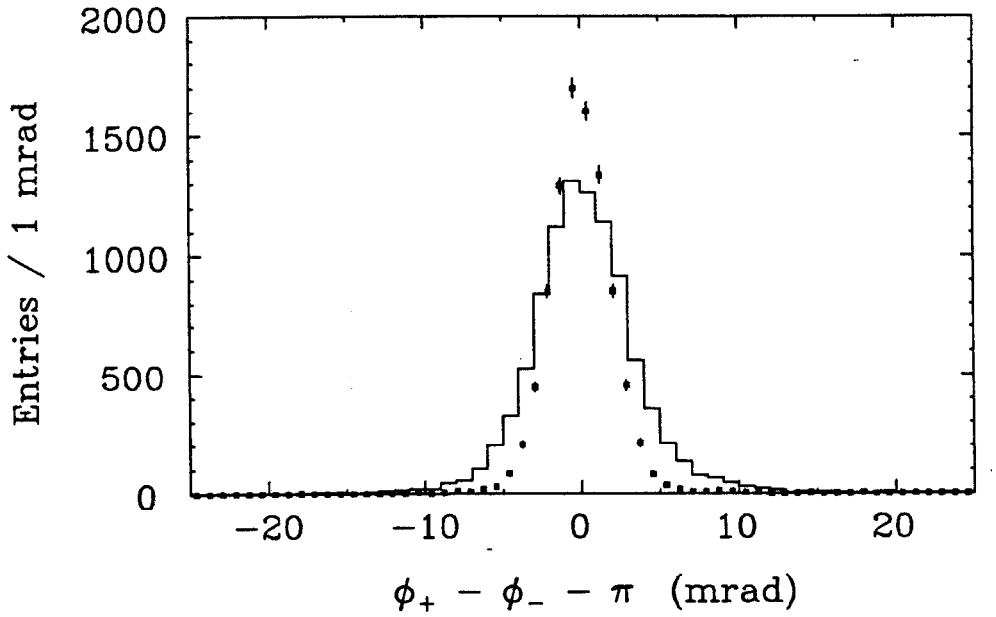

Figure 3.4 $\phi_+ - \phi_- - \pi$ for dimuon events, data (histogram) and Monte Carlo (points).

that there is no significant discrepancy between data and Monte Carlo drift chamber resolutions for D decays. The mass resolutions for $D^0 \to K^-\pi^+$, $D^+ \to K^-\pi^+\pi^+$, and $D^0 \to K^-\pi^+\pi^+\pi^-$, are respectively $\sigma = 28 \pm 2$, 22 ± 2, and $14 \pm 2\,\mathrm{MeV}/c^2$ in the data, and 25, 19, and $17\,\mathrm{MeV}/c^2$ in the Monte Carlo.

The momentum resolution for charged tracks can be improved by using the location of the interaction point as a track position measurement. This is accomplished by two fitting procedures which are used in this thesis, the *vertex constraint fit* and the *beam fit.*

In each event a vertex constraint fit is performed simultaneously on all tracks which pass within a fiducial volume around the origin ($|\xi| < 15\,\mathrm{mm}$ and $|\eta| < 15\,\mathrm{cm}$). The tracks are constrained to pass through a common point; the position and size of the beam crossing spot are used to constrain the location of this point. The vertex-constrained momenta are used in this thesis for the analysis of Section 4.2 only.

Use of the vertex constraint fit has several disadvantages:

1. The covariance matrices for the parameters of each track must include contributions from multiple Coulomb scattering and energy loss in the material of the detector which depend on the particle mass. However, in practice each particle in the fit is assumed to be a pion in the calculation of these contributions.

2. The vertex constraint fit introduces correlations between the parameters of different tracks, which are not considered in the Mark III kinematic fitting programs.

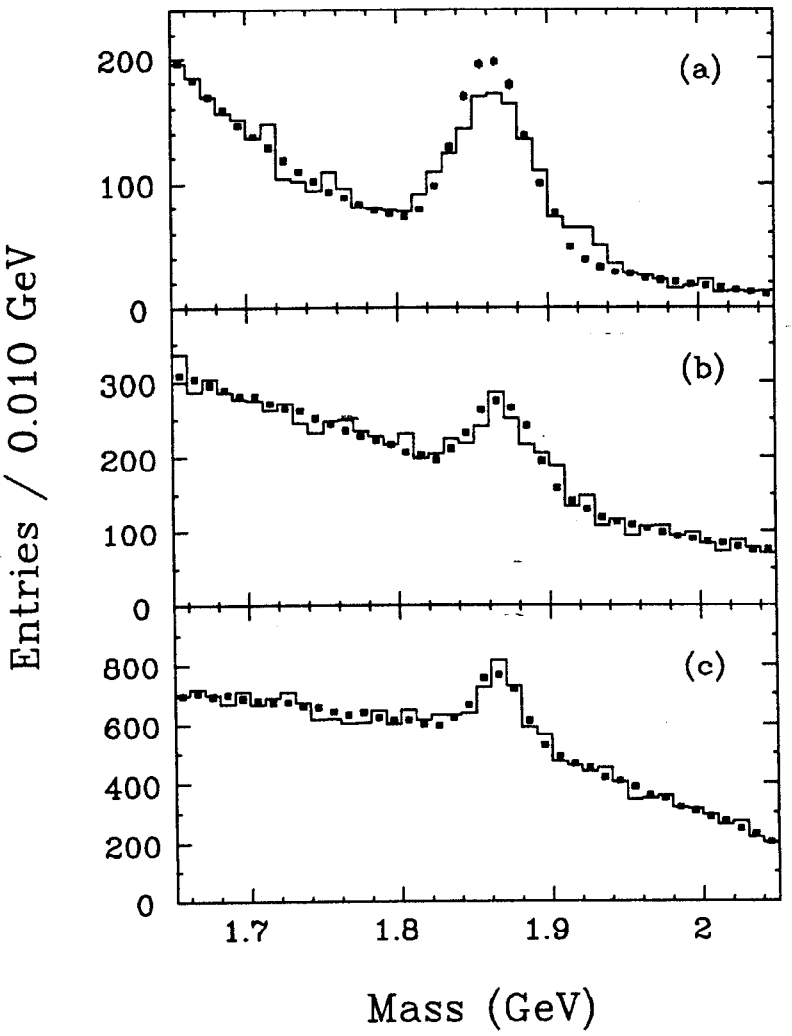

Figure 3.5 $D^0 \to K^-\pi^+$, $D^+ \to K^-\pi^+\pi^+$, and $D^0 \to K^-\pi^+\pi^+\pi^-$ mass spectra, data (histogram) and Monte Carlo (points). For the Monte Carlo plots, the form of the background and the number of signal events are taken from a fit to the data. In each mode the requirement $M_{\rm rec} > 1.95\,{\rm GeV}/c^2$ is imposed. The TOF criteria of the $D_s^+ \to \bar{K}^{*0}K^+$ analysis (Chapter 5) are used for particle identification.

3. The presence of a K_S^0 in an event can negate the benefits of vertex fitting for *all* of the tracks.

The beam fit[52] was developed to avoid these problems. Multiple Coulomb scattering and energy loss corrections (described in the Appendix) are applied to the measured parameters and covariance matrix of each track for each of the identification hypotheses e, μ, π, K, p. Then the single tracks are constrained to emanate (in the xy projection) from the beam crossing spot to obtain the beam fit momentum for each hypothesis. Although the tracks of an event are no longer constrained to pass through a common point, a significant resolution improvement is achieved [Fig. 3.6]. In addition, the beam fit χ^2 is a useful variable for rejecting tracks which do not originate in the primary event vertex, such as kaon decay products.

Shower Counter Reconstruction

Clusters of hits in the shower counters are identified. Charge division is used to determine the shower position along the proportional tubes (the z position in the barrel or y in the endcaps). The total energy deposited in each shower is calculated from the charge integrals.

The energy resolution of the shower counters is $\Delta E/E \sim 18\%/\sqrt{E}$ (E in GeV). Figure 3.7 shows the reconstructed barrel and endcap energy distributions for Bhabha events. Shower positions in the barrel are measured with a resolution of 3 cm (corresponding to $\sim$ 25 mrad) in z and 1.2 cm ($\sim$ 10 mrad) azimuthally. The shower position resolution of the endcaps is approximately 1 cm ($\sim$ 6 mrad) in each direction.

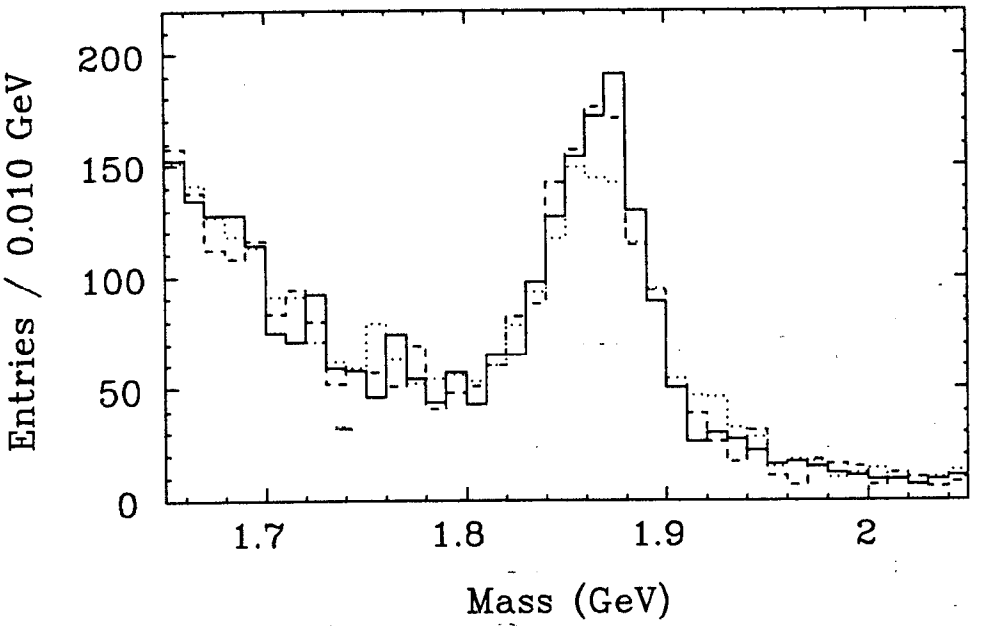

Figure 3.6 Comparison of mass resolution using track parameters from helix fit (dotted histogram), vertex constrained fit (dashed), and beam fit (solid) for $D^0 \to K^-\pi^+$. The same $K\pi$ combinations are selected in each case. Tracks are required to have beam fit χ^2 confidence level CL $> 10^{-4}$ *and* vertex constrained fits, and $M_{\rm rec}$ from the helix fits $> 1.95\,{\rm GeV}/c^2$.

Time of Flight Reconstruction

Struck TOF counters are associated, if possible, with reconstructed drift chamber or shower counter tracks. For each track the time of flight is determined from the phototube times, accounting for the propagation time of light in the counter, and for discriminator "time-walk" caused by variations in pulse height. Since there are two phototubes on each scintillator, it is normally possible to determine the z position of a TOF hit from the phototube times. For charged tracks this value is compared with the projected z position from drift chamber information, providing a check against errors in the drift chamber and TOF reconstruction. If two tracks hit the same TOF counter, the time measurement from the nearer phototube is

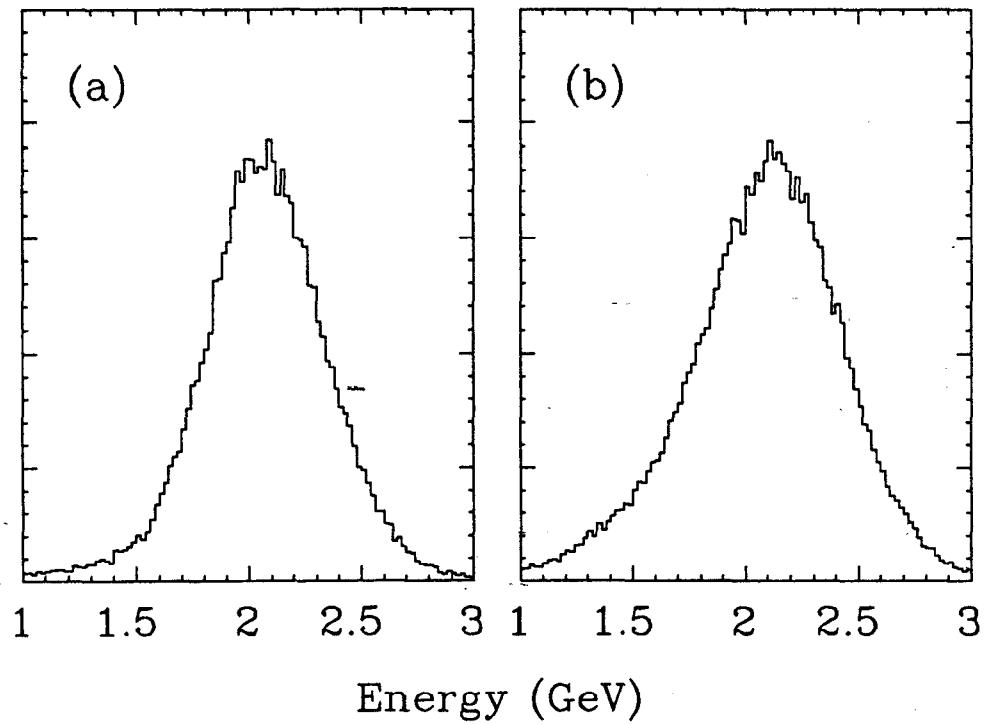

Figure 3.7 Reconstructed energy E for Bhabha scattering events (a) in the barrel and (b) in the endcaps.

used for each track, and the phototube pulse amplitudes are shared according to the projected z positions and the measured light attenuation properties of the counter. A quality flag is returned which identifies TOF measurements which may be unreliable, *e.g.* because of ambiguities caused by multiple tracks in a counter. After the analysis of Section 4.2 was completed, the reconstruction algorithm was revised to improve the handling of situations such as these.

To identify charged tracks the measured time of flight $t_{\rm meas}$ is compared to the predicted times t_i for the hypotheses $i = e, \mu, \pi, K, p$, where

$$t_i = \frac{a\sqrt{M_i^2 + p^2}}{pc},$$

M_i is the hypothesized mass, and a, p are the path length and momentum determined from the drift chamber reconstruction. In this thesis the normalized time residual $(t_{\rm meas} - t_i)/\sigma_i$ is used to select π and K candidates. The time difference uncertainty σ_i includes the time resolution of the individual TOF counter and the uncertainty on the predicted time resulting from the drift chamber resolution.

The capabilities of the TOF system are illustrated in Fig. 3.8. The π-K separation is at least 3σ for momenta up to 0.8 GeV/c. Figure 3.9 shows the time residuals for dimuon events from the 1985–86 data sample. A Gaussian fit to the distribution between -0.4 and $+0.4$ ns yields $\sigma = 207 \pm 2$ ps, whereas the same measurement from 1983 J/ψ data gave $\sigma = 175$ ps.[41] The resolution is over 300 ps for a few of the counters. The reasons for the change are radiation damage to the counters and lengthening of the SPEAR bunches at higher energies and beam currents. The beam crossing time spread is ~ 75 ps.

Muon Detector Reconstruction

Charged tracks from the drift chamber reconstruction are projected through the shower counter, magnet coil, steel detector shell, and into the muon system. The amount of material traversed by the track is computed in order to account for multiple scattering; a search is made for struck muon tubes within 6σ of the projected track. A high-momentum track is identified as a muon if it is detected in both layers of the muon system. The efficiency of the detector is studied by selecting dimuon events using drift chamber and TOF information, and requiring an identified μ^+. When the negatively charged track lies within the acceptance of the muon system, the efficiency for identification is found to be $97.5 \pm 0.2\%$, in agreement with the Monte Carlo prediction of $97.6 \pm 0.1\%$.

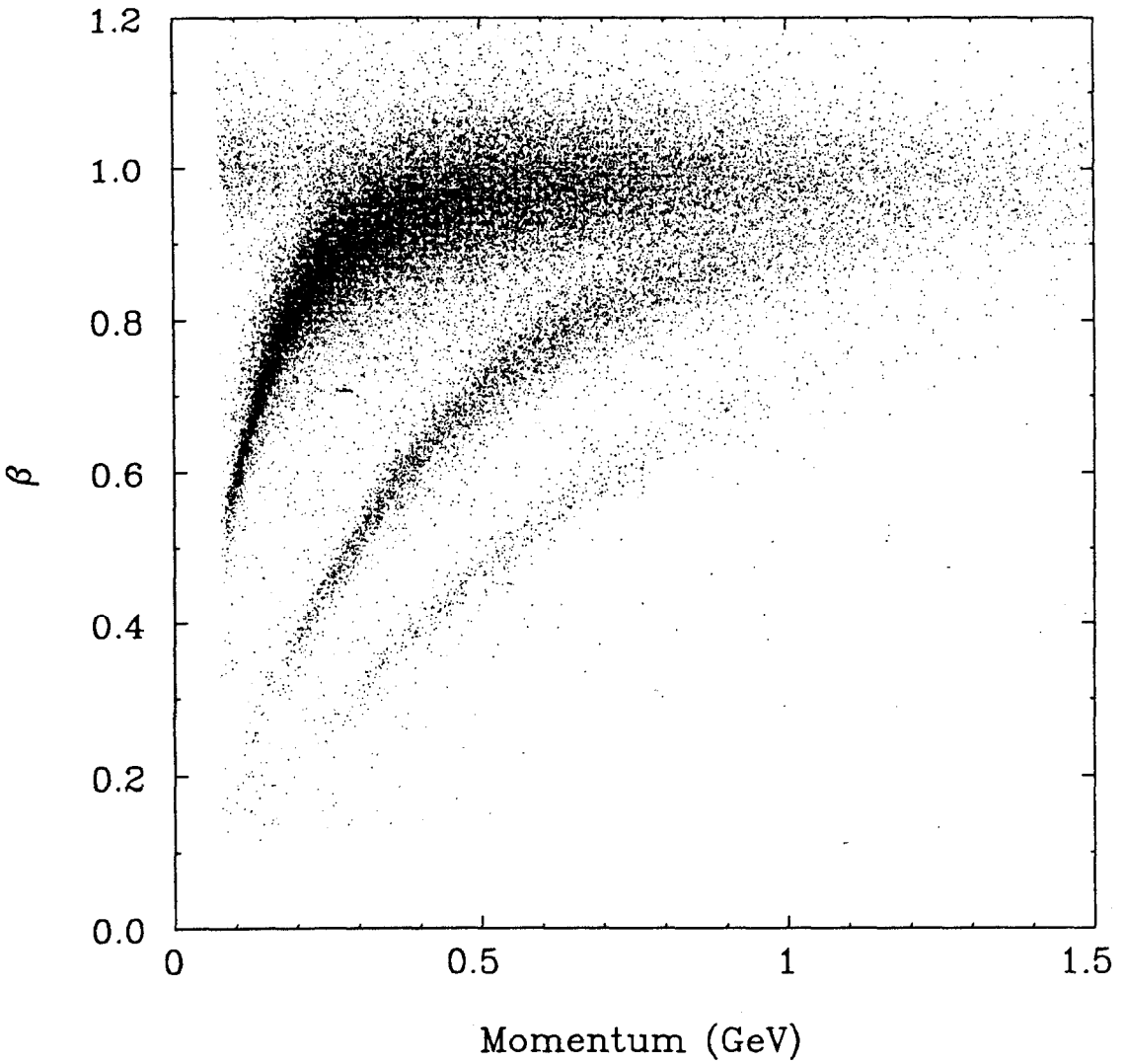

Figure 3.8 Momentum *vs.* TOF $\beta = a/ct_{\text{meas}}$ for tracks from the hadronic event sample. The pion (and muon) band is most prominent, with kaon and proton bands below it. The electron band ($\beta = 1$) can be seen at low momenta. Tracks with $p < 0.070\,\text{GeV}/c$ are curled up before reaching the TOF system.

3.6 Hadronic Event Filter

The post-filter program is used to reduce the size of the event sample by more than a factor of 10 without loss of efficiency for charm decays. QED events which

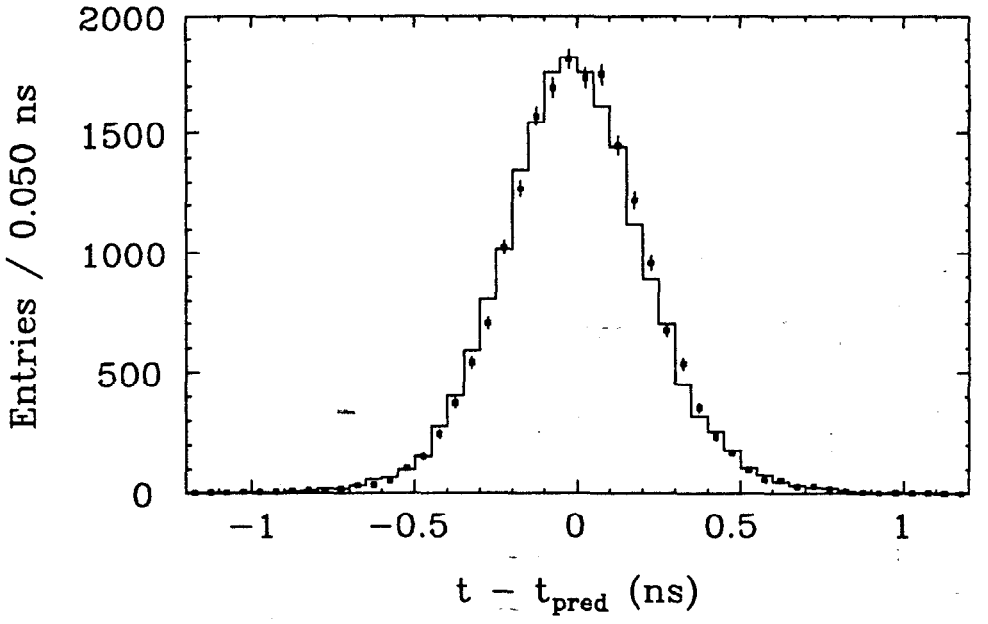

Figure 3.9 Measured minus predicted time of flight from dimuon events, data (histogram) and Monte Carlo (points). The Monte Carlo TOF simulation used in this thesis is based on the dimuon time residuals observed in the 1985–86 data.

were already flagged by the pre-filter are discarded. The refined track information obtained in the full reconstruction allows more effective cuts to be made for eliminating uninteresting events. Loose requirements are imposed on the event vertex z position to reject cosmic rays and beam-gas events. Events containing two charged tracks must pass cuts on p_{xy}, acolinearity, TOF, and shower energy.

3.7 Event Simulation

Monte Carlo events for efficiency and background studies are created using a detailed detector simulation program. Event generators (described below) are available to create events of various types. The generated track four-momenta are used to calculate particle trajectories and the simulated detector response. Energy loss,

multiple Coulomb scattering, and hadronic interactions in the detector material are included. Detector efficiencies and resolutions, dead drift chamber wires, and the inoperative layer 1 are also taken into account. The time residual distributions of the individual TOF counters are taken from real dimuon events. The barrel shower counter simulation uses a library of real showers extracted from real $J/\psi \to \rho\pi$ decays. Raw event data is generated in the same format as in real events, and the same reconstruction algorithm is used.

Event Generators

Generators for the following processes were used in this thesis:

- $e^+e^- \to D_s^{*\pm} D_s^{\mp}$,
- $e^+e^- \to D_s^+ D_s^-$,
- $e^+e^- \to D^* \bar{D}^*$,
- $e^+e^- \to D^* \bar{D}$,
- $e^+e^- \to D\bar{D}$,
- $e^+e^- \to u\bar{u}(g)$, $d\bar{d}(g)$, $s\bar{s}(g)$ (Jetset 6.2),
- $e^+e^- \to \mu^+\mu^-(\gamma)$;[53]
- $e^+e^- \to e^+e^-(\gamma)$.[54]

The charm event generators allow the user to select specific decay modes for one or more of the charmed mesons, or to allow those particles to be "autodecayed" according to a list of final states and branching fractions. In the D_s generators the decay channels of η, η', K^*, and ϕ mesons can also be selected. When D or D_s decays to vector-pseudoscalar final states are selected, the vector particle two-body decay angles are generated with a $\cos^2\theta$ distribution. The correct matrix elements for $\eta \to \pi^+\pi^-\pi^0$ and $\eta' \to \gamma\rho^0$ decays are also used. A uniform matrix element is used otherwise.

The Jetset 6.2 generator,[55] based on the Lund string fragmentation model, is used to estimate backgrounds from non-charm continuum events. A cross section of 12.49 nb for these final states at $\sqrt{s} = 4.14$ GeV is calculated by Jetset. This value is used to normalize the background predictions. No attempt is made to adjust the parameters of the model, or to defend its accuracy at these low center-of-mass energies.

Decays are processed in all of the generators until the four-momenta of the "stable" daughters (γ, e, μ, $\pi^{\pm}$, $K^{\pm}$, K^0_L, p, $\bar{p}$, n, $\bar{n}$) are obtained. The detector simulation adds $\pi^{\pm}$, $K^{\pm}$ decays, γ conversions, and e bremsstrahlung.

3.8 Kinematic Fitting

Constraints of several types may be imposed on the measured track momenta in order to improve resolutions and reject background. In such a procedure one computes the vector of track parameters $\mathbf{x} = (\phi, \kappa, s)$ which minimizes the quantity

$$\chi^2 = (\mathbf{x} - \mathbf{x}_{\mathrm{meas}})^t \, \mathbf{S}^{-1} (\mathbf{x} - \mathbf{x}_{\mathrm{meas}}),$$

and satisfies the constraint conditions $f(\mathbf{x}) = 0$. Here $\mathbf{x}_{\mathrm{meas}}$ is the vector of measured track parameters and $\mathbf{S}$ is the block-diagonal matrix containing the 3×3 covariance matrices associated with the individual track measurements. (The charged track parameters ξ and η are not considered in the fit.) The constraint conditions represent a particular hypothesis for the particle identities and event topology. The number of degrees of freedom of the χ^2 distribution is equal to the number of constraints.

The following types of constraints are used in various combinations in this analysis:

1. The total four-momentum of a set of reconstructed tracks is equal to the four-momentum of the colliding e^+e^-: $(\vec{0}, \sqrt{s})$.

2. The invariant mass of a subset of tracks is fixed to a constant.

3. The recoil mass of a subset of tracks is fixed to a constant; the recoiling object is not reconstructed.

4. Two disjoint subsets of tracks have equal but unspecified invariant masses.

Backgrounds are reduced by rejecting track combinations which yield large χ^2. Since the observed track measurement resolutions are worse than expected (Section 3.5) the computed χ^2 values will be too large, and the detection efficiencies will be smaller than predicted by the Monte Carlo. For the one-constraint fits of Chapters 4 and 5 this effect is taken into accounted in the systematic errors on the efficiency. The four- and six-constraint fits of Chapter 6 require more delicate treatment: the observed track measurement resolutions are used to correct the covariance matrices for the systematic errors which appear to be present. For each track, the covariance of the parameters x_i and x_j is multiplied by $s_i s_j$ [Table 3.1]; these scaling factors are determined from studies of the residual distributions from kinematic fits on the data. Dimuon events from the 1985–86 data sample are used to obtain the drift chamber factors, and $J/\psi \to \rho\pi$ events are used for the shower counter factors. The covariance matrices in the Monte Carlo need no adjustments.

Table 3.1 Correction factors for track parameter covariance matrices.

x_i	s_i
Drift Chamber	
ϕ	1.14
$1/p_{xy}$	1.16
$\tan\lambda$	1.22
Barrel Shower Counter	
ϕ	1.21
$\tan\lambda$	1.14
$\sqrt{E}$	0.92
Endcap Shower Counters	
x/z	1.29
y/z	1.10
$\sqrt{E}$	1.16

4
Analysis of $D_s^+ \to \phi\pi^+$

4.1 Introduction

The D_s^+ has been observed in many experiments in the decay mode $D_s^+ \to \phi\pi^+$, $\phi \to K^+K^-$.[17,28–30,56–58] Since the ϕ lies just above K^+K^- threshold and is quite narrow, combinatoric background is relatively easy to suppress. This has been especially helpful in e^+e^- experiments. Because of its prominence, the $\phi\pi^+$ mode is customarily used for normalization in measuring the relative branching fractions of other D_s^+ decay modes.

In Section 4.2 I describe the Mark III observation of $e^+e^- \to D_s^* D_s$, with $D_s^+ \to \phi\pi^+$.[59] An excess of $\phi\pi^+$ combinations is found at $M(\phi\pi^+) \sim 1.97\,\mathrm{GeV}/c^2$ and $M_{\mathrm{rec}} \sim 2.1\,\mathrm{GeV}/c^2$. The calorimeter energy resolution is inadequate to observe the D_s^* directly in its decay to γD_s. The D_s^+ and D_s^{*+} masses and $\sigma(D_s^* D_s) \times B(D_s^+ \to \phi\pi^+)$ are extracted from the $M(\phi\pi^+)$ and M_{cr} distributions.

In Section 4.3 I report another measurement of σB from the same data set. A smaller systematic uncertainty is achieved from further studies of the track selection and identification efficiencies. The procedure includes kinematic fitting of each $K^+K^-\pi^+$ combination to the hypothesis $e^+e^- \to K^+K^-\pi^+ D_s^{*-}$, where the D_s^{*-}

is not reconstructed, but is used as a recoil mass constraint. This technique leads to improved mass resolution for primary D_s's, and to reduced backgrounds. The analysis also benefits from improvements in the TOF reconstruction algorithm. This measurement is used in the determination of $B(D_s^+ \to \bar{K}^{*0}K^+)/B(D_s^+ \to \phi\pi^+)$, and in the double tag analysis of Chapter 6.

4.2 Details of the Original Analysis

Analysis of the decay mode $D_s^+ \to \phi\pi^+$, $\phi \to K^+K^-$, begins with the selection of events from the hadron-filtered sample which contain ≥ 3 charged tracks. A vertex-constraint fit is performed for each event to improve the charged-track momentum resolution (See Chapter 3.) If the contribution of a track to the fit χ^2 is more than 12.5 (for two degrees of freedom), the original helix fit momentum is used. Tracks which do not satisfy the fitter pre-selection criteria are rejected altogether.

Kaon candidates are identified using the TOF system. We require

$$\frac{|t - t_K|}{\sigma_K} < \frac{|t - t_\pi|}{\sigma_\pi},$$

where t is the measured time of flight, t_π, t_K are the predicted π and K times, and σ_π, σ_K are the uncertainties on the time differences. All tracks which survive the vertex-constraint fit are accepted as pion candidates.

The invariant mass distribution of K^+K^- combinations in the ϕ region is shown in Fig. 4.1. A ϕ signal is seen which contains 236 ± 34 entries. Combinations with mass within $10\,\mathrm{MeV}/c^2$ of the nominal ϕ mass are chosen as ϕ candidates, and all $\phi\pi^+$ combinations are formed. A scatter plot of the $\phi\pi^+$ mass *vs.* $M_{\rm rec}$ is shown in Fig. 4.2. An enhancement is observed at $M(\phi\pi^+) \sim 1.97\,\mathrm{GeV}/c^2$ and

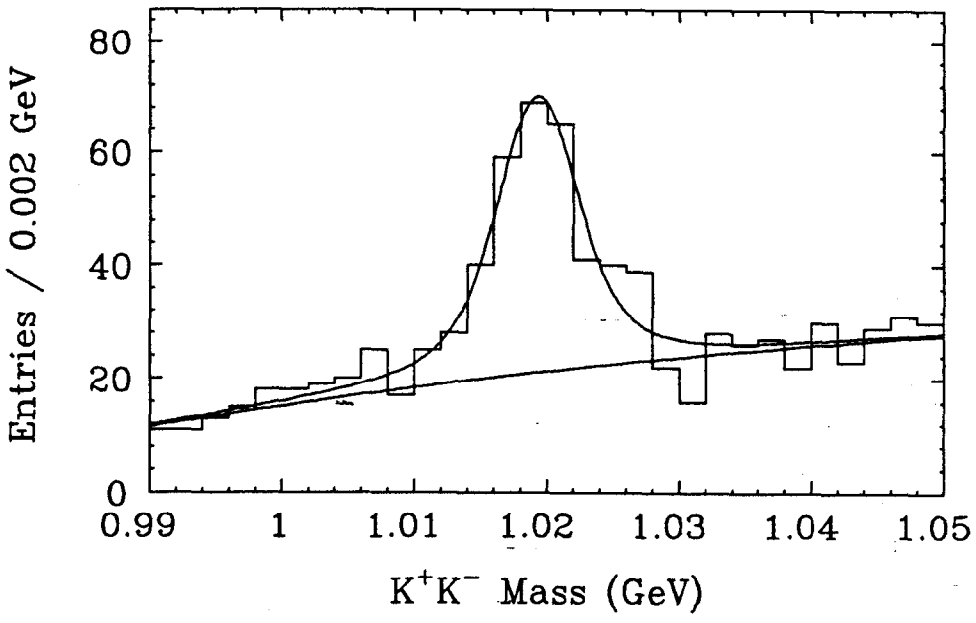

Figure 4.1 Inclusive K^+K^- mass distribution for events containing ≥ 3 charged tracks.

$M_{\rm rec} \sim 2.1\,{\rm GeV}/c^2$, which is the expected signal for $e^+e^- \to D_s^{*\pm}D_s^{\mp}$. A hint of $D^+ \to \phi\pi^+$ appears at $M_{\rm rec} \sim M(D^*)$. There is no evidence for $e^+e^- \to D_s^+D_s^-$.

The $M_{\rm rec}$ distribution for $\phi\pi^+$ combinations near the D_s mass [$M(\phi\pi^+)$ between 1.92 and $2.02\,{\rm GeV}/c^2$] is shown in Fig. 4.3. Entries from primary and secondary D_s's from $e^+e^- \to D_s^{*\pm}D_s^{\mp}$ are present in this distribution, near the D_s^* mass.

The D_s mass and $\sigma(e^+e^- \to D_s^{*\pm}D_s^{\mp}) \times B(D_s^+ \to \phi\pi^+)$ are measured from the distribution obtained by selecting $M_{\rm rec}$ in the D_s^* region, 2.04 to $2.18\,{\rm GeV}/c^2$ [Fig. 4.4]. The number of signal entries is determined by the fit to be 26.7 ± 5.2. The background shape is obtained by combining ϕ candidates with pions from different events. The Monte Carlo mass resolution of $15.1\,{\rm MeV}/c^2$ was assumed in the fit. The fitted D_s mass is $1972.4 \pm 3.7 \pm 3.7\,{\rm MeV}/c^2$. The systematic error accounts for uncertainties in the background shape ($2.5\,{\rm MeV}/c^2$), the effects of the

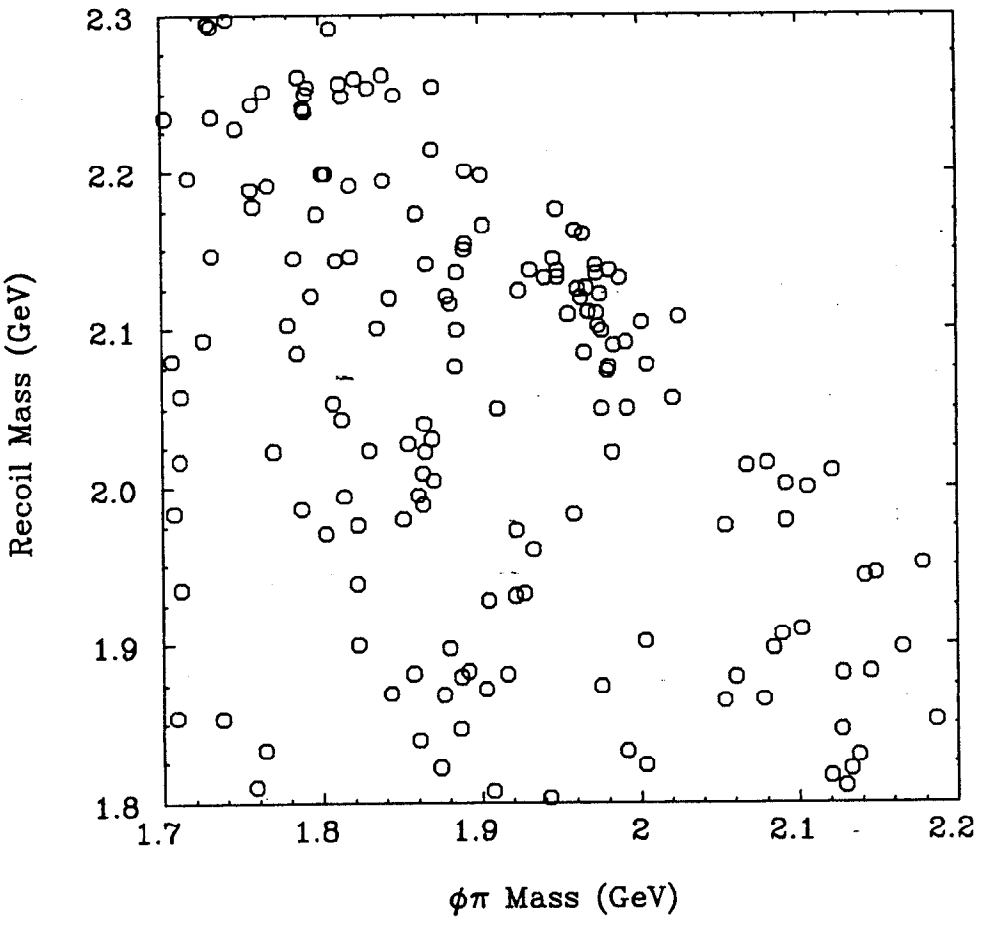

Figure 4.2 Scatter plot of $M(\phi\pi^+)$ *vs.* $M_{\rm rec}$.

selection criteria ($2.4\,{\rm MeV}/c^2$), and the momentum scale ($1.1\,{\rm MeV}/c^2$). A variety of background shapes and cuts are used in order to estimate the systematic error. The relationship between $M(D_s^+)$ and the momentum scale is determined by Monte Carlo simulation.

The angular distributions of the D_s^+ and ϕ decays are shown in Fig. 4.5 for combinations with $1.92 < M(\phi\pi^+) < 2.02\,{\rm GeV}/c^2$ and $2.04 < M_{\rm rec} < 2.18\,{\rm GeV}/c^2$. Here, θ_ϕ is the polar angle of the ϕ in the D_s^+ helicity frame; θ_{K^+} is the polar angle of the K^+ in the ϕ helicity frame. Since the D_s^* is not reconstructed, the helicity

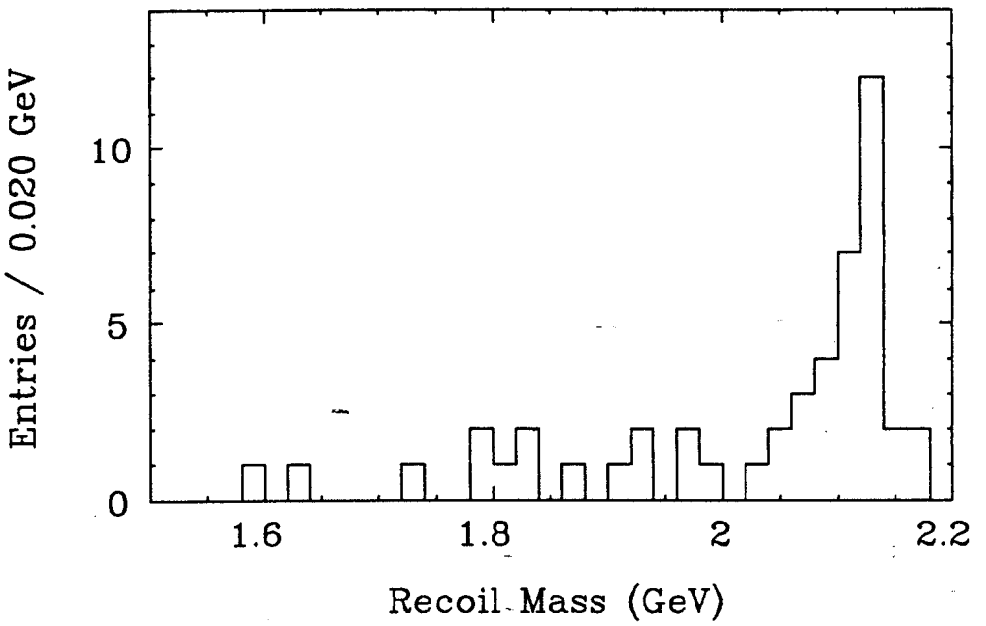

Figure 4.3 $M_{\rm rec}$ distribution for $1.92 < M(\phi\pi^+) < 2.02\,{\rm GeV}/c^2$.

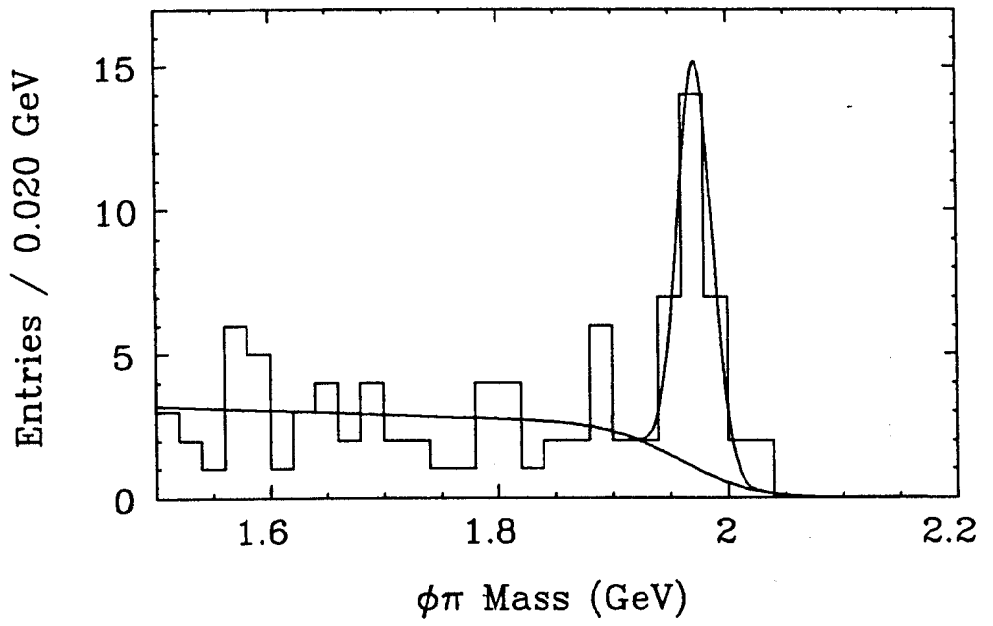

Figure 4.4 $M(\phi\pi^+)$ distribution for $2.04 < M_{\rm rec} < 2.18\,{\rm GeV}/c^2$.

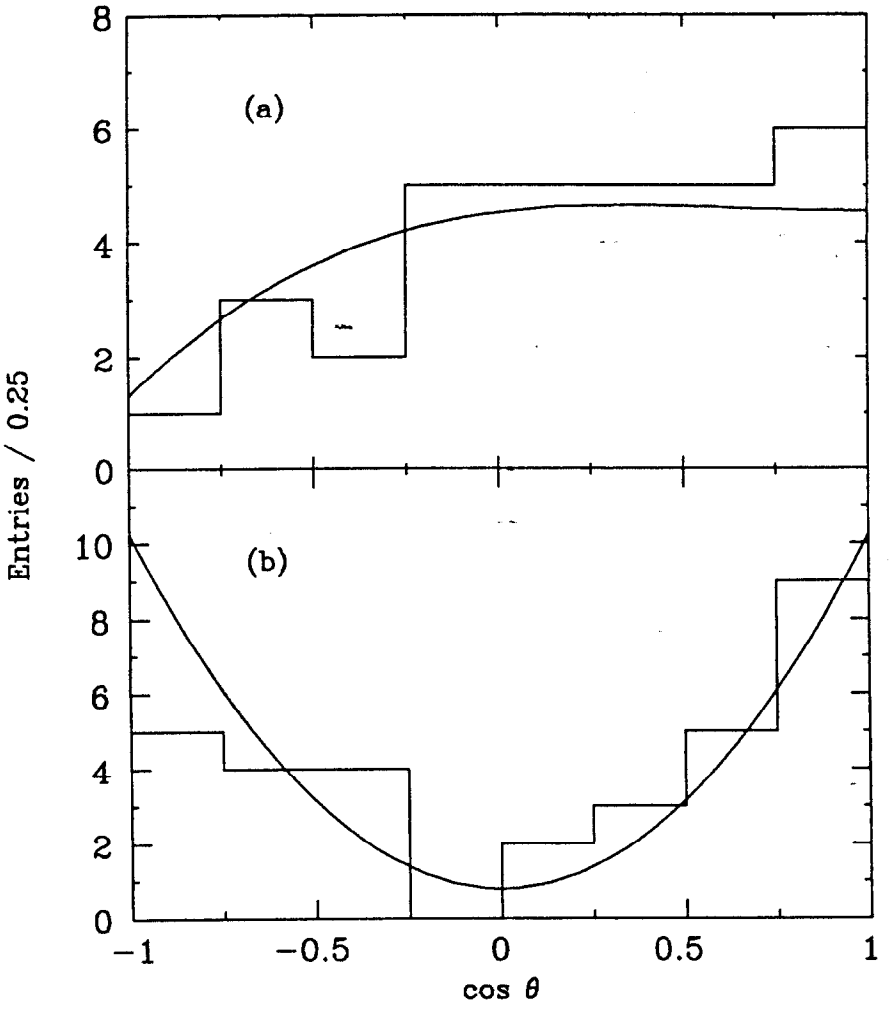

Figure 4.5 (a) $\cos\theta_\phi$ and (b) $\cos\theta_{K^+}$ distributions for combinations in the $D_s^* D_s$ signal region, not corrected for acceptance. The curves show the Monte Carlo predictions for $J^P(D_s) = 0^-$ and $J^P(D_s^*) = 1^-$.

frame of secondary D_s's is not determined; all $\phi\pi^+$ combinations are assumed to arise from primary D_s's in computing θ_ϕ. The curves were obtained from a Monte Carlo simulation which assumes $J^P(D_s) = 0^-$ and $J^P(D_s^*) = 1^-$ (Chapter 3). The ϕ is produced with helicity zero in the $D_s^+ \to \phi\pi^+$ decay, resulting in an angular distribution proportional to $\cos^2\theta_{K^+}$. Flat distributions were included for the small background contribution. The normal spin-parity assignments are consistent with the data.

The production cross section times branching ratio is calculated from the observed number of $D_s^+ \to \phi\pi^+$ decays ($N_{\rm obs} = 26.7 \pm 5.2$), the integrated luminosity ($\mathcal{L} = 6.30 \pm 0.46\,{\rm pb}^{-1}$), and the detection efficiency ($\epsilon = 7.1\%$, including the $\phi \to K^+K^-$ branching fraction). I assume $B(D_s^{*+} \to \gamma D_s^+) = 100\%$. Since each $e^+e^- \to D_s^* D_s$ event contains two D_s's, we have $N_{\rm obs} = 2\sigma\mathcal{L}B(D_s^+ \to \phi\pi^+)\epsilon$ or

$$\sigma(e^+e^- \to D_s^{*+}D_s^- + D_s^{*-}D_s^+)B(D_s^+ \to \phi\pi^+) = \frac{N_{\rm obs}}{2\mathcal{L}\epsilon} = 30 \pm 6 \pm 11\,{\rm pb}.$$

The systematic error includes uncertainties in the reconstruction efficiency (31%), the background shape (15%), and the integrated luminosity (7%). The contribution to the peak from $D_s^+ \to \bar{K}^{*0}K^+$ and from non-resonant $D_s^+ \to K^+K^-\pi^+$ decays is negligible.

The D_s^* mass is determined from the recoil mass spectrum of D_s candidates. The resolution is improved by using the nominal D_s^+ mass,[60] $1971.4\,{\rm MeV}/c^2$, rather that the reconstructed value in the calculation of the recoil mass (Section 3.1). The constrained recoil mass distribution for $\phi\pi^+$ combinations in the D_s mass region is shown in Fig. 4.6. The signal shape assumed in the fit is taken from a Monte Carlo simulation which includes initial-state radiation.[61] The width and location of the broad contribution from secondary D_s's are constrained in the fit to vary properly as

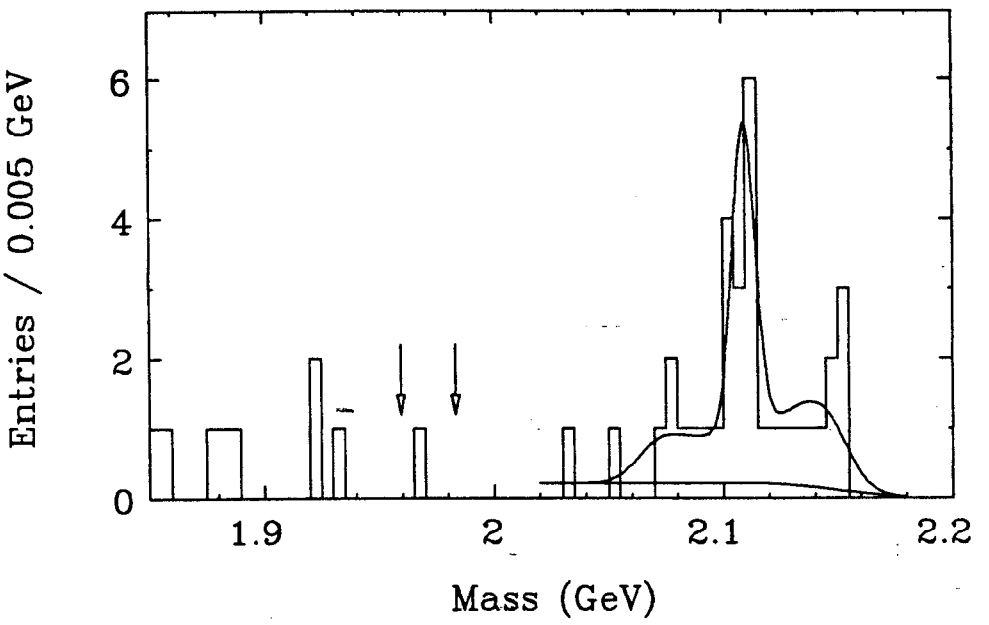

Figure 4.6 $M_{\rm cr}$ distribution for $1.92 < M(\phi\pi^+) < 2.02\,{\rm GeV}/c^2$. $D_s^+ D_s^-$ production would produce a signal in the interval indicated by the arrows.

the mass of the narrow primary peak [$= M(D_s^*)$] is varied. The background shape is obtained from ϕ sidebands; the normalization of the background is estimated from the fit to Fig. 4.4. The result is

$$M(D_s^*) = 2109.3 \pm 2.1 \pm 3.1\,{\rm MeV}/c^2.$$

The systematic error includes contributions from the uncertainties in the D_s^+ mass ($1.7\,{\rm MeV}/c^2$), the center-of-mass energy ($1.7\,{\rm MeV}/c^2$), the effects of the radiative corrections ($1.2\,{\rm MeV}/c^2$), the selection criteria ($1.5\,{\rm MeV}/c^2$), the background shape ($0.5\,{\rm MeV}/c^2$), and the momentum scale ($0.1\,{\rm MeV}/c^2$). The D_s^*-D_s mass difference is then

$$M(D_s^*) - M(D_s) = 137.9 \pm 2.1 \pm 4.3\,{\rm MeV}/c^2.$$

The D_s^* mass obtained with this technique is anti-correlated with the input

value of D_s mass: $\delta M(D_s^*) \cong -\delta M(D_s)$. Making use of the more precise D_s mass measurements which are now available (world average $= 1969.4 \pm 1.0\,\mathrm{MeV}/c^2$ [5]), we obtain

$$M(D_s^*) = 2111.3 \pm 2.1 \pm 2.8\,\mathrm{MeV}/c^2;$$

$$M(D_s^*) - M(D_s) = 141.9 \pm 2.1 \pm 3.3\,\mathrm{MeV}/c^2.$$

The systematic errors are

$$\sigma^2[M(D_s^*)] = (2.6\,\mathrm{MeV}/c^2)^2 + \sigma^2[M(D_s)],$$

$$\sigma^2[M(D_s^*) - M(D_s)] = (2.6\,\mathrm{MeV}/c^2)^2 + 4\sigma^2[M(D_s)].$$

Two other results are obtained from the M_{cr} spectrum of the $D_s^+ \to \phi\pi^+$ candidates. By fitting the D_s^* peak with a Breit-Wigner resonance function instead of a Gaussian, an upper limit of $22\,\mathrm{MeV}/c^2$ (90% CL) is obtained for the width of the D_s^*. An upper limit on $D_s^+ D_s^-$ production relative to $D_s^{*\pm} D_s^{\mp}$ is also established from Fig. 4.6. No enhancement is seen at $M_{\mathrm{cr}} = M(D_s^+)$; a $\pm 12\,\mathrm{MeV}/c^2$ interval centered on the D_s^+ mass, which would include 90% of an expected signal, contains one event. The 90% CL upper limit on the number of signal events is 3.89. The detection efficiency is 6.3%. This yields

$$\frac{\sigma(e^+e^- \to D_s^+ D_s^-)}{\sigma(e^+e^- \to D_s^{*+} D_s^- + D_s^{*-} D_s^+)} < \frac{3.89}{26.7} \times \frac{7.1\%}{6.3\%} \times 1.25$$

$$< 0.21 \quad (90\%\ \mathrm{CL}).$$

The factor of 1.25 is included to account for the following: statistical uncertainty (19%) and uncertainty in the background shape (15%) for the $D_s^* D_s$ analysis, and Monte Carlo statistics (5.7%). The quadratic sum of these contributions is 25%.

4.3 New Determination of $\sigma(D_s^* D_s) \times B(D_s^+ \to \phi\pi^+)$

This reanalysis of the $D_s^+ \to \phi\pi^+$ decay mode was undertaken to permit more precise determinations of other D_s branching ratios relative to $\phi\pi^+$. It was desirable to use the same analysis techniques as for the other modes, in order to make the systematic errors on the relative branching ratios as small and as straightforward to determine as possible. Mark III searches for $D_s^+ \to \bar{K}^{*0}K^+$, $\bar{K}^0K^+$, and other final states have relied on kinematic fitting to reduce backgrounds and improve the mass resolution. This method is now applied to $D_s^+ \to \phi\pi^+$, with other refinements which were described in Chapter 3.

Candidate pions and kaons are chosen by the following criteria. Tracks must have helix fits, pass within 20 mm of the beam axis, and satisfy $|\cos\theta| < 0.85$, where θ is the angle between a track and the z axis. Energy-loss corrections are made and the *beam fitter* is used to constrain each track to originate within the beam spot in the xy-plane. The χ^2 CL for these fits must be greater than 10^{-4} for each track.

The TOF system is used for particle identification. TOF information is accepted if a drift chamber track is projected to enter a TOF counter ($|z_{\rm tof}| < 1.50\,$m), and if the TOF measurement has a good quality flag. All tracks with $|t - t_K|/\sigma_K < 5$ and

$$\frac{t - t_\pi}{\sigma_\pi} + \frac{t - t_K}{\sigma_K} > 0$$

are accepted as kaon candidates.[⋆] All other tracks are used as pion candidates.

Each $K^+K^-\pi^+$ combination is kinematically fitted to the hypothesis $e^+e^- \to K^+K^-\pi^+D_s^{*-}$. The D_s^{*-} is not reconstructed, but the constraint $M_{\rm rec} = M(D_s^*) =$

⋆ If $\sigma_\pi \cong \sigma_K$ the latter requirement corresponds to $t > \frac{1}{2}(t_\pi + t_K)$.

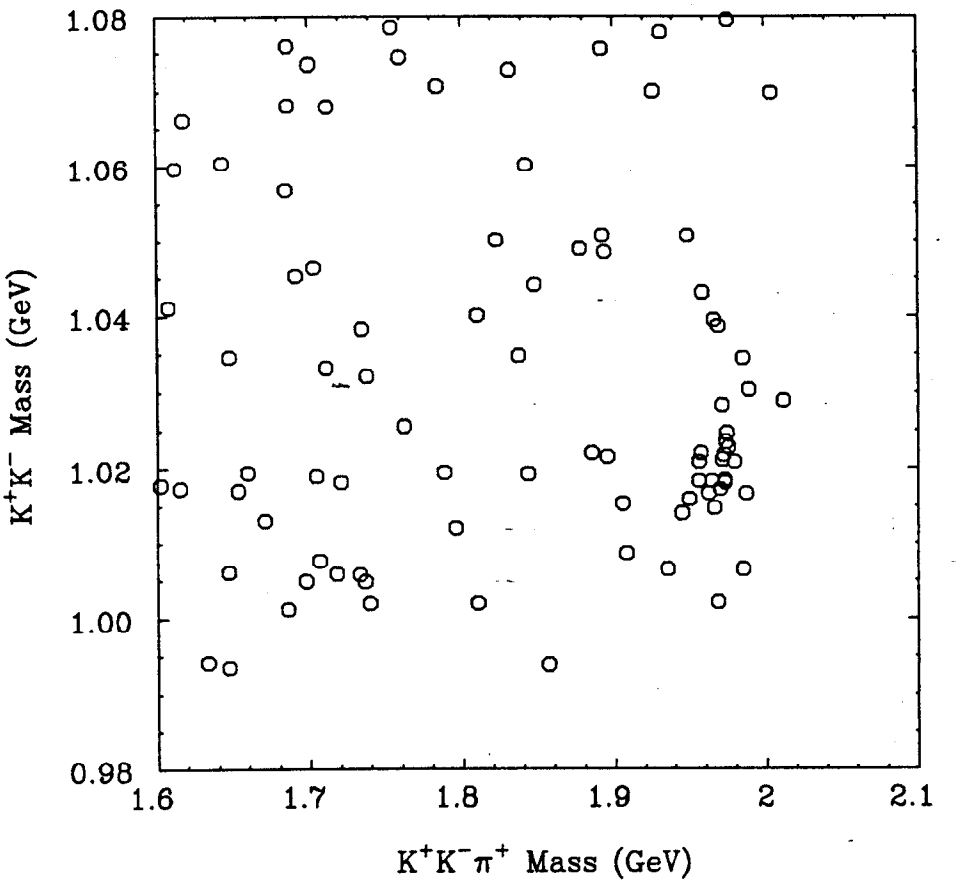

Figure 4.7 $M(K^+K^-)$ *vs.* $M(K^+K^-\pi^+)$ after the kinematic fit.

$2.1093\,\mathrm{GeV}/c^2$ is imposed, requiring CL $> 1\%$. The fit hypothesis is correct only for decays of primary D_s's; the fit reduces the reconstruction efficiency for secondary decays by one-fifth relative to primary decays. The mass resolution for events in which the primary D_s is reconstructed is $\sim 4\,\mathrm{MeV}/c^2$, whereas candidates from the secondary D_s which are not rejected by the fit form a broader mass distribution extending $\pm 50\,\mathrm{MeV}/c^2$ about the D_s mass.

The fitted K^+K^- mass *vs.* $K^+K^-\pi^+$ mass is plotted in Fig. 4.7, showing a clear $D_s^+ \to \phi\pi^+$ signal. After a $\pm 15\,\mathrm{MeV}/c^2$ cut around the ϕ, the $M(\phi\pi^+)$ distribution shown in Fig. 4.8 is obtained.

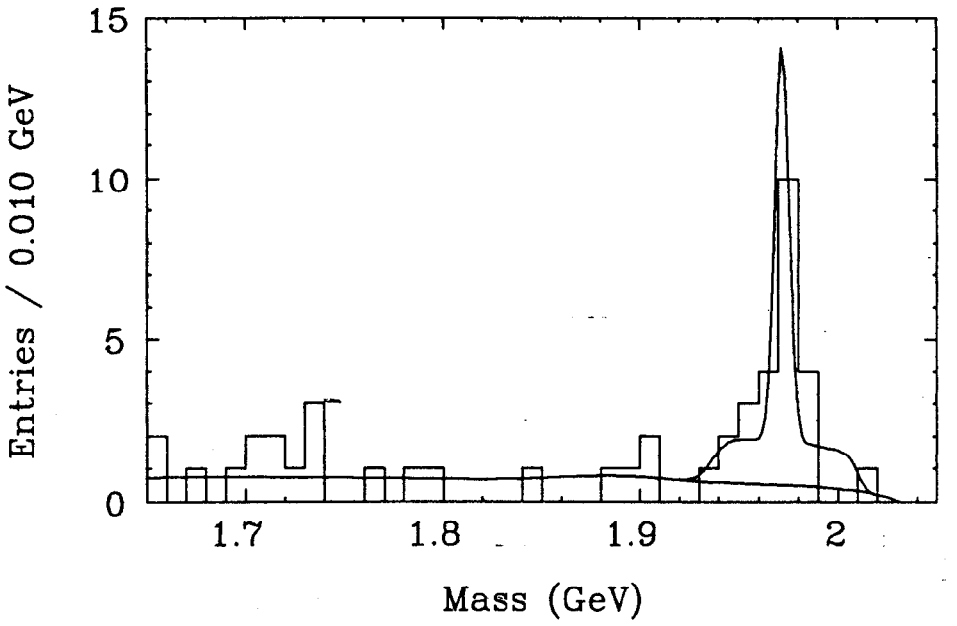

Figure 4.8 Fitted $\phi\pi^+$ mass spectrum.

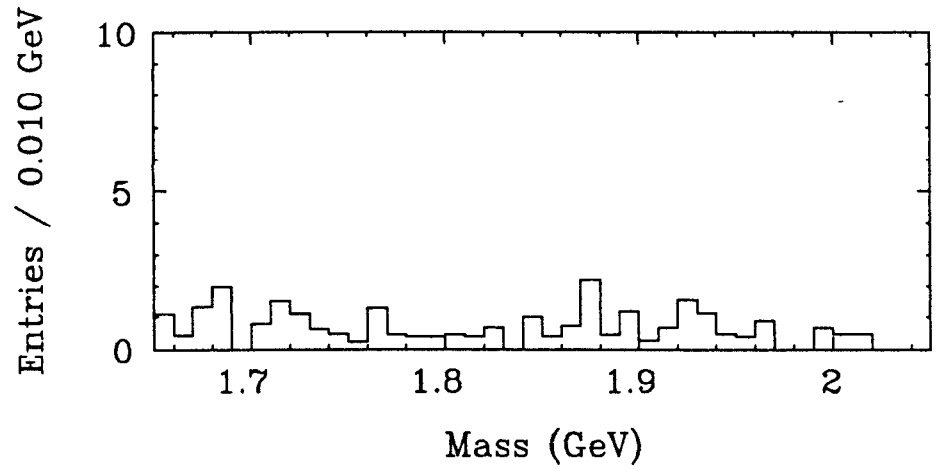

Figure 4.9 Background distribution predicted from Monte Carlo simulation of $D^*\bar{D}^*$, $D^*\bar{D}$, $D\bar{D}$, and non-charm continuum events, normalized to the integrated luminosity of the data set.

The shape of the background is taken from Fig. 4.9, which shows the sum of the predicted contributions from non-charm continuum events and D decays. Allowance is made for the $D^+ \to \phi\pi^+$ signal, which is reduced and distorted by the

kinematic fit. The total of these contributions agrees with the observed number of background entries. Nevertheless, the normalization of the background is allowed to vary in the fit. The shapes and relative amounts of the primary and secondary signal contributions are also obtained by Monte Carlo calculation.

The signal contains 20.4 ± 4.5 events. The Monte Carlo efficiency is 6.32% for $\phi\pi^+$. I obtain

$$\sigma(e^+e^- \to D_s^{*+}D_s^- + D_s^{*-}D_s^+)B(D_s^+ \to \phi\pi^+) = 26 \pm 6 \pm 5\,\text{pb}.$$

Contributions to the systematic error are from:

- the integrated luminosity (7%);
- tracking efficiency (3%);
- track selection criteria (3%);
- TOF modelling (13%);
- 1C fit χ^2 cut (3%);
- Monte Carlo statistics (2%);
- background shape (12%);
- $B(\phi \to K^+K^-)$ (3%).

Adding these in quadrature gives a total systematic error of 21%. The trigger, pre-filter, and hadron filter are $>99.5\%$ efficient for $D_s^+ \to \phi\pi^+$ decays which satisfy the other selection requirements; the systematic uncertainty from these sources is negligible. The efficiencies of the track selection and identification criteria are compared to the Monte Carlo efficiencies in studies of $D^0 \to K^-\pi^+$. The kinematic fit χ^2 cut is checked using dimuon events.

5
Analysis of $D_s^+ \to \bar{K}^{*0}K^+$

5.1 Introduction

In this chapter I describe the Mark III $D_s^+ \to \bar{K}^{*0}K^+$ analysis, which is very similar to the $\phi\pi^+$ study of Chapter 4. The $M(\bar{K}^{*0}K^+)$ and $M_{\rm rec}$ distributions are examined to find evidence for $D_s^{*\pm}D_s^{\mp}$ production. The kinematic fitting procedure of Section 4.3 is then applied to determine σB and hence $B(D_s^+ \to \bar{K}^{*0}K^+)/B(D_s^+ \to \phi\pi^+)$.

The decay $D_s^+ \to \bar{K}^*(892)^0K^+ \to K^+K^-\pi^+$ was first observed by ARGUS.[62] They observed $87.2^{+19.1}_{-21.0}$ events, and found $B(D_s^+ \to \bar{K}^{*0}K^+)/B(D_s^+ \to \phi\pi^+) = 1.44 \pm 0.37$. A preliminary Mark III result was reported in 1986.[63]

5.2 Measurement of $\sigma(D_s^*D_s) \times B(D_s^+ \to \bar{K}^{*0}K^+)$

The analysis of $D_s^+ \to \bar{K}^{*0}K^+$ is done with the same track selection and particle identification criteria as were used for $D_s^+ \to \phi\pi^+$ (Section 4.3). The inclusive $K^-\pi^+$ mass spectrum is shown in Fig. 5.1. A $\bar{K}^*(892)^0$ signal of 5940 ± 370 entries is observed. Combinations in the mass region $0.821 < M(K^-\pi^+) < 0.971\,{\rm GeV}/c^2$

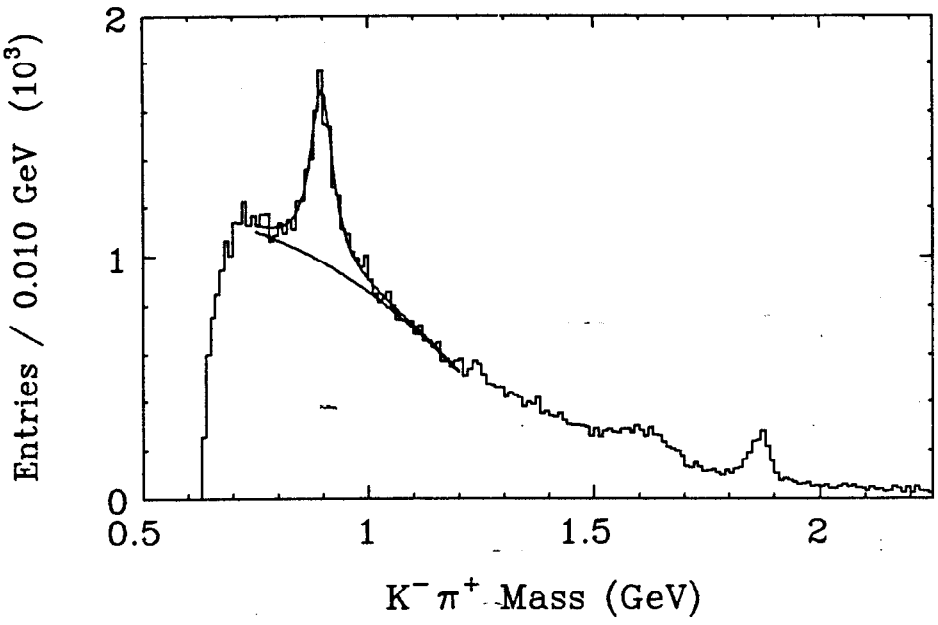

Figure 5.1 Inclusive $K^-\pi^+$ mass spectrum. The enhancements in the high mass region result from $D \to \bar{K}\pi\pi$ and $D \to \bar{K}\pi$.

are selected as $\bar{K}^{*0}$ candidates and all $\bar{K}^{*0}K^+$ combinations are formed. For $D_s^+ \to \bar{K}^{*0}K^+$, the angle θ_π of the π^+ in the $\bar{K}^{*0}$ helicity frame has a $\cos^2\theta_\pi$ distribution; the requirement $|\cos\theta_\pi| > 0.3$ is imposed to reduce background. The resulting scatter plot of $M(\bar{K}^{*0}K^+)$ *vs.* $M_{\rm rec}$ is shown in Fig. 5.2. The $M_{\rm rec}$ distribution shown in Fig. 5.3 results when the region $1.94 < M(\bar{K}^{*0}K^+) < 2.00\,{\rm GeV}/c^2$ is selected. The $M(\bar{K}^{*0}K^+)$ distribution for $M_{\rm rec}$ between 2.06 and $2.16\,{\rm GeV}/c^2$ is shown in Fig. 5.4. Evidence for a $D_s^* D_s$ signal is seen.

As in the $\phi\pi^+$ analysis, it is advantageous to use kinematic fitting to reduce backgrounds and improve the $\bar{K}^{*0}K^+$ mass resolution. All $K^+K^-\pi^+$ combinations are again formed and each is fitted to the hypothesis $e^+e^- \to K^+K^-\pi^+D_s^{*-}$, where the unobserved D_s^{*-} represents a recoil mass constraint. Because the background level is much higher than for $D_s^+ \to \phi\pi^+$, the requirement ${\rm CL}(\chi^2) > 10\%$ is used. The fitted track four-momenta are used for the remaining calculations. A scatter

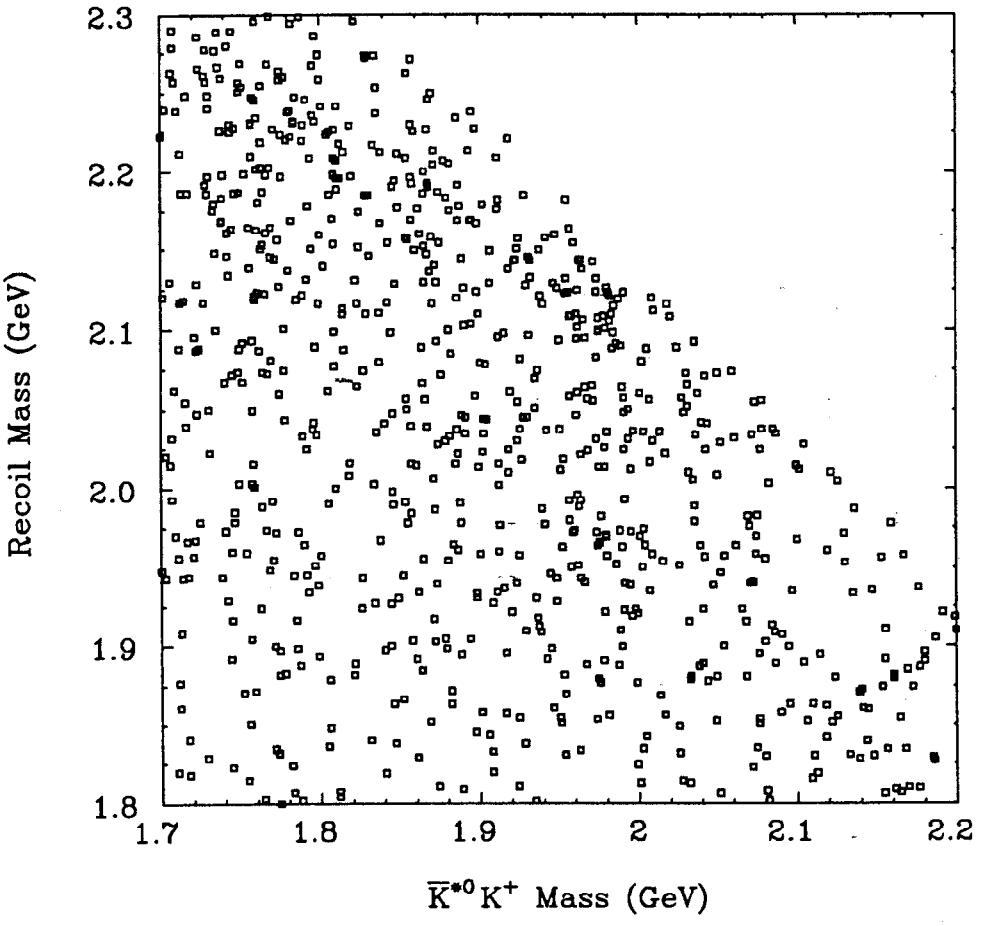

Figure 5.2 $M(\bar{K}^{*0}K^+)$ *vs.* $M_{\rm rec}$.

plot of $M(K^-\pi^+)$ *vs.* $M(K^+K^-\pi^+)$ is displayed in Fig. 5.5. A $\bar{K}^{*0}$ band appears across the plot, with an enhancement at the D_s^+ mass. Combinations are chosen with fitted $K^-\pi^+$ mass between 0.821 and 0.971 GeV/c^2. The $\cos\theta_\pi$ distribution is found to be consistent with expectations [Fig. 5.6]; the requirement $|\cos\theta_\pi| > 0.3$ is imposed for the measurement of σB. The resulting $\bar{K}^{*0}K^+$ mass plot is shown in Fig. 5.7.

The spectrum is fitted by the procedure used in the $\phi\pi^+$ analysis. The signal shape is obtained by Monte Carlo simulation of primary and secondary D_s^+ produc-

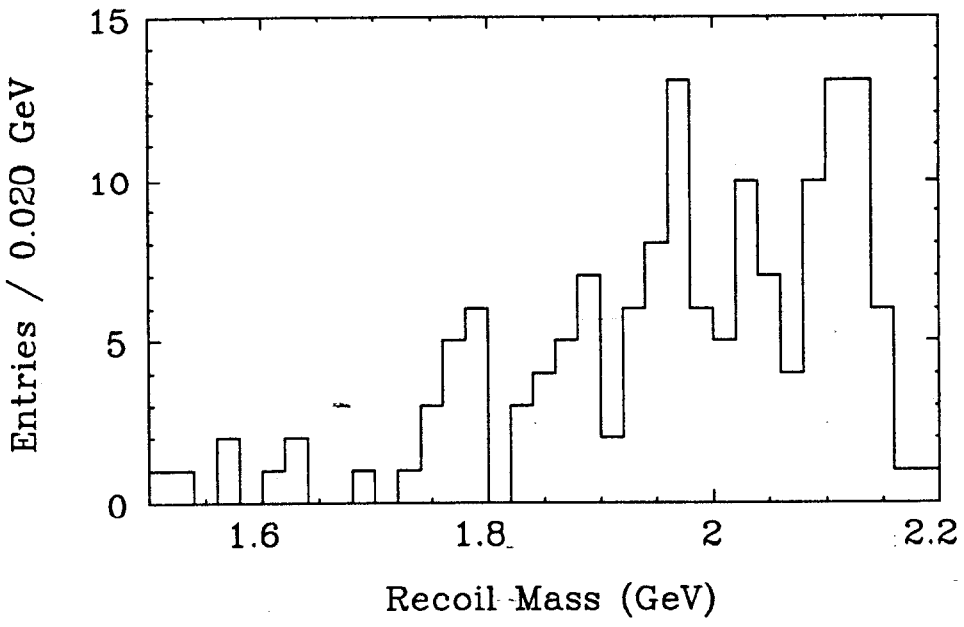

Figure 5.3 $M_{\rm rec}$ distribution for $1.94 < M(\bar{K}^{*0}K^{+}) < 2.00\,{\rm GeV}/c^2$.

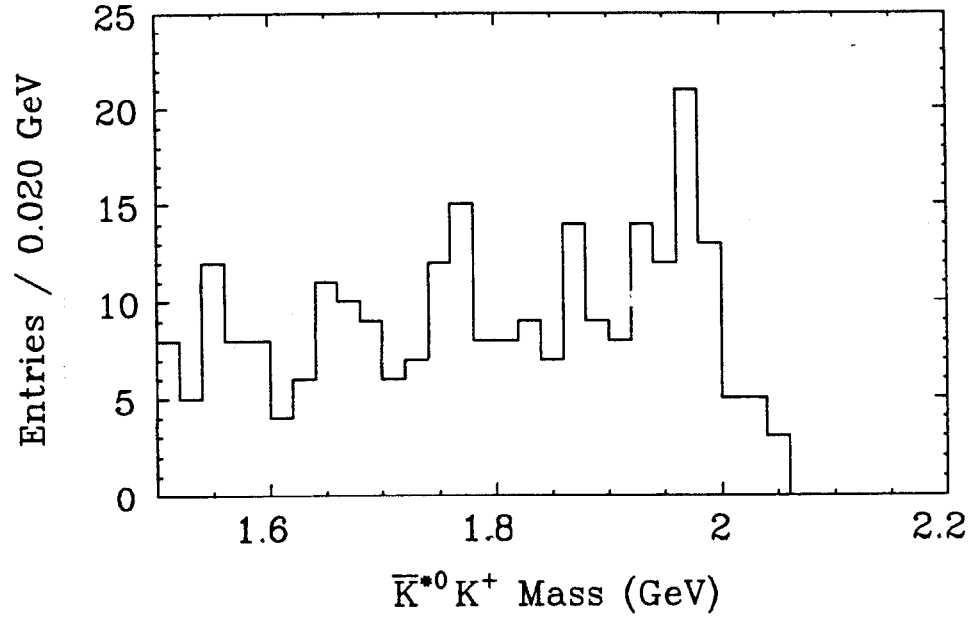

Figure 5.4 $M(\bar{K}^{*0}K^{+})$ distribution for $2.06 < M_{\rm rec} < 2.16\,{\rm GeV}/c^2$.

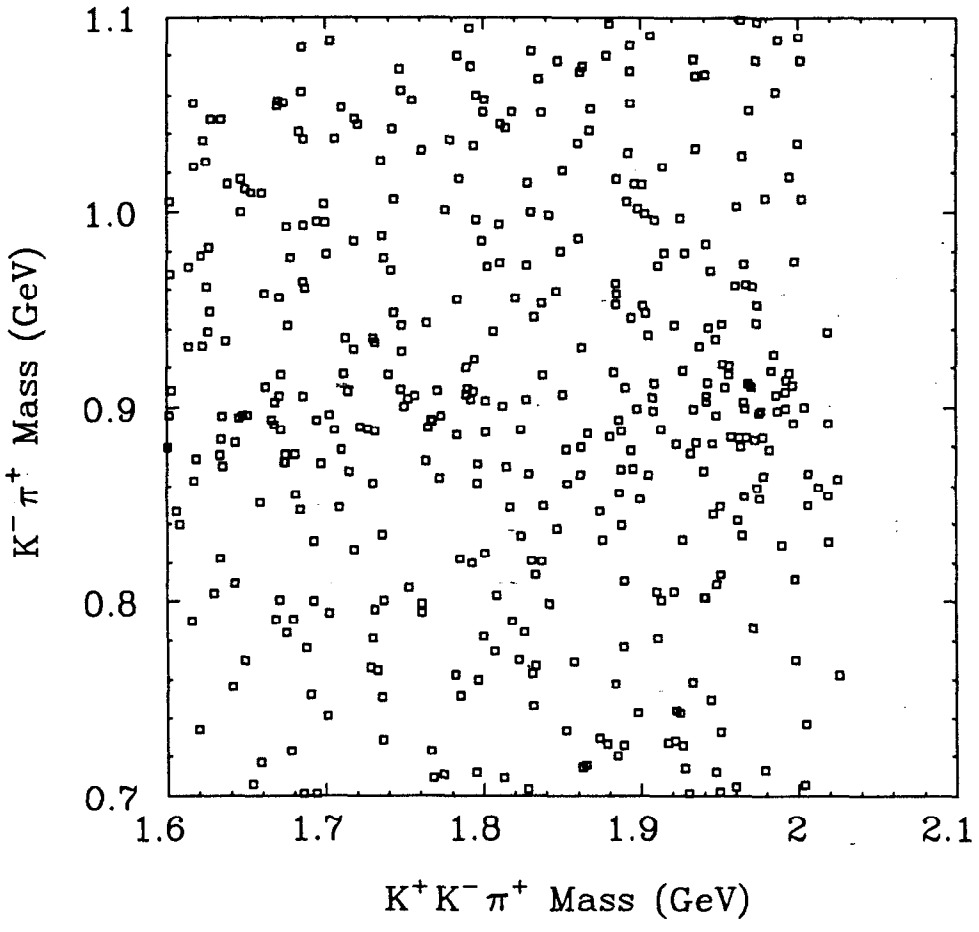

Figure 5.5 $M(K^-\pi^+)$ *vs.* $M(K^+K^-\pi^+)$ after the kinematic fit.

tion, with $D_s^+ \to \bar{K}^{*0}K^+$. The shape of the background is taken from Monte Carlo $D^*\bar{D}^*$, $D^*\bar{D}$, $D\bar{D}$, and non-charm continuum events [Fig. 5.8]. The total of these contributions is again consistent with the observed number of background entries, but the normalization of the background is allowed to vary in the fit. The signal contains 23.8 ± 6.3 events. A subtraction is made for two sources of background which produce enhancements at or near the D_s^+ mass: $D^+ \to \bar{K}^{*0}\pi^+$ (0.8 ± 0.6 events[64]) and non-resonant $D_s^+ \to K^+K^-\pi^+$ (1.8 ± 0.8 events[65]). The decay $D_s^+ \to \phi\pi^+$ is excluded by the $\bar{K}^{*0}$ requirement on the $K^-\pi^+$ mass. The detection efficiency for

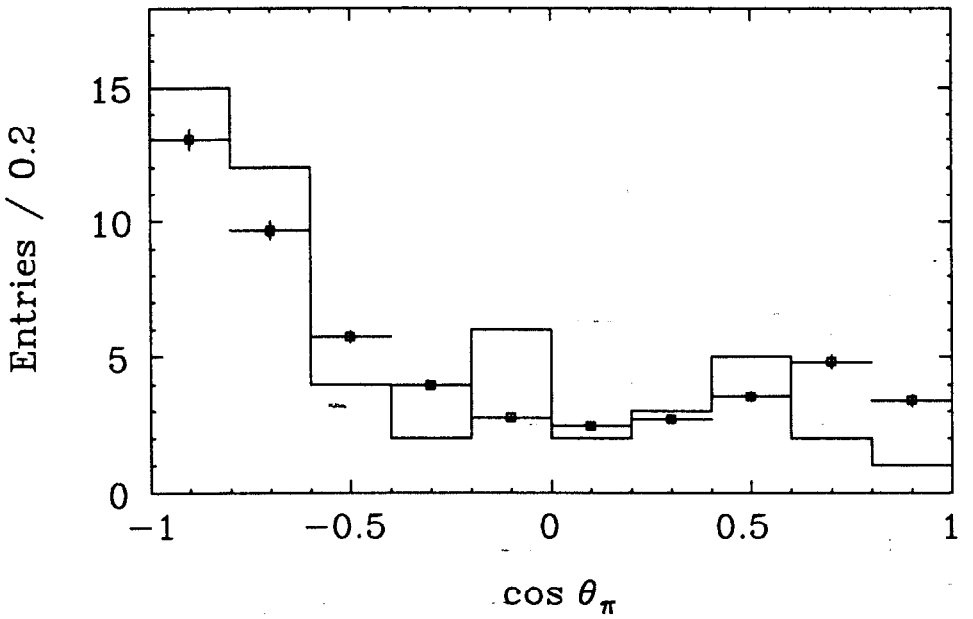

Figure 5.6 Distribution of $\cos\theta_\pi$ for data (histogram) and Monte Carlo (points). A linearly decreasing contribution to account for the background has been added to the Monte Carlo. The shape of the background contribution is taken from a $\bar{K}^{*0}K^+$ mass sideband and from D Monte Carlo; the relative amounts of signal and background (53%:47%) is taken from a fit to the $\bar{K}^{*0}K^+$ mass spectrum.

$D_s^+ \to \bar{K}^{*0}K^+$, including $B(\bar{K}^{*0} \to K^-\pi^+)$, is 7.8%, yielding

$$\sigma(e^+e^- \to D_s^{*+}D_s^- + D_s^{*-}D_s^+)B(D_s^+ \to \bar{K}^{*0}K^+) = 22 \pm 6 \pm 6\,\text{pb}.$$

Contributions to the systematic error are from:

- the integrated luminosity (7%);
- tracking efficiency (3%);
- track selection criteria (3%);
- TOF modelling (8%);
- 1C fit χ^2 cut (11%);
- Monte Carlo statistics (2%);

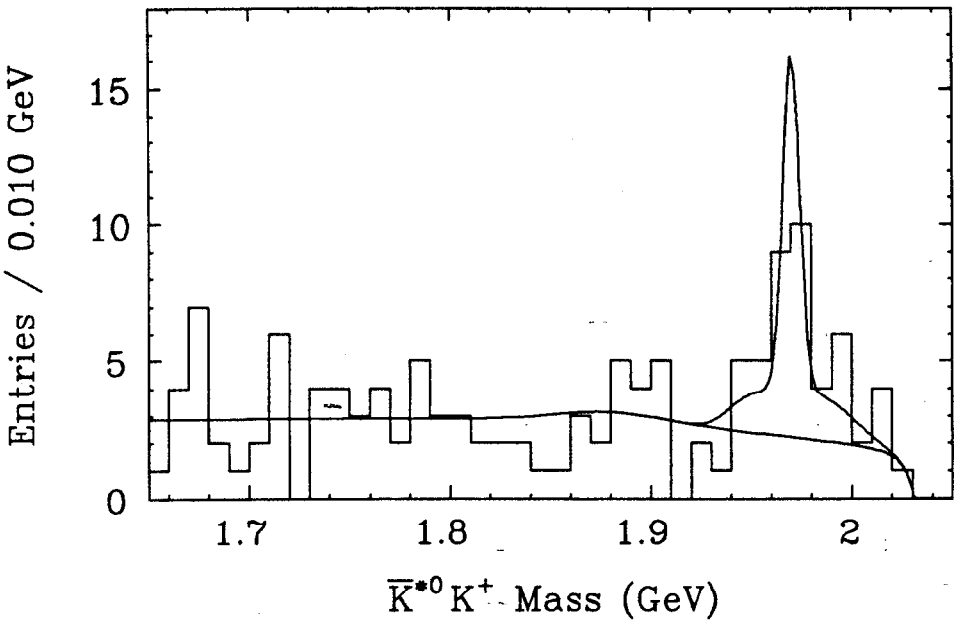

Figure 5.7 $M(\bar{K}^{*0}K^+)$ spectrum after the kinematic fit, requiring $|\cos\theta_\pi| > 0.3$.

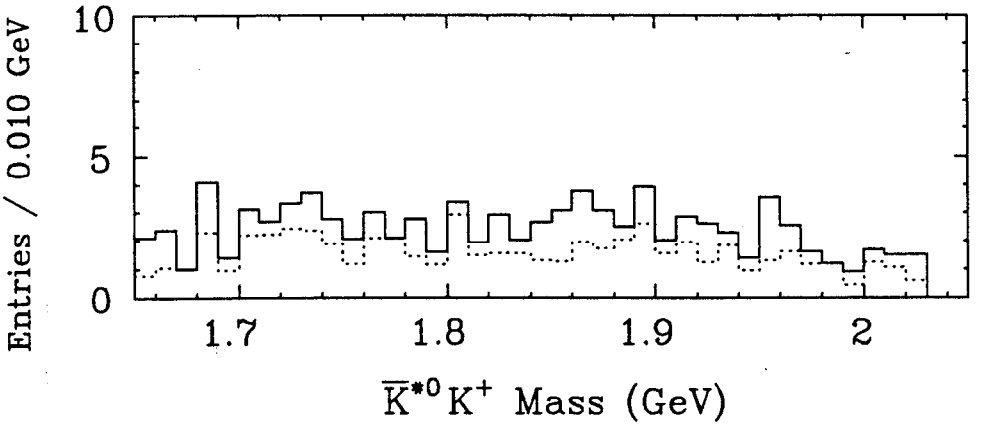

Figure 5.8 Background distributions predicted by Monte Carlo simulation, normalized to the integrated luminosity of the data set. The dotted histogram shows the contribution from $D^*\bar{D}^*$, $D^*\bar{D}$, and $D\bar{D}$ events; the solid histogram gives the total for these final states and non-charm continuum events.

- background shape (21%);
- $D_s^+ \to K^+K^-\pi^+$ subtraction (4%);
- $D^+ \to \bar{K}^{*0}\pi^+$ subtraction (3%).

The trigger, filter, and post-filter efficiency errors are again negligible. By adding the relative errors in quadrature, I obtain a total systematic error of 33%.

5.3 Determination of $B(D_s^+ \to \bar{K}^{*0}K^+)/B(D_s^+ \to \phi\pi^+)$

The ratio of the central values of $\sigma B(\bar{K}^{*0}K^+)$ and $\sigma B(\phi\pi^+)$ is 0.84. The relative statistical errors on the σB's are added in quadrature to obtain $(26.6\%)^2 + (24.2\%)^2 = (36.0\%)^2$. Contributions to the systematic error which do not cancel in the ratio are:

- ToF modelling (5%);
- 1-C fit χ^2 cut (8%);
- Monte Carlo statistics (3%);
- Background shapes (added in quadrature) (24%);
- $D_s^+ \to K^+K^-\pi^+$ subtraction (4%);
- $D^+ \to \bar{K}^{*0}\pi^+$ subtraction (3%);
- $B(\phi \to K^+K^-)$ (3%).

These items (added in quadrature) give a relative systematic error of 27%. The relative branching fraction is

$$\frac{B(D_s^+ \to \bar{K}^{*0}K^+)}{B(D_s^+ \to \phi\pi^+)} = 0.84 \pm 0.30 \pm 0.22.$$

6
D_s^+ Absolute Hadronic Branching Fractions

6.1 Introduction

Estimates of the D_s^+ absolute hadronic branching fractions can been made from measurements of σB in e^+e^- annihilation far above charm threshold, with some assumptions about the D_s^+ cross section. For example, CLEO[17] obtained

$$\sigma(D_s) = 3.0\,\text{nb} \times \frac{4}{10} \times 2 \times 0.15 = 0.36\,\text{nb},$$

where 3.0 nb is the measured total hadronic cross section, $\frac{4}{10}$ is the fraction of hadronic events containing charm, 2 is the number of charmed particles per $c\bar{c}$ event, and 0.15 is the assumed probability that the charm quark will pair with a strange quark "popped" from the vacuum. For comparison with experiments at other center-of-mass energies, we compute the quantity

$$R(D_s) \equiv \frac{\sigma(D_s)}{\sigma_{\mu\mu}} = 0.46,$$

which is approximately independent of $\sqrt{s}$ in this simple picture. The existing measurements of $R(D_s) \times B(D_s^+ \to \phi\pi^+)$ and the corresponding estimates of $B(D_s^+ \to \phi\pi^+)$ are listed in Table 6.1. A value of $B(D_s^+ \to \phi\pi^+) = 2$–$3\%$ is indicated.

Table 6.1 Estimates of $B(D_s^+ \to \phi\pi^+)$ from high energy e^+e^- annihilation. Brackets indicate my own estimates; the other numbers are contained in or inferred from the references.

Experiment	Reference	$\sqrt{s}$ (GeV)	$R(D_s) \times B_{\phi\pi^+}$ (%)	$R(D_s)$	$B_{\phi\pi^+}$ (%)
CLEO	17	10	2.1	0.46	4.4
	66	10	$0.92 \pm 0.23 \pm 0.13$	[0.46]	$[2.0 \pm 0.5 \pm 0.3]$
TASSO	28	30–42	$6.4 \pm 1.3 \pm 1.9$	0.487	$13 \pm 3 \pm 4$
	67	35–44	1.6	0.48	$3.3 \pm 1.6 \pm 1.0$
ARGUS	31, 68	10	$1.47 \pm 0.32 \pm 0.20$	0.54	3.0 ± 0.8
	69	10	$0.94 \pm 0.10 \pm 0.16$	[0.54]	$[1.7 \pm 0.2 \pm 0.3]$
HRS	30	29	1.35 ± 0.34[a]	0.39[a]	3.3 ± 1.1
	70	29	1.13 ± 0.30[a]	0.39[a]	2.8 ± 1.0

[a] $z \equiv E/E_{\rm beam} > 0.4$.

The final analysis topic covered in this thesis is an attempt to measure absolute hadronic D_s^+ branching fractions by searching for fully reconstructed $e^+e^- \to D_s^{*\pm}D_s^{\mp} \to \gamma D_s^+ D_s^-$ events. The expected number of events with $D_s^+ \to$ *Mode* i and $D_s^- \to$ *Mode* j is proportional to $\sigma B_i B_j$, where $\sigma \equiv \sigma(D_s^{*\pm}D_s^{\mp})$ and $B_i \equiv B(D_s^+ \to$ *Mode* $i)$. It is therefore possible (in principle) to use "double tag" events, along with the measured relative D_s^+ branching fractions and $\sigma B_{\phi\pi^+}$, to determine the B_i. Before describing the procedure I summarize the existing D_s^+ relative branching fraction measurements and limits [Table 6.2]. The absence of the annihilation decays to $\rho^0\pi^+$ and $\omega\pi^+$ is particularly interesting. It is important to resolve the disagreement in the $\eta\pi^+$ results, and to confirm the unexpectedly large $\eta'\pi^+$ measurements.

Table 6.2 D_s^+ relative branching fractions, 1989.

D_s^+ Decay mode	$B/B(D_s^+ \to \phi\pi^+)$	Reference
$\phi\pi^+$	1	–
$\bar{K}^{*0}K^+$	1.44 ± 0.37	62
	$0.87 \pm 0.13 \pm 0.05$	65
	$0.89 \pm 0.32 \pm 0.13$	57
	0.93 ± 0.37	58
	$0.84 \pm 0.30 \pm 0.22$	a
$\phi\pi^+\pi^+\pi^-$	$1.11 \pm 0.37 \pm 0.28$	31
	$0.41 \pm 0.13 \pm 0.11$	69
	$0.42 \pm 0.13 \pm 0.07$	65
	$0.39 \pm 0.17 \pm 0.06$	57
$\bar{K}^0K^+$	$0.92 \pm 0.32 \pm 0.20$	71
$f_0(975)\pi^+$	$0.28 \pm 0.10 \pm 0.03$	23
$\bar{K}^{*0}K^{*+}$	$2.3 \pm 1.2 \pm 0.8$	57
$\phi\pi^+\pi^0$	< 3.5 (90% CL)	58
	$2.4 \pm 1.0 \pm 0.5$	25
	< 2.5 (90% CL)	72
$K^+K^-\pi^+$ non-resonant	$0.25 \pm 0.07 \pm 0.05$	65
	$0.96 \pm 0.32 \pm 0.14$	57
$K^+K^-\pi^+\pi^+\pi^-$ non-resonant	< 0.32 (90% CL)	65
	$0.11 \pm 0.07 \pm 0.02$	57
$\pi^+\pi^+\pi^-$	$0.44 \pm 0.10 \pm 0.04$	23
$\pi^+\pi^+\pi^-$ non-resonant	$0.29 \pm 0.09 \pm 0.03$	23
$\pi^+\pi^+\pi^+\pi^-\pi^-$	< 0.29 (90% CL)	23
$\eta\pi^+$	~ 3	73
	$2.5 \pm 0.8 \pm 0.8$	74
	< 1.5 (90% CL)	25
$\eta'\pi^+$	~ 5	73
	5.7 ± 1.5	72
$\rho^0\pi^+$	< 0.22 (90% CL)	24
	< 0.08 (90% CL)	23
$\omega\pi^+$	< 0.5 (90% CL)	25
$\pi^+\pi^+\pi^-\pi^0$	< 3.3 (90% CL)	25
$K^+K^-\pi^+\pi^0$ (non-ϕ)	< 2.4 (90% CL)	25
$K^0\pi^+$	< 0.21 (90% CL)	71

[a] Chapter 5 of this thesis.

6.2 Search for Double Tag Events

Many D_s^+ decay modes have been included in this study, in order to maximize the sensitivity. They are:

1. $\phi\pi^+$, $\phi \to K^+K^-$;
2. $\bar{K}^0K^+$, $\bar{K}^0 \to K_S^0 \to \pi^+\pi^-$;
3. $f_0(975)\pi^+$, $f_0 \to \pi^+\pi^-$;
4. $\bar{K}^{*0}K^+$, $\bar{K}^{*0} \to K^-\pi^+$;
5. $\bar{K}^{*0}K^{*+}$, $\bar{K}^{*0} \to K^-\pi^+$, $K^{*+} \to K^0\pi^+$, $K^0 \to K_S^0 \to \pi^+\pi^-$;
6. $\phi\pi^+\pi^+\pi^-$, $\phi \to K^+K^-$;
7. $\phi\pi^+\pi^0$, $\phi \to K^+K^-$, $\pi^0 \to \gamma\gamma$;
8. $\eta\pi^+$, $\eta \to \gamma\gamma$;
9. $\eta\pi^+$, $\eta \to \pi^+\pi^-\pi^0$, $\pi^0 \to \gamma\gamma$;
10. $\eta'\pi^+$, $\eta' \to \gamma\rho^0$;
11. $\eta'\pi^+$, $\eta' \to \eta\pi^+\pi^-$, $\eta \to \gamma\gamma$.

Three groups of double tag modes are studied. Group 1 consists of all combinations

$$e^+e^- \to D_s^{*\pm}D_s^{\mp} \to \gamma(D_s^+ \to \textit{Mode } i)(D_s^- \to \textit{Mode } j),$$

where $i, j = 1, 2, \ldots, 7$. This group contains a total of 28 different final states (not counting charge conjugate states). Because of the current interest in the $D_s^+ \to \eta\pi^+$ and $\eta'\pi^+$ decays, these channels are considered separately. Group 2 comprises the double tag modes with $i = 1, 2, \ldots, 7$ and $j = 8, 9$ ($\eta\pi^+$), and their charge conjugates (14 final states). Group 3 represents $i = 1, 2, \ldots, 7$ and $j = 10, 11$ ($\eta'\pi^+$, 14 final states). No assumption is made about the branching fractions for $D_s^+ \to \eta\pi^+$ and $\eta'\pi^+$ relative to the other channels.

Since a very small number of signal events is expected, the selection criteria are chosen to maximize the detection efficiency. For some final states it is necessary to tighten the particle identification cuts to reduce the combinatoric background to a manageable level. Kinematic fitting is employed to improve the resolution and reduce backgrounds. No significant double tag signal is seen. The results from the three groups yield upper limits on $B_{\phi\pi^+}$, $B_{\eta\pi^+}$, and $B_{\eta'\pi^+}$, respectively. $D^{*0}\bar{D}^0$ events are also studied as a test of the technique.

The search for a particular double tag mode,

$$e^+e^- \to D_s^{*\pm}D_s^{\mp},$$
$$D_s^{*\pm} \to \gamma D_s^{\pm},$$
$$D_s^+ \to \textit{Mode } i,$$
$$D_s^- \to \textit{Mode } j,$$

begins with the selection of events having the correct number of charged tracks. Reconstructed track candidates are required to pass within 6 cm of the beam axis, with $|z| < 15$ cm at the point of closest approach. This cut removes debris from $K^{\pm}$ decays and calorimeter "splash-backs," while rejecting few $K_S^0 \to \pi^+\pi^-$ decays. All accepted tracks must have helix fits, and their total charge must be zero.

All neutral showers in the calorimeters are accepted as γ candidates. Events containing fewer photons than the desired final state are rejected. No restriction is imposed on extra photons because spurious showers may be created by $K^{\pm}$ decay products, electronics noise, and hadronic shower "split-offs." In the Monte Carlo, kaon decays are only generated inside the drift chamber, and no attempt is made to simulate the other phenomena.

Selection of charged π and K candidates is based on TOF information. Tracks may be accepted for both identification hypotheses. A track is used as a pion candidate *unless* it has a TOF measurement with good quality flag *and* the measured time is more than 5σ from that predicted for the π hypothesis. The analogous criterion is used to select kaon candidates, except for double tag modes in which both D_s decays contain photons, *i.e.* $D_s^+ \to \phi\pi^+\pi^0$ *vs.* $D_s^- \to \{\phi\pi^-\pi^0, \eta\pi^+, \text{or } \eta'\pi^+\}$. The high backgrounds in these channels are reduced by requiring kaons to have good quality TOF measurements with

$$\frac{|t_{\rm meas} - t_K|}{\sigma_K} \leq 5$$

and

$$\frac{t_{\rm meas} - t_\pi}{\sigma_\pi} + \frac{t_{\rm meas} - t_K}{\sigma_K} > 0.$$

All combinations of photons and accepted particle identification assignments are formed which have the π^+, π^-, K^+, K^-, and γ multiplicities of the desired final state. For each of these combinations a kinematic fit is performed which imposes total event energy and momentum conservation conditions (four constraints). The requirement $\chi^2 < 50$ is used to select combinations for further consideration. Since the detection efficiency for low energy photons is difficult to simulate in the Monte Carlo, the fitted photon energies are required to be greater than 50 MeV.

Within each successfully fitted track combination, candidates for $D_s^+ \to$ *Mode i* and $D_s^- \to$ *Mode j* decays are formed from all permutations of identical particles in the combination. The number of permutations is dramatically reduced by cuts on the resonant substructure of the D_s decay modes [Table 6.3]. The cuts on narrow resonances were chosen to be 95% efficient for Monte Carlo events. The resolutions

Table 6.3 Resonance mass cuts.

Mode	Resonance	Mass Interval (GeV/c^2) Center	Half-width	*vs. Mode*
$\phi\pi^+$	$\phi \to K^+K^-$	1.020	0.020	All
$\bar{K}^0K^+$	$K^0_S \to \pi^+\pi^-$	0.498	0.025	All
$f_0(975)\pi^+$	$f_0(975) \to \pi^+\pi^-$	0.965	0.040	All
$\bar{K}^{*0}K^+$	$\bar{K}^{*0} \to K^-\pi^+$	0.896	0.080	All
$\bar{K}^{*0}K^{*+}$	$\bar{K}^{*0} \to K^-\pi^+$	0.896	0.100	All
	$K^{*+} \to \bar{K}^0_S\pi^+$	0.892	0.100	All
	$K^0_S \to \pi^+\pi^-$	0.498	0.025	All
$\phi\pi^+\pi^+\pi^-$	$\phi \to K^+K^-$	1.020	0.020	All
$\phi\pi^+\pi^0$	$\phi \to K^+K^-$	1.020	0.020	All
	$\pi^0 \to \gamma\gamma$	0.135	0.030	$\phi\pi^+\pi^+\pi^-$ and $\bar{K}^{*0}K^{*+}$
		0.135	0.035	All others
$\eta\pi^+$	$\eta \to \gamma\gamma$	0.549	0.040	$\phi\pi^+\pi^+\pi^-$ and $\bar{K}^{*0}K^{*+}$
		0.549	0.070	$\phi\pi^+\pi^0$
		0.549	0.050	All others
	$\eta \to \pi^+\pi^-\pi^0$	0.549	0.050	$\phi\pi^+\pi^+\pi^-$ and $\bar{K}^{*0}K^{*+}$
		0.549	0.060	All others
	$\pi^0 \to \gamma\gamma$	0.135	0.035	$\phi\pi^+\pi^+\pi^-$ and $\bar{K}^{*0}K^{*+}$
		0.135	0.040	All others
$\eta'\pi^+$	$\eta' \to \gamma\rho^0$	0.958	0.045	$\phi\pi^+\pi^+\pi^-$ and $\bar{K}^{*0}K^{*+}$
		0.958	0.050	All others
	$\rho^0 \to \pi^+\pi^-$	0.700	0.200	All
	$\eta' \to \eta\pi^+\pi^-$	0.958	0.060	$\phi\pi^+\pi^+\pi^-$ and $\bar{K}^{*0}K^{*+}$
		0.958	0.065	All others
	$\eta \to \gamma\gamma$	0.549	0.060	$\phi\pi^+\pi^+\pi^-$ and $\bar{K}^{*0}K^{*+}$
		0.549	0.070	All others

for a particular D_s decay mode depend on the numbers of charged and neutral tracks in the decay of the other D_s in the event.

Further background rejection is achieved by imposing additional kinematic constraints on the candidate events. Two kinematic fits are attempted for each of the accepted track permutations. The two fit hypotheses are

$$e^+e^- \to D_s^{*+}X^-, \quad D_s^{*+} \to \gamma X^+,$$

and

$$e^+e^- \to D_s^{*-}X^+, \quad D_s^{*-} \to \gamma X^-,$$

where in each case $X^+ \to$ *Mode* i and $X^- \to$ *Mode* j. In other words, the two D_s candidates in the event are constrained to have equal but unspecified mass $M(X)$; this quantity is determined in the fit. The γ is also paired with the D_s candidates in both possible ways, requiring $M(\gamma X) = M(D_s^*) = 2.109\,\mathrm{GeV}/c^2$. Four-momentum conservation is again imposed, for a total of six constraints. The pairing which yields the larger $\mathrm{CL}(\chi^2_{6\mathrm{C}})$ is retained if $\mathrm{CL}(\chi^2_{6\mathrm{C}}) > 5\%$. Double tag events would produce a signal at the D_s^+ mass in the resulting $M(X)$ distribution.

In some D_s decay modes it is possible for a set of tracks to satisfy the resonance requirements in more than one way. For example, in $D_s^+ \to f_0(975)\pi^+ \to \pi^+\pi^+\pi^-$ both $\pi^+\pi^-$ combinations may satisfy the f_0 resonance cut, but in the double tag search the χ^2 and $M(X)$ values from the 6C fits would be identical. Only one entry to the $M(X)$ distribution is made in this case. However, an event may contribute multiple entries if $\gamma D_s^+ D_s^-$ candidates can be formed from different permutations of the tracks, for example, if spurious low-energy photon candidates are present.

A mass region is selected for each double tag mode which contains 95% of the Monte Carlo signal events, and the number of *distinct events* in the data which

Table 6.4 Half-width in GeV/c^2 of the $M(X)$ signal region for each double tag mode. Equal widths are used for the charge-conjugate final states. Each of the intervals is centered at 1.970 GeV/c^2.

	$\phi\pi^-$	K^0K^-	$f_0\pi^-$	$K^{*0}K^-$	$K^{*0}K^{*-}$	$\phi\pi^-\pi^-\pi^+$	$\phi\pi^-\pi^0$
$\phi\pi^+$	0.015						
$\bar{K}^0K^+$	0.010	0.010					
$f_0\pi^+$	0.015	0.015	0.010				
$\bar{K}^{*0}K^+$	0.010	0.015	0.015	0.015			
$\bar{K}^{*0}K^{*+}$	0.015	0.015	0.020	0.010	0.020		
$\phi\pi^+\pi^+\pi^-$	0.010	0.008	0.010	0.025	0.020	0.015	
$\phi\pi^+\pi^0$	0.025	0.020	0.030	0.020	0.030	0.030	0.025
$\eta\pi^+$							
$\eta \to \gamma\gamma$	0.025	0.025	0.025	0.025	0.025	0.025	0.030
$\eta \to 3\pi$	0.030	0.035	0.025	0.025	0.020	0.025	0.030
$\eta'\pi^+$							
$\eta' \to \gamma\rho^0$	0.020	0.020	0.020	0.015	0.015	0.020	0.030
$\eta' \to \eta\pi\pi$	0.030	0.025	0.025	0.020	0.025	0.020	0.035

populate this region is determined. For each group, the total number of candidate signal events, $n_{\rm obs}$, is determined by combining all double tag modes. The interval width for each of the double tag modes is listed in Table 6.4. The $M(X)$ distributions for all modes are shown below. The contribution from each event is weighted by $1/N$, where N is the number of entries (in all modes) from the event.

Group 1

The $M(X)$ distributions for the double tag modes of Group 1 are shown in Figs. 6.1 to 6.7. The limits of the signal regions are indicated. The sum of these histograms is found in Fig. 6.8(a); the unweighted sum is shown in Fig. 6.8(b). Table 6.5 contains the event and entry totals for each mode. No candidate events are found in the signal regions.

Group 2

The $M(X)$ distributions for the double tag modes of Group 2, weighted by $1/N$, are shown in Figs. 6.9 and 6.10. The sum of these histograms is found in Fig. 6.11(a); the unweighted sum is shown in Fig. 6.11(b). Table 6.6 contains the event and entry totals for each mode. The total number of candidate events found in the signal regions is $n_{\rm obs} = 5$.

Group 3

The $M(X)$ distributions for the double tag modes of Group 3, weighted by $1/N$, are shown in Figs. 6.12 and 6.13. The sum of these histograms is found in Fig. 6.14(a); the unweighted sum is shown in Fig. 6.14(b). Table 6.7 contains the event and entry totals for each mode. The total number of candidate events found in the signal regions is $n_{\rm obs} = 3$.

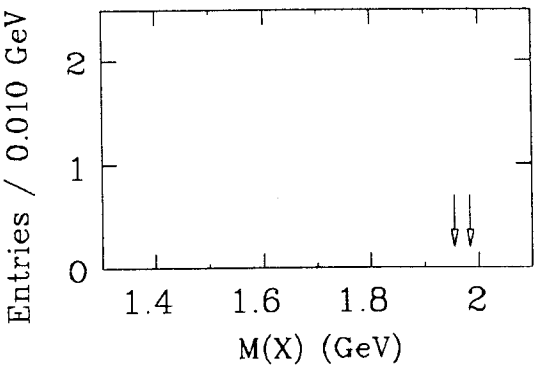

Figure 6.1 $M(X)$ distributions from Group 1 double tag modes, with entries weighted by $1/N$: $\phi\pi^+$ *vs.* $\phi\pi^-$. The limits of the signal region are indicated by the arrows.

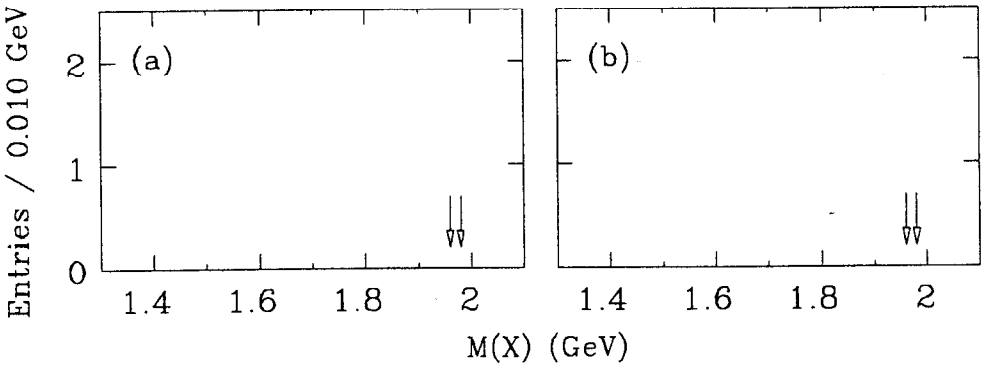

Figure 6.2 Group 1 weighted $M(X)$ distributions (continued): $\bar{K}^0K^+$ *vs.* (a) $\phi\pi^-$, (b) K^0K^-.

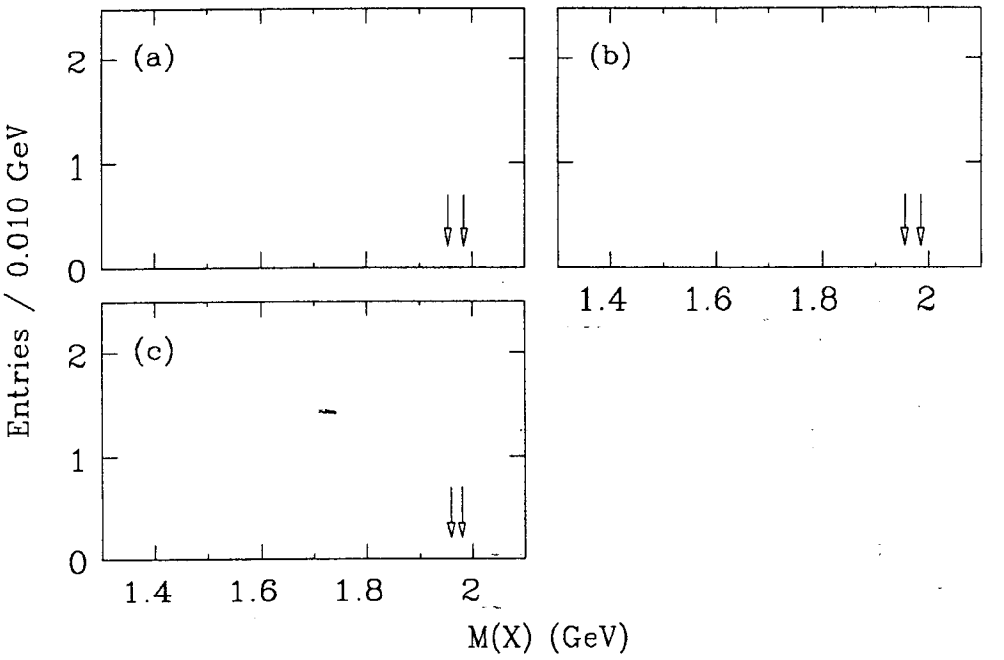

Figure 6.3 Group 1 weighted $M(X)$ distributions (continued): $f_0(975)\pi^+$ *vs.* (a) $\phi\pi^-$, (b) K^0K^-, (c) $f_0(975)\pi^-$.

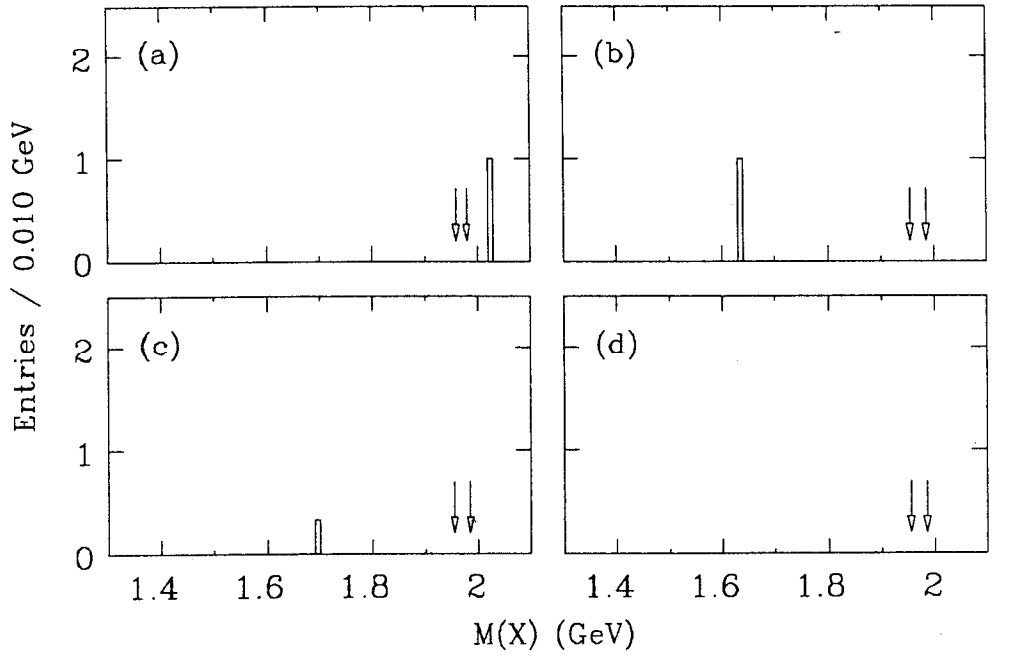

Figure 6.4 Group 1 weighted $M(X)$ distributions (continued): $\bar{K}^{*0}K^+$ *vs.* (a) $\phi\pi^-$, (b) K^0K^-, (c) $f_0(975)\pi^-$, (d) $K^{*0}K^-$.

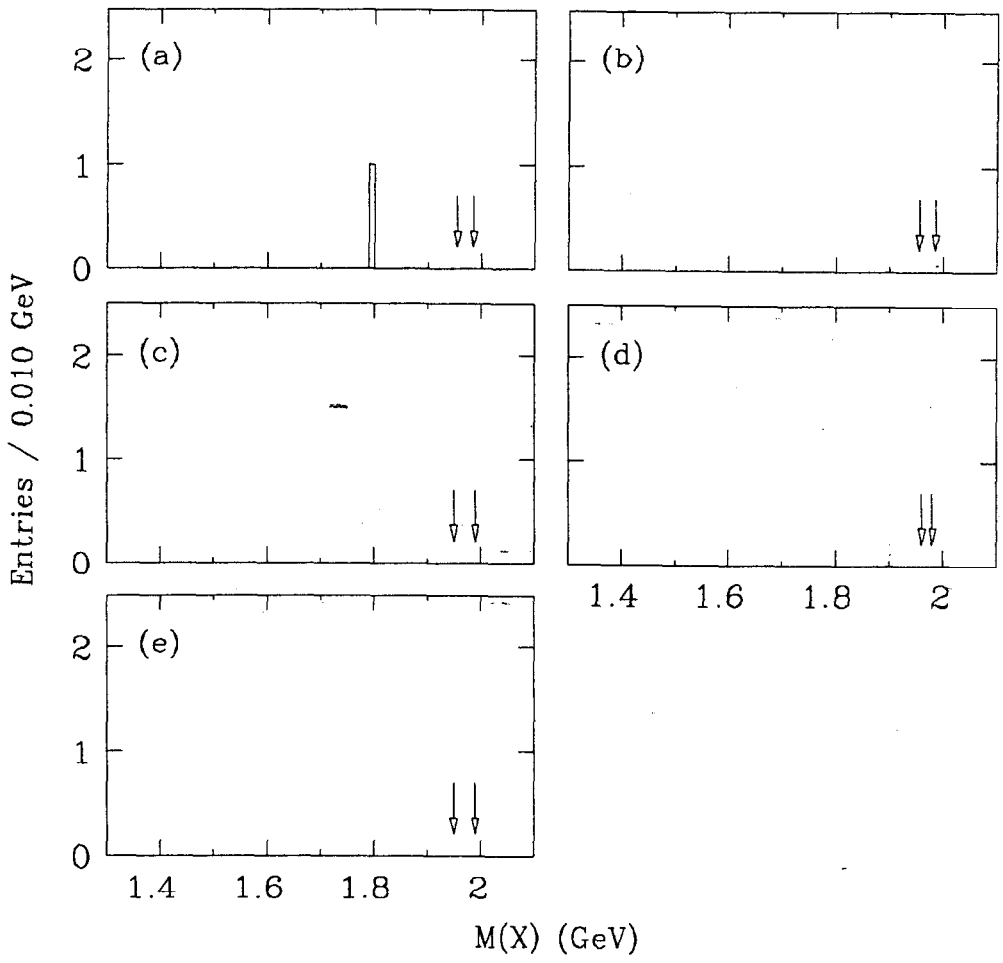

Figure 6.5 Group 1 weighted $M(X)$ distributions (continued): $\bar{K}^{*0}K^{*+}$ *vs.* (a) $\phi\pi^-$, (b) K^0K^-, (c) $f_0(975)\pi^-$, (d) $K^{*0}K^-$, (e) $K^{*0}K^{*-}$.

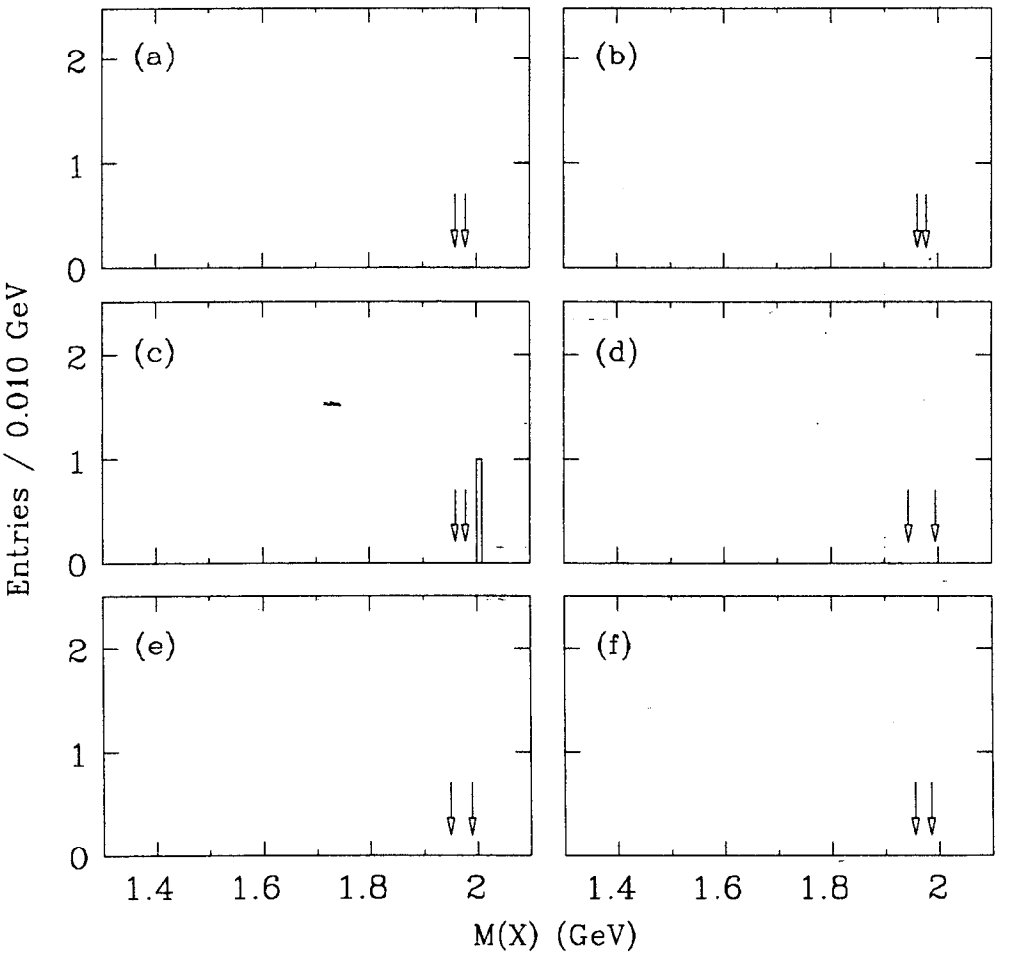

Figure 6.6 Group 1 weighted $M(X)$ distributions (continued): $\phi\pi^+\pi^+\pi^-$ *vs.* (a) $\phi\pi^-$, (b) K^0K^-, (c) $f_0(975)\pi^-$, (d) $K^{*0}K^-$, (e) $K^{*0}K^{*-}$, (f) $\phi\pi^-\pi^-\pi^+$.

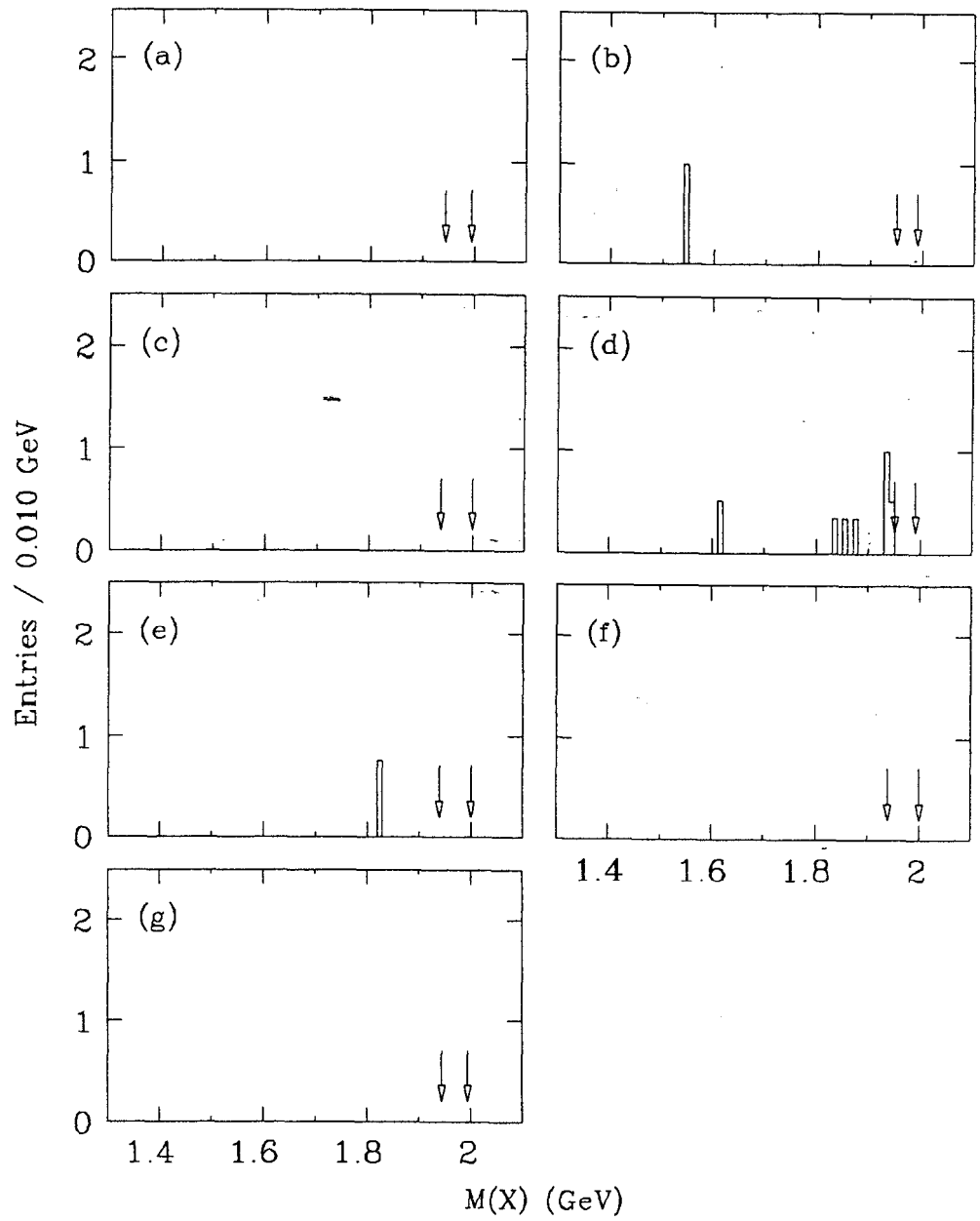

Figure 6.7 Group 1 weighted $M(X)$ distributions (continued): $\phi\pi^+\pi^0$ *vs.* (a) $\phi\pi^-$, (b) K^0K^-, (c) $f_0(975)\pi^-$, (d) $K^{*0}K^-$, (e) $K^{*0}K^{*-}$, (f) $\phi\pi^-\pi^-\pi^+$, (g) $\phi\pi^-\pi^0$.

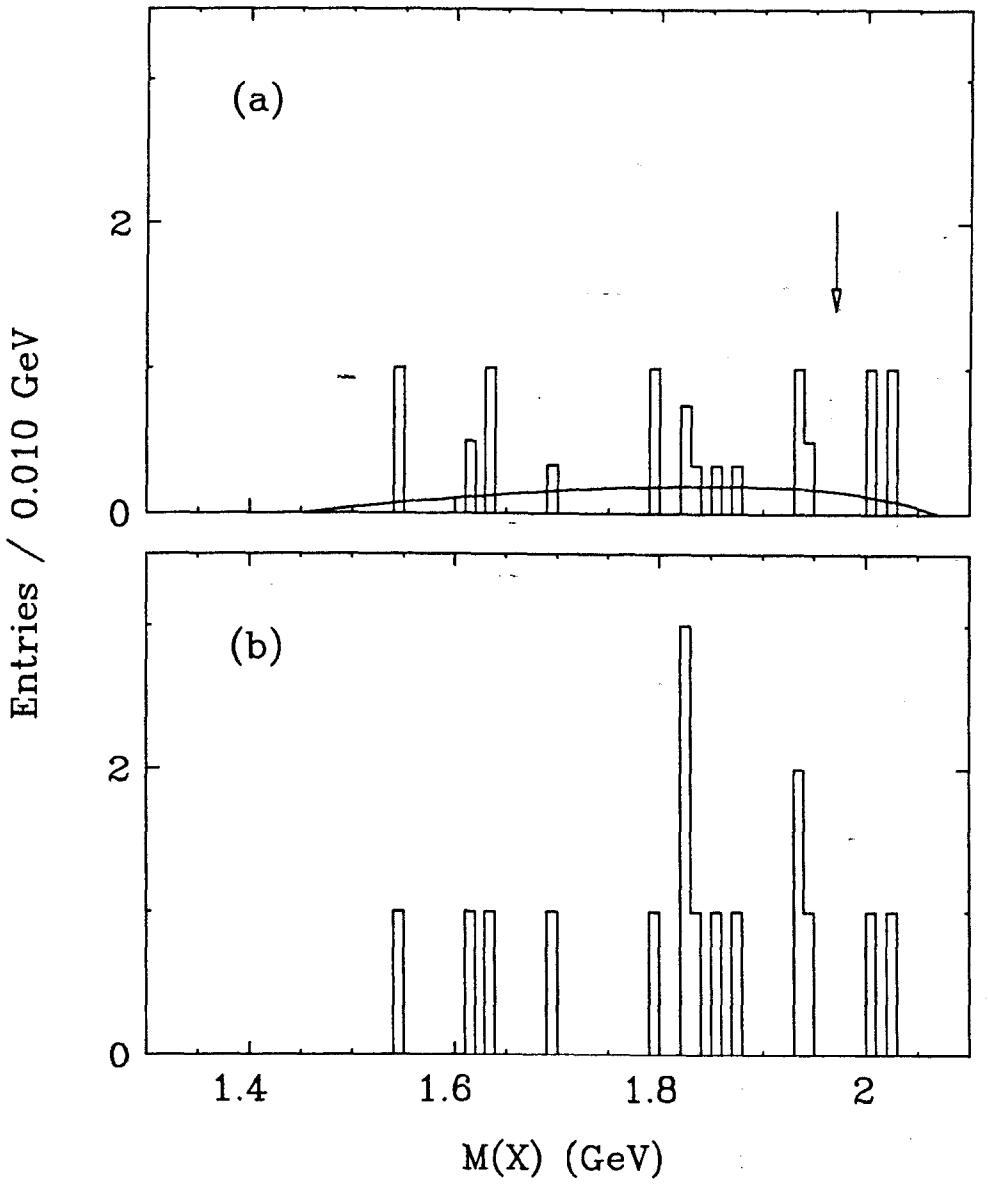

Figure 6.8 Sum of $M(X)$ distributions from Group 1 double tag modes, (a) entries weighted by $1/N$, (b) unweighted. The curve in (a) is the result of a fit to the spectrum outside of the region 1.935–2.005 GeV/c^2. The arrow is drawn at the D_s^+ mass.

Table 6.5 Statistics from Group 1 double tag modes. Tabulated are the number of entries and the number of distinct events contributing to the signal region and to the entire mass spectrum for *Mode i vs. Mode j* + charge conjugate.

		Signal Region		Total	
Mode i	*Mode j*	Events	Entries	Events	Entries
$\phi\pi^+$	$\phi\pi^-$	0	0	0	0
$\bar{K}^0K^+$	$\phi\pi^-$	0	0	0	0
	K^0K^-	0	0	0	0
$f_0(975)\pi^+$	$\phi\pi^-$	0	0	0	0
	K^0K^-	0	0	0	0
	$f_0(975)\pi^-$	0	0	0	0
$\bar{K}^{*0}K^+$	$\phi\pi^-$	0	0	1	1
	K^0K^-	0	0	1	1
	$f_0(975)\pi^-$	0	0	1	1
	$K^{*0}K^-$	0	0	0	0
$\bar{K}^{*0}K^{*+}$	$\phi\pi^-$	0	0	1	1
	K^0K^-	0	0	0	0
	$f_0(975)\pi^-$	0	0	0	0
	$K^{*0}K^-$	0	0	0	0
	$K^{*0}K^{*-}$	0	0	0	0
$\phi\pi^+\pi^+\pi^-$	$\phi\pi^-$	0	0	0	0
	K^0K^-	0	0	0	0
	$f_0(975)\pi^-$	0	0	1	1
	$K^{*0}K^-$	0	0	0	0
	$K^{*0}K^{*-}$	0	0	0	0
	$\phi\pi^-\pi^-\pi^+$	0	0	0	0
$\phi\pi^+\pi^0$	$\phi\pi^-$	0	0	0	0
	K^0K^-	0	0	1	1
	$f_0(975)\pi^-$	0	0	0	0
	$K^{*0}K^-$	0	0	4	7
	$K^{*0}K^{*-}$	0	0	1	3
	$\phi\pi^-\pi^-\pi^+$	0	0	0	0
	$\phi\pi^-\pi^0$	0	0	0	0
Total		0	0	11	16

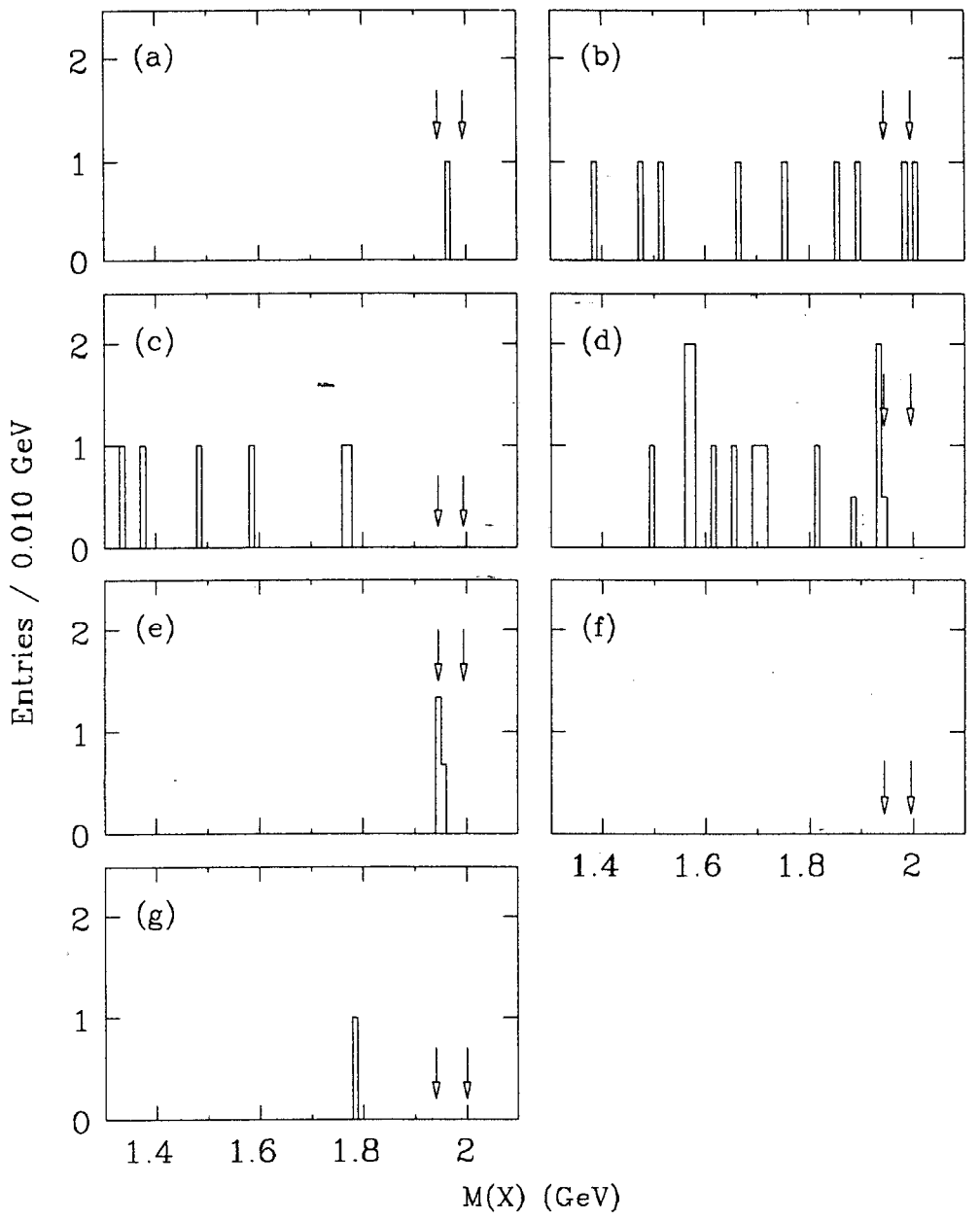

Figure 6.9 $M(X)$ distributions from Group 2 double tag modes, with entries weighted by $1/N$: $\eta\pi^+$, $\eta \to \gamma\gamma$ *vs.* (a) $\phi\pi^-$, (b) K^0K^-, (c) $f_0(975)\pi^-$, (d) $K^{*0}K^-$, (e) $K^{*0}K^{*-}$, (f) $\phi\pi^-\pi^-\pi^+$, (g) $\phi\pi^-\pi^0$. The limits of the signal regions are indicated by the arrows.

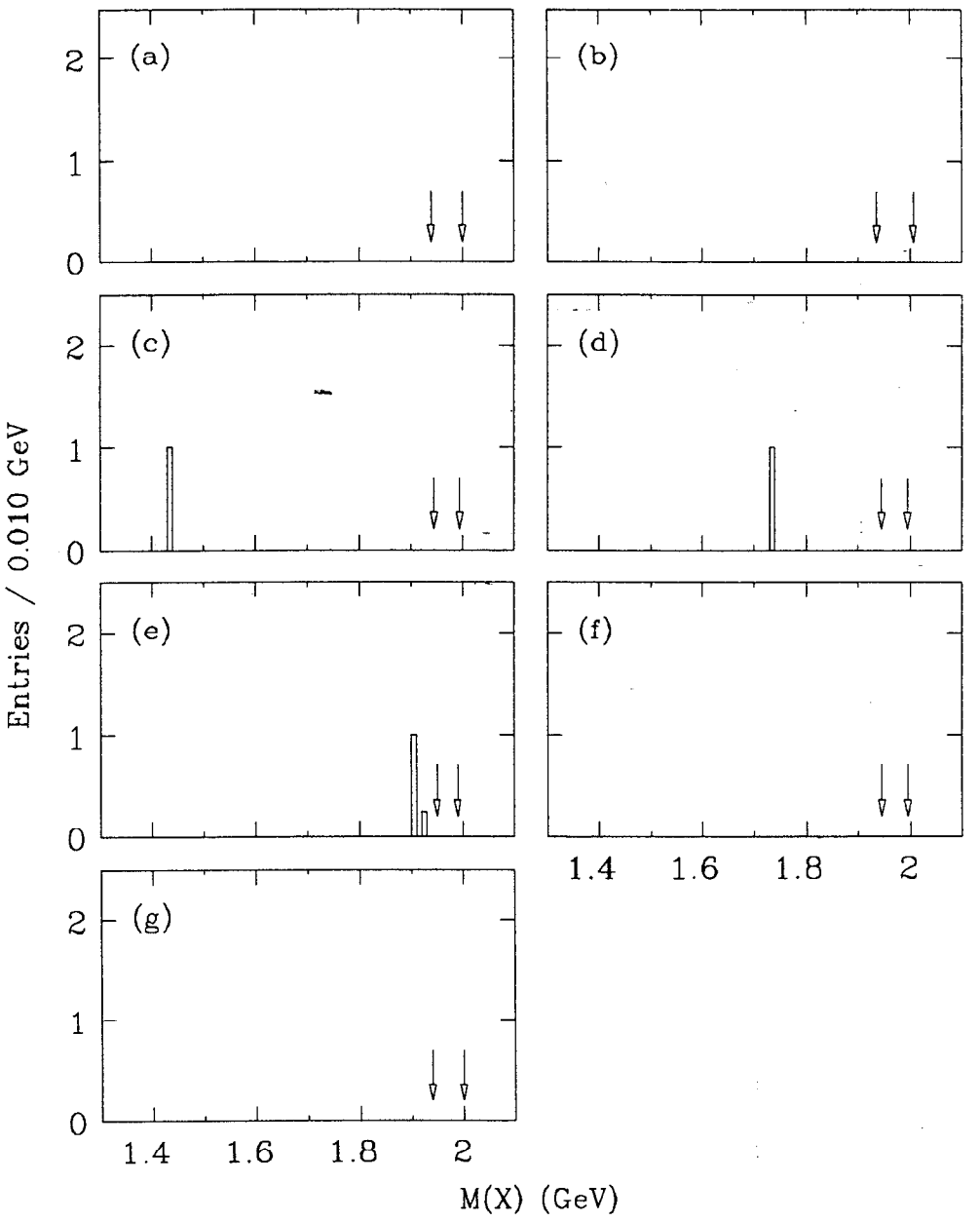

Figure 6.10 Group 2 weighted $M(X)$ distributions (continued): $\eta\pi^+$, $\eta \to \pi^+\pi^-\pi^0$ *vs.* (a) $\phi\pi^-$, (b) K^0K^-, (c) $f_0(975)\pi^-$, (d) $K^{*0}K^-$, (e) $K^{*0}K^{*-}$, (f) $\phi\pi^-\pi^-\pi^+$, (g) $\phi\pi^-\pi^0$.

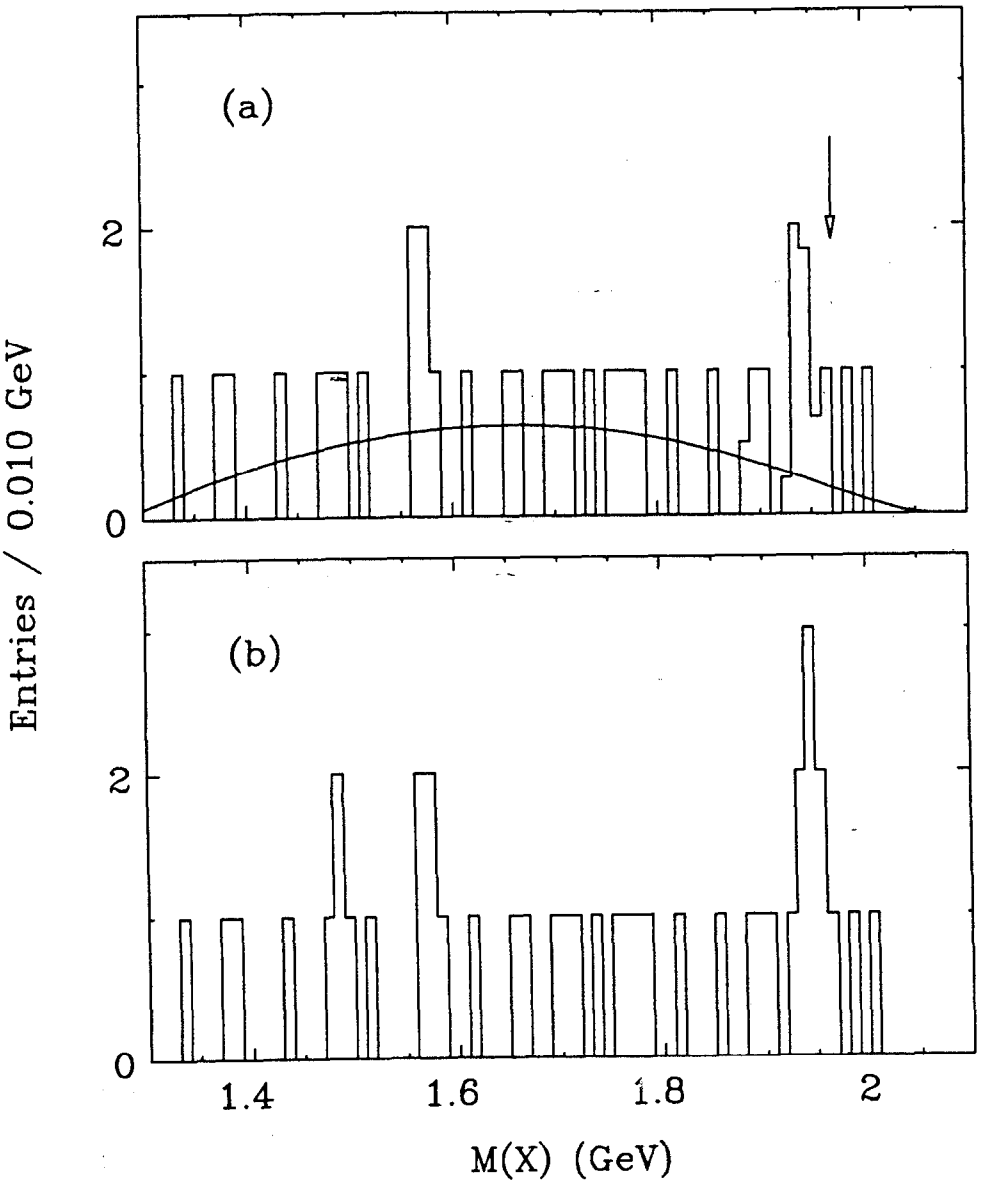

Figure 6.11 Sum of $M(X)$ distributions from Group 2 double tag modes, (a) entries weighted by $1/N$, (b) unweighted. The curve in (a) is the result of a fit to the spectrum outside of the region 1.935–2.005 GeV/c^2.

Table 6.6 Statistics from Group 2 double tag modes.

		Signal Region		Total	
Mode i	*Mode j*	Events	Entries	Events	Entries
$\eta\pi^+$, $\eta \to \gamma\gamma$	$\phi\pi^-$	1	1	1	1
	K^0K^-	1	1	9	9
	$f_0(975)\pi^-$	0	0	7	8
	$K^{*0}K^-$	1	1	14	15
	$K^{*0}K^{*-}$	2	4	2	4
	$\phi\pi^-\pi^-\pi^+$	0	0	0	0
	$\phi\pi^-\pi^0$	0	0	1	1
$\eta\pi^+$, $\eta \to 3\pi$	$\phi\pi^-$	0	0	0	0
	K^0K^-	0	0	0	0
	$f_0(975)\pi^-$	0	0	1	1
	$K^{*0}K^-$	0	0	1	1
	$K^{*0}K^{*-}$	0	0	2	2
	$\phi\pi^-\pi^-\pi^+$	0	0	0	0
	$\phi\pi^-\pi^0$	0	0	1	1
Total		5	7	38	42

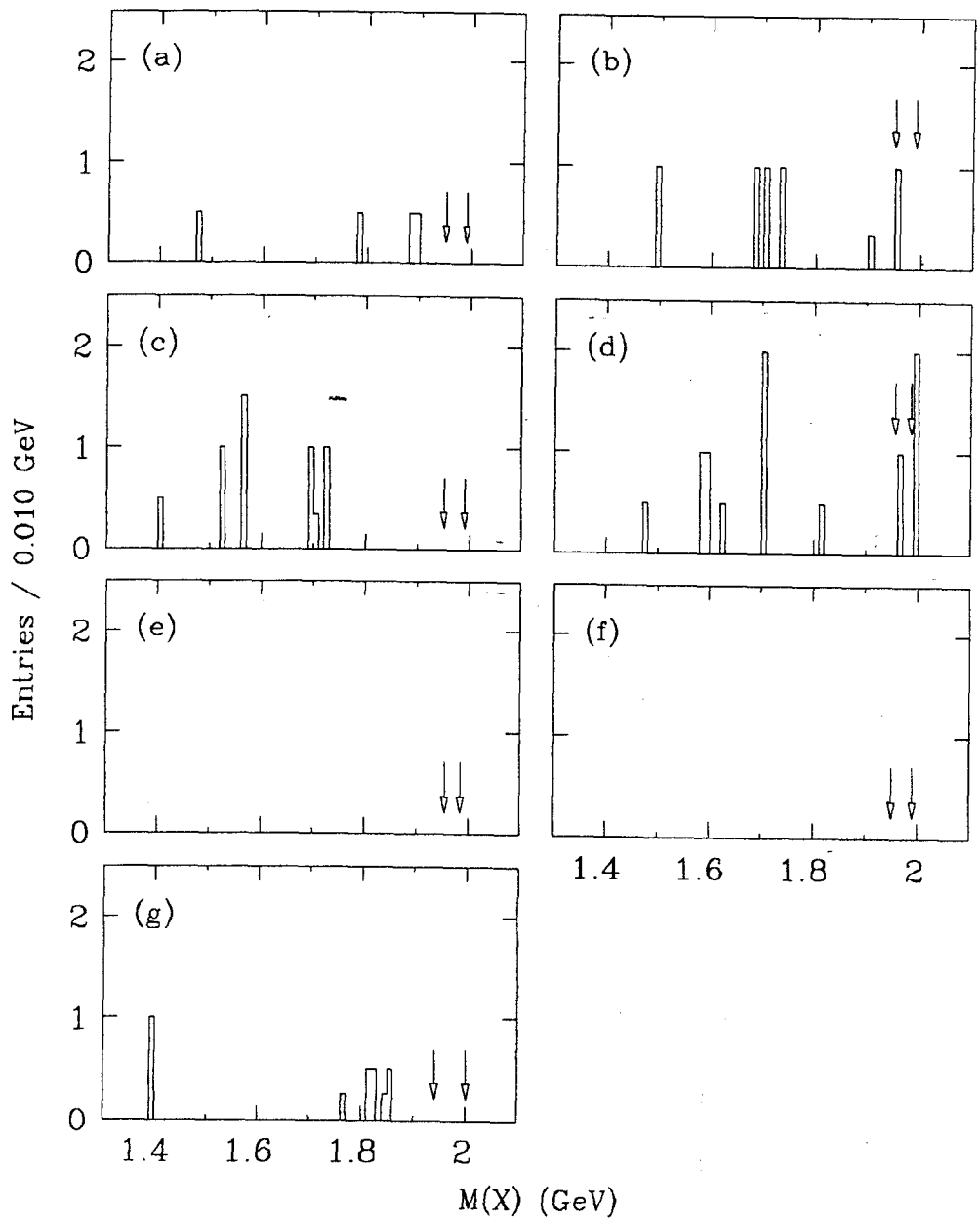

Figure 6.12 $M(X)$ distributions from Group 3 double tag modes, with entries weighted by $1/N$: $\eta'\pi^+$, $\eta' \to \gamma\rho^0$ *vs.* (a) $\phi\pi^-$, (b) K^0K^-, (c) $f_0(975)\pi^-$, (d) $K^{*0}K^-$, (e) $K^{*0}K^{*-}$, (f) $\phi\pi^-\pi^-\pi^+$, (g) $\phi\pi^-\pi^0$. The limits of the signal regions are indicated by the arrows.

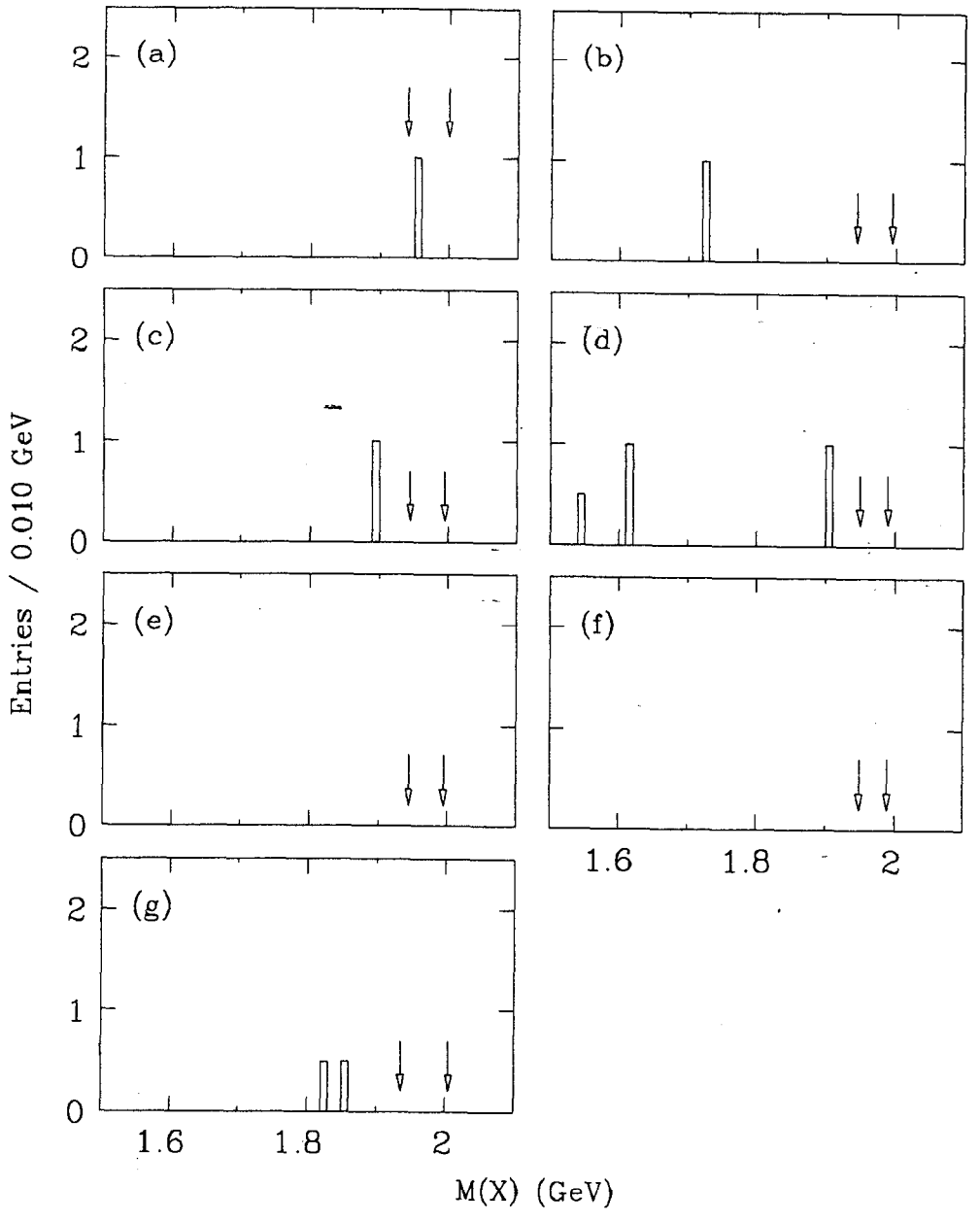

Figure 6.13 Group 3 weighted $M(X)$ distributions (continued): $\eta'\pi^+$, $\eta' \to \eta\pi^+\pi^-$, $\eta \to \gamma\gamma$ *vs.* (a) $\phi\pi^-$, (b) K^0K^-, (c) $f_0(975)\pi^-$, (d) $K^{*0}K^-$, (e) $K^{*0}K^{*-}$, (f) $\phi\pi^-\pi^-\pi^+$, (g) $\phi\pi^-\pi^0$.

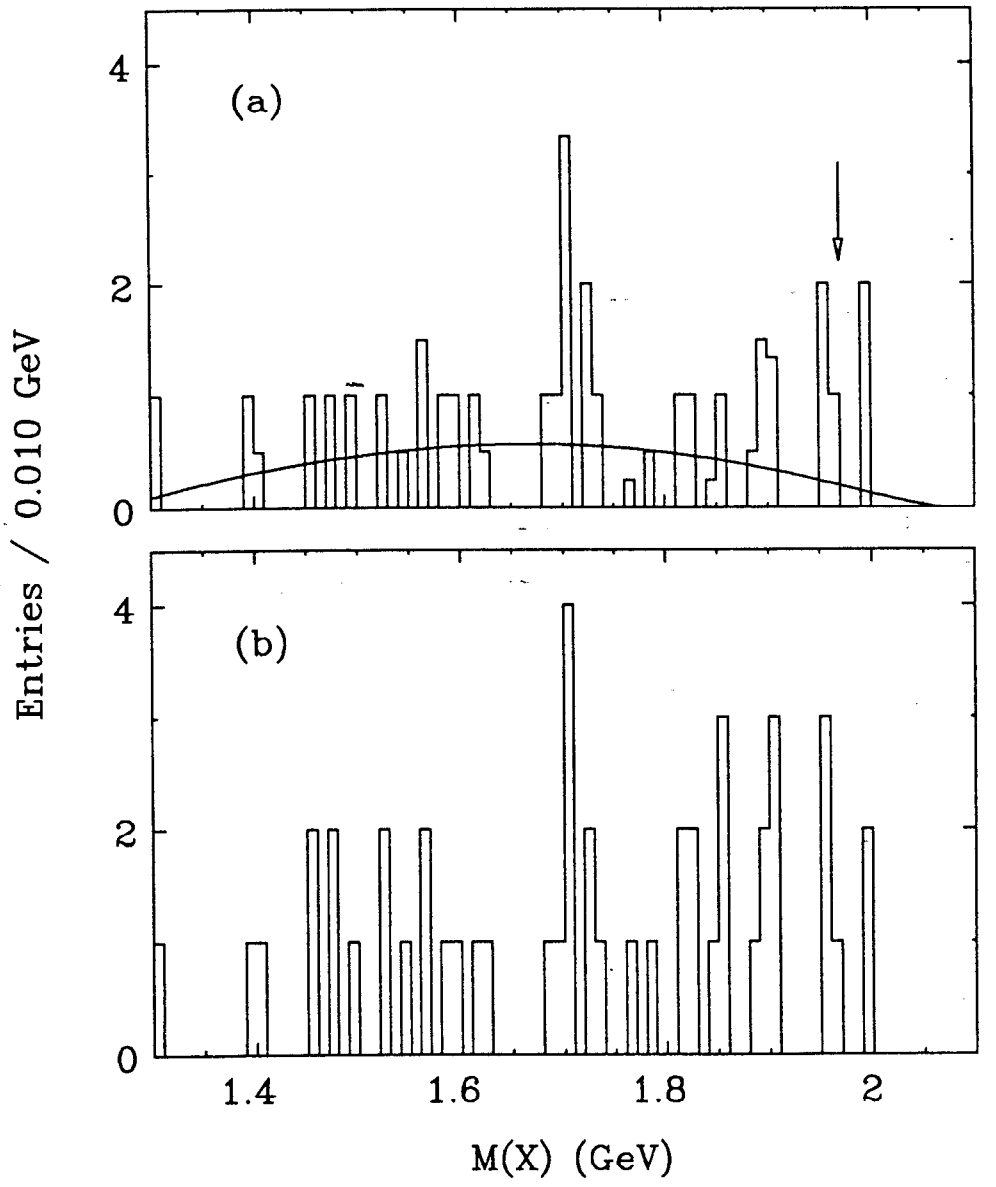

Figure 6.14 Sum of $M(X)$ distributions from Group 3 double tag modes, (a) entries weighted by $1/N$, (b) unweighted. The curve in (a) is the result of a fit to the spectrum outside of the region 1.935–2.005 GeV/c^2.

Table 6.7 Statistics from Group 3 double tag modes.

		Signal Region		Total	
Mode i	*Mode j*	Events	Entries	Events	Entries
$\eta'\pi^+$, $\eta' \to \gamma\rho^0$	$\phi\pi^-$	0	0	3	4
	K^0K^-	1	2	5	6
	$f_0(975)\pi^-$	0	0	6	8
	$K^{*0}K^-$	1	1	9	10
	$K^{*0}K^{*-}$	0	0	0	0
	$\phi\pi^-\pi^-\pi^+$	0	0	0	0
	$\phi\pi^-\pi^0$	0	0	3	7
$\eta'\pi^-$, $\eta' \to \eta\pi\pi$	$\phi\pi^-$	1	1	2	2
	K^0K^-	0	0	2	2
	$f_0(975)\pi^-$	0	0	1	1
	$K^{*0}K^-$	0	0	4	5
	$K^{*0}K^{*-}$	0	0	0	0
	$\phi\pi^-\pi^-\pi^+$	0	0	0	0
	$\phi\pi^-\pi^0$	0	0	1	2
Total		3	4	35	49

D^0 Double Tags

As a check of the procedure, a search is made for D^0 double tags from the reaction

$$e^+e^- \to D^{*0}\bar{D}^0 \text{ or } \bar{D}^{*0}D^0,$$

$$D^* \to \gamma D.$$

The following double tag modes are considered:

- $K^-\pi^+\pi^+\pi^-$ *vs.* $K^\pm\pi^-\pi^-\pi^+$,
- $K^-\pi^+\pi^+\pi^-$ *vs.* $K^+\pi^-\pi^0$ + *c.c.*,
- $K^-\pi^+\pi^0$ *vs.* $K^+\pi^-\pi^0$.

The γD mass constraint is changed to $M(D^{*0}) = 2.007\,\mathrm{GeV}/c^2$. To reduce the combinatoric background, kaon candidates are required to satisfy the more stringent TOF requirement used for $D_s^+ \to \phi\pi^+\pi^0$. The $\gamma\gamma$ mass cut for selecting π^0's after the four-constraint fit is 0.10 to $0.17\,\mathrm{GeV}/c^2$. No other resonance cuts are made.

The sum of the observed $M(X)$ distributions, weighted by $1/N$, appears in Fig. 6.15(a). This spectrum contains more entries in the D region than predicted from a simulation of $D\bar{D}$, $D^*\bar{D}$, and $D^*\bar{D}^*$ events [Figure 6.15(b)]. This is an indication that spurious photon candidates can artificially enhance the reconstruction efficiency, and/or that events with only one correctly reconstructed D can be pulled into the signal region by the 6C kinematic fit. This situation is tolerable when setting upper limits on double tag signals, but attempts to measure $B_{\eta\pi^+}$ and $B_{\eta'\pi^+}$ from the small enhancements in Groups 2 and 3 would not be reliable. For this reason, no such measurements will be quoted.

It is interesting to note that about 35% of the Monte Carlo double tag events populating the D^0 region are correctly identified, 25% have both D's correctly reconstructed but $D^{*0} \to \pi^0 D^0$ instead of γD^0, and 40% have some other topology

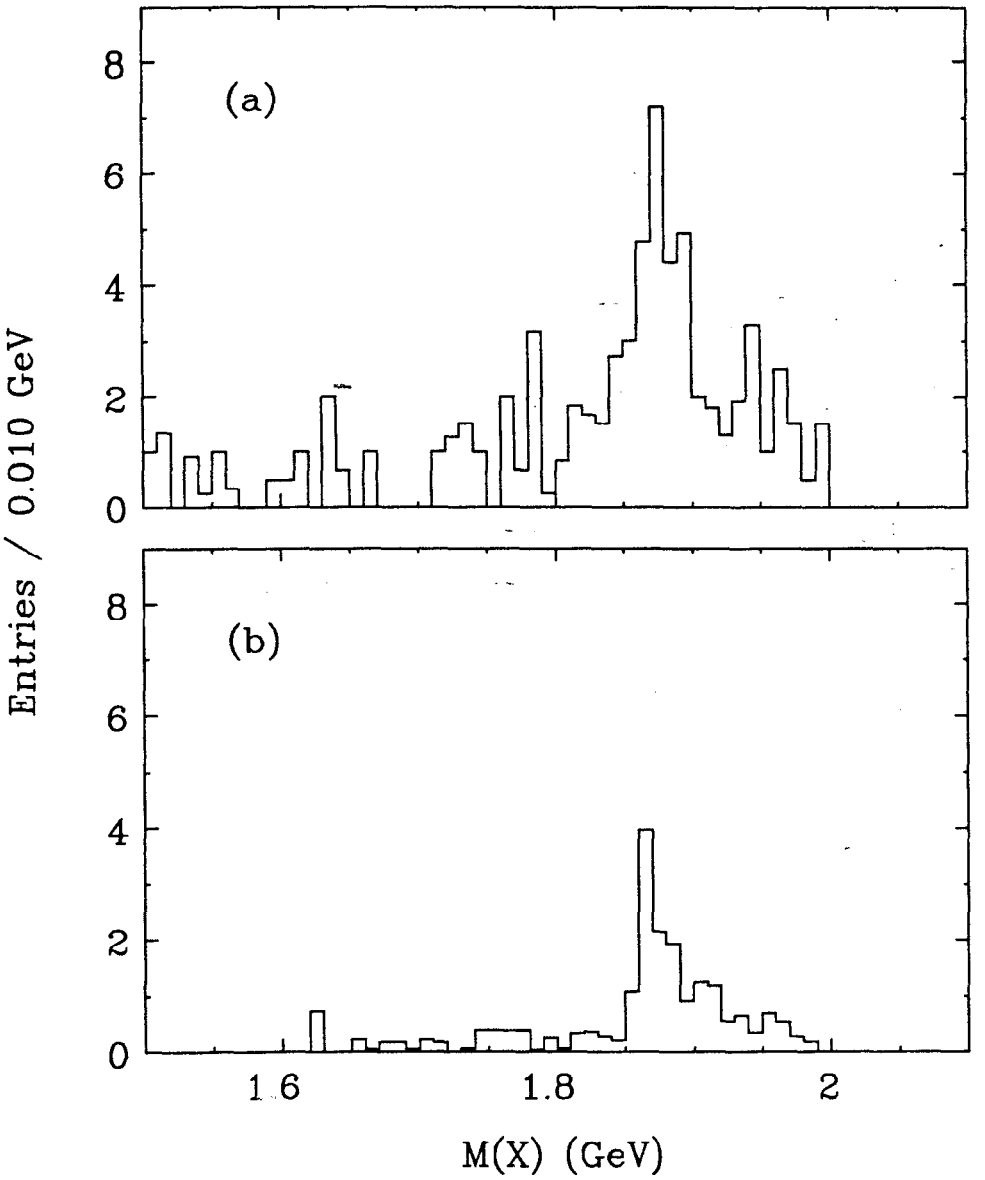

Figure 6.15 Sum of weighted $M(X)$ distributions for D^0 double tag modes: (a) data, (b) Monte Carlo $D\bar{D}$, $D^*\bar{D}$, and $D^*\bar{D}^*$ events, normalized to the same integrated luminosity.

such as $K^-\pi^+\pi^0$ *vs.* $K^+\pi^-\pi^0\pi^0$, or $e^+e^- \to D^*\bar{D}^*$. Most of the misidentified events arise in the $K^-\pi^+\pi^0$ *vs.* $K^+\pi^-\pi^0$ mode.

6.3 Calculation of Upper Limits on Absolute Branching Fractions

Upper limits on $B_{\phi\pi^+}$, $B_{\eta\pi^+}$, and $B_{\eta'\pi^+}$ are established from the three groups of double tag modes by computing the relative likelihood of observing $n_{\rm obs}$ candidate events in a group as a function of the corresponding B_i. For each group this likelihood function is integrated over B_i to find the 90% CL point.

The likelihood functions are described in the following notation:

$$\begin{aligned}
\nu_{\rm s},\, \nu_{\rm b} &= \text{ expected total number of signal and background events,} \\
A &\equiv \sigma(e^+e^- \to D_s^{*\pm}D_s^{\mp})\mathcal{L}B_{\phi\pi^+}, \\
b_i &\equiv B_i/B_{\phi\pi^+}, \\
\epsilon_{ij} &= \text{ detection efficiency for double tag mode } i \textit{ vs. } j;
\end{aligned}$$

the index $i = 1, 2, \ldots, 7$ refers to the D_s^+ decay modes $\phi\pi^+$, $\bar{K}^0K^+$, $f_0(975)\pi^+$, $\bar{K}^{*0}K^+$, $\bar{K}^{*0}K^{*+}$, $\phi\pi^+\pi^+\pi^-$, $\phi\pi^+\pi^0$. Also let

$$\mathbf{u} \equiv \begin{bmatrix} A \\ b_2 \\ b_3 \\ \vdots \\ b_7 \end{bmatrix}.$$

The measured values $\hat{u}_i$ are assumed to have Gaussian errors, with S_{ij} = covariance of the measurements $\hat{u}_i$ and $\hat{u}_j$. The $\hat{u}_i$ and their errors $(=\sqrt{S_{ii}})$ are listed in Table 6.8. Because the absolute branching fraction results are inversely proportional to $A = \sigma\mathcal{L}B(D_s^+ \to \phi\pi^+)$, it is desirable to measure this quantity with high precision. The Mark III measurement of $\sigma B(D_s^+ \to \bar{K}^{*0}K^+)$ (Chapter 5) and the world average value of $B_{\bar{K}^{*0}K^+}/B_{\phi\pi^+}$ are used to obtain $A = 146 \pm 57$. Combining this with the Mark III direct measurement of $A = 162 \pm 51$ (Chapter 4) and accounting for

Table 6.8 Measured values of $\sigma\mathcal{L}B_{\phi\pi^+}$ and relative branching fractions. The off-diagonal elements of **S** are zero, except $S_{12} = S_{21} = -8.63$ and $S_{14} = S_{41} = -0.83$.

i	$u_i \equiv$	$\hat{u}_i$	$\sqrt{S_{ii}}$	References
1	$A = \sigma(e^+e^- \to D_s^{*\pm}D_s^{\mp})\mathcal{L}B(D_s^+ \to \phi\pi^+)$	156	38	(See text)
2	$b_2 = B(D_s^+ \to \bar{K}^0K^+)/B(D_s^+ \to \phi\pi^+)$	0.92	0.38	71
3	$b_3 = B(D_s^+ \to f_0(975)\pi^+)/B(D_s^+ \to \phi\pi^+)$	0.28	0.10	23
4	$b_4 = B(D_s^+ \to \bar{K}^{*0}K^+)/B(D_s^+ \to \phi\pi^+)$	0.93	0.12	62, 65, 57, 58
5	$b_5 = B(D_s^+ \to \bar{K}^{*0}K^{*+})/B(D_s^+ \to \phi\pi^+)$	2.3	1.4	57
6	$b_6 = B(D_s^+ \to \phi\pi^+\pi^+\pi^-)/B(D_s^+ \to \phi\pi^+)$	0.41	0.10	69, 65, 57
7	$b_7 = B(D_s^+ \to \phi\pi^+\pi^0)/B(D_s^+ \to \phi\pi^+)$	2.4	1.1	25

common systematic errors yields $A = 156 \pm 38$. The uncertainty on the integrated luminosity cancels entirely in this analysis.

The total number of background events in the signal regions of each group is estimated by summing the $M(X)$ histograms, weighted by $1/N$. A smooth curve is fitted to the resulting distribution, omitting the interval $1.935 \leq M(X) \leq 2.005\,\mathrm{GeV}/c^2$, which corresponds to the widest signal regions. This curve is used to represent the background shape in each of the double tag modes. The expected number of background events in the signal region of a particular mode is obtained by normalizing the background curve to the sum of the entry weights outside of the signal region, and integrating the curve inside the region. The sum of these background predictions, denoted ν_b, is a conservative estimate of the number of distinct background events expected to contribute to n_{obs}.

The ϵ_{ij} are obtained from Monte Carlo samples of the double tag modes [Tables 6.9–6.11]. At most one entry per simulated event is counted in the determination. The branching fractions for $\phi \to K^+K^-$, $\bar{K}^0 \to \pi^+\pi^-$, etc.

have been factored into the ϵ_{ij}.

The expected number of reconstructed double tag events in Group 1 is

$$\begin{aligned}\nu_s = \nu_s(\mathbf{u}, B_{\phi\pi^+}) &= \sigma\mathcal{L}\sum_{i,j=1}^{7} B_i B_j \epsilon_{ij} \\ &= [\sigma\mathcal{L}B_{\phi\pi^+}]B_{\phi\pi^+}\sum b_i b_j \epsilon_{ij} \\ &= AB_{\phi\pi^+}\sum b_i b_j \epsilon_{ij} \qquad \text{(Group 1)}.\end{aligned}$$

The relative likelihood $\ell(B_{\phi\pi^+})$ is computed by maximizing the function

$$\ell(\mathbf{u}, B_{\phi\pi^+}) = \frac{1}{n_{\rm obs}!}(\nu_s + \nu_b)^{n_{\rm obs}} \exp\left[-\nu_s - \nu_b - \tfrac{1}{2}(\mathbf{u}-\hat{\mathbf{u}})^t \mathbf{S}^{-1}(\mathbf{u}-\hat{\mathbf{u}})\right]$$

with respect to $\mathbf{u}$. The likelihood is set to zero for values of $B_{\phi\pi^+}$ and $\mathbf{u}$ which yield $B_{\phi\pi^+}\Sigma b_i > 100\%$. The 90% CL upper limit B_{90} on the value of $B_{\phi\pi^+}$ is obtained numerically from

$$\frac{\int_0^{B_{90}} \ell(B)\,dB}{\int_0^1 \ell(B)\,dB} = 0.90\,.$$

In Groups 2 and 3 the expected numbers of signal events are

$$\begin{aligned}\nu_s(\mathbf{u}, B_{\eta\pi^+}) &= 2\sigma\mathcal{L}\sum_{i=1}^{7} B_{\eta\pi^+} B_i \epsilon_{\eta i} \\ &= 2[\sigma\mathcal{L}B_{\phi\pi^+}]B_{\eta\pi^+}\sum b_i \epsilon_{\eta i} \\ &= 2AB_{\eta\pi^+}\sum b_i \epsilon_{\eta i} \qquad \text{(Group 2)}, \\ \nu_s(\mathbf{u}, B_{\eta'\pi^+}) &= 2AB_{\eta'\pi^+}\sum b_i \epsilon_{\eta' i} \qquad \text{(Group 3)},\end{aligned}$$

where $\epsilon_{\eta i}$ is the total detection efficiency for $D_s^+ \to \eta\pi^+$, $\eta \to \gamma\gamma$ and $\eta \to \pi^+\pi^-\pi^0$ *vs.* mode i, and where $\epsilon_{\eta' i}$ is the total for $D_s^+ \to \eta'\pi^+$, $\eta' \to \gamma\rho^0$ and $\eta' \to \eta\pi^+\pi^-$, $\eta \to \gamma\gamma$ *vs.* mode i. The upper limits on $B_{\eta\pi^+}$ and $B_{\eta'\pi^+}$ are established using the same $\ell(\mathbf{u}, B)$ as in Group 1, but without the "unitarity" condition.

The following contributions to the systematic uncertainty are considered:

Table 6.9 Detection efficiencies for Group 1 double tag modes. $N_{ij}^{\rm mc}$ is the number of reconstructed Monte Carlo events contributing to the signal region for mode i *vs.* j; this is used to obtain the Monte Carlo statistical error.

Mode i	*Mode j*	ϵ_{ij}	$N_{ij}^{\rm mc}$
$\phi\pi^+$	$\phi\pi^-$	0.0191	234
$\bar{K}^0K^+$	$\phi\pi^-$	0.0175	618
	K^0K^-	0.0190	485
$f_0(975)\pi^+$	$\phi\pi^-$	0.0285	332
	K^0K^-	0.0298	501
	$f_0(975)\pi^-$	0.0367	407
$\bar{K}^{*0}K^+$	$\phi\pi^-$	0.0224	204
	K^0K^-	0.0236	618
	$f_0(975)\pi^-$	0.0331	286
	$K^{*0}K^-$	0.0337	227
$\bar{K}^{*0}K^{*+}$	$\phi\pi^-$	0.0030	111
	K^0K^-	0.0032	166
	$f_0(975)\pi^-$	0.0053	184
	$K^{*0}K^-$	0.0042	114
	$K^{*0}K^{*-}$	0.0007	55
$\phi\pi^+\pi^+\pi^-$	$\phi\pi^-$	0.0043	53
	K^0K^-	0.0037	65
	$f_0(975)\pi^-$	0.0068	79
	$K^{*0}K^-$	0.0060	55
	$K^{*0}K^{*-}$	0.0008	29
	$\phi\pi^-\pi^-\pi^+$	0.0010	17
$\phi\pi^+\pi^0$	$\phi\pi^-$	0.0095	116
	K^0K^-	0.0075	133
	$f_0(975)\pi^-$	0.0122	142
	$K^{*0}K^-$	0.0113	103
	$K^{*0}K^{*-}$	0.0015	55
	$\phi\pi^-\pi^-\pi^+$	0.0023	57
	$\phi\pi^-\pi^0$	0.0010	16

Table 6.10 Detection efficiencies for Group 2 double tag modes.

Mode i	*Mode j*	ϵ_{ij}	$N_{ij}^{\rm mc}$
$\eta\pi^+$, $\eta \to \gamma\gamma$	$\phi\pi^-$	0.0333	519
	K^0K^-	0.0342	769
	$f_0(975)\pi^-$	0.0483	717
	$K^{*0}K^-$	0.0443	512
	$K^{*0}K^{*-}$	0.0055	254
	$\phi\pi^-\pi^-\pi^+$	0.0088	182
	$\phi\pi^-\pi^0$	0.0061	127
$\eta\pi^+$, $\eta \to 3\pi$	$\phi\pi^-$	0.0101	258
	K^0K^-	0.0093	344
	$f_0(975)\pi^-$	0.0138	335
	$K^{*0}K^-$	0.0124	236
	$K^{*0}K^{*-}$	0.0018	135
	$\phi\pi^-\pi^-\pi^+$	0.0026	87
	$\phi\pi^-\pi^0$	0.0017	57

1. Charged track reconstruction efficiency. Since A was measured in the same experiment in final states containing three charged tracks, the contribution to the systematic error on ν_s is zero for the first three tracks; a relative uncertainty of $\Delta_{ij}^{(1)} = 1\%$ is used for each of the additional tracks.

2. Photon detection efficiency. An uncertainty $\Delta_{ij}^{(2)} = 2.5\%$ per photon is used to account for the calorimeter ribs and the barrel/endcap interface regions. Three of the D_s^+ decay modes used in this analysis, $\phi\pi^+\pi^0$, $\eta\pi^+$ ($\eta \to \pi^+\pi^-\pi^0$), and $\eta'\pi^+$ ($\eta' \to \gamma\rho^0$), yield a significant proportion of photons below 100 MeV. An additional contribution of 2.5% per γ is used for these modes. The γ detection errors are based on previous studies of $\psi(3770)$ data.[75]

3. TOF identification. The kaon identification criteria used for $D_s^+ \to \phi\pi^+\pi^0$ *vs.* $D_s^- \to \phi\pi^-\pi^0$, $\eta\pi^-$, and $\eta'\pi^-$ are also used in the measurement of A. The

Table 6.11 Detection efficiencies for Group 3 double tag modes.

Mode i	*Mode j*	ϵ_{ij}	$N_{ij}^{\rm mc}$
$\eta'\pi^+$, $\eta' \to \gamma\rho^0$	$\phi\pi^-$	0.0181	364
	K^0K^-	0.0182	529
	$f_0(975)\pi^-$	0.0275	528
	$K^{*0}K^-$	0.0248	370
	$K^{*0}K^{*-}$	0.0032	189
	$\phi\pi^-\pi^-\pi^+$	0.0043	115
	$\phi\pi^-\bar{\pi}^0$	0.0032	85
$\eta'\pi^-$, $\eta' \to \eta\pi\pi$	$\phi\pi^-$	0.0083	292
	K^0K^-	0.0078	399
	$f_0(975)\pi^-$	0.0118	396
	$K^{*0}K^-$	0.0101	264
	$K^{*0}K^{*-}$	0.0014	147
	$\phi\pi^-\pi^-\pi^+$	0.0022	105
	$\phi\pi^-\pi^0$	0.0012	55

TOF efficiency error cancels for $D_s^+ \to \phi\pi^+\pi^0$ *vs.* $\eta\pi^-$ and $\eta'\pi^-$; $\Delta_{ij}^{(3)} = 11\%$ is assumed in $D_s^+ \to \phi\pi^+\pi^0$ *vs.* $D_s^- \to \phi\pi^-\pi^0$.

4. Resonance mass cuts and definition of signal regions. The resonance cuts introduce no significant uncertainty on the efficiency, except for the $f_0(975)$. A systematic error $\Delta_{ij}^{(4)} = 3\%$ is included for each f_0 in the final state to account for the uncertainty on the line shape and width. In addition, the probability that an event will contribute to the $M(X)$ signal region has a 2% uncertainty in each double tag mode. This accounts for uncertainties in the mass resolution, the mass scale, and the D_s^+ mass.

5. Branching fractions of the ϕ, K^0, $f_0(975)$, K^*, π^0, η, η'. In each of the three groups of measurements, the error on ν_s from $B(\phi \to K^+K^-)$, $B(K^0 \to$

$\pi^+\pi^-$), $B(f_0 \to \pi^+\pi^-)$, $B(K^* \to K\pi)$, and $B(\pi^0 \to \gamma\gamma)$ is negligible or zero. The η and η' branching fractions contribute the following uncertainties: $D_s^+ \to \eta\pi^+$, $\eta \to \gamma\gamma$, $\Delta_{ij}^{(5)} = 1.0\%$; $D_s^+ \to \eta\pi^+$, $\eta \to \pi^+\pi^-\pi^0$, 2.1%; $D_s^+ \to \eta'\pi^+$, $\eta' \to \gamma\rho^0$, 4.7%; $D_s^+ \to \eta'\pi^+$, $\eta' \to \eta\pi^+\pi^-$, $\eta \to \gamma\gamma$, 3.8%.

6. Kinematic fit χ^2 cut. Since the errors on the track parameters were conservatively estimated using Bhabha scattering and dimuon events, no additional systematic error is applied.

The contributions to the uncertainty on ν_s are

$$\Delta\nu_s^{(k)} = \begin{cases} AB_{\phi\pi^+} \sum_{i,j} b_i b_j \epsilon_{ij} \Delta_{ij}^{(k)} & \text{(Group 1)}, \\ 2AB_{\eta\pi^+} \sum_i b_i \left(\epsilon_{\gamma\gamma,i}\, \Delta_{\gamma\gamma,i}^{(k)} + \epsilon_{3\pi,i}\, \Delta_{3\pi,i}^{(k)} \right) & \text{(Group 2)}, \\ 2AB_{\eta'\pi^+} \sum_i b_i \left(\epsilon_{\gamma\rho^0,i}\, \Delta_{\gamma\rho^0,i}^{(k)} + \epsilon_{\eta\pi\pi,i}\, \Delta_{\eta\pi\pi,i}^{(k)} \right) & \text{(Group 3)}, \end{cases}$$

for $k = 1, 2, \ldots, 5$.

The Monte Carlo statistical errors are

$$\Delta\nu_s^{(\mathrm{mc})} = \begin{cases} AB_{\phi\pi^+} \left[\sum_{i,j} (2 - \delta_{ij}) \frac{(b_i b_j \epsilon_{ij})^2}{N_{ij}^{\mathrm{mc}}} \right]^{\frac{1}{2}} & \text{(Group 1)}, \\ 2AB_{\eta\pi^+} \left[\sum_i b_i^2 \left(\frac{\epsilon_{\gamma\gamma,i}^2}{N_{\gamma\gamma,i}^{\mathrm{mc}}} + \frac{\epsilon_{3\pi,i}^2}{N_{3\pi,i}^{\mathrm{mc}}} \right) \right]^{\frac{1}{2}} & \text{(Group 2)}, \\ 2AB_{\eta'\pi^+} \left[\sum_i b_i^2 \left(\frac{\epsilon_{\gamma\rho^0,i}^2}{N_{\gamma\rho^0,i}^{\mathrm{mc}}} + \frac{\epsilon_{\eta\pi\pi,i}^2}{N_{\eta\pi\pi,i}^{\mathrm{mc}}} \right) \right]^{\frac{1}{2}} & \text{(Group 3)}, \end{cases}$$

where N_{ij}^{mc} is the number of reconstructed i *vs.* j events in the Monte Carlo sample [Tables 6.9–6.11].

These contributions are evaluated using the set of parameters $\mathbf{u}$ which maximizes the likelihood function at $B = B_{90}$. The errors are added in quadrature, and the branching fraction limit is inflated as follows:

$$\Delta\nu_s = \left[(\Delta\nu_s^{(1)})^2 + (\Delta\nu_s^{(2)})^2 + \cdots + (\Delta\nu_s^{(5)})^2 + (\Delta\nu_s^{(\mathrm{mc})})^2 \right]^{\frac{1}{2}},$$

$$B_{90} \leftarrow B_{90} \times \frac{\nu_s}{\nu_s - \Delta\nu_s}.$$

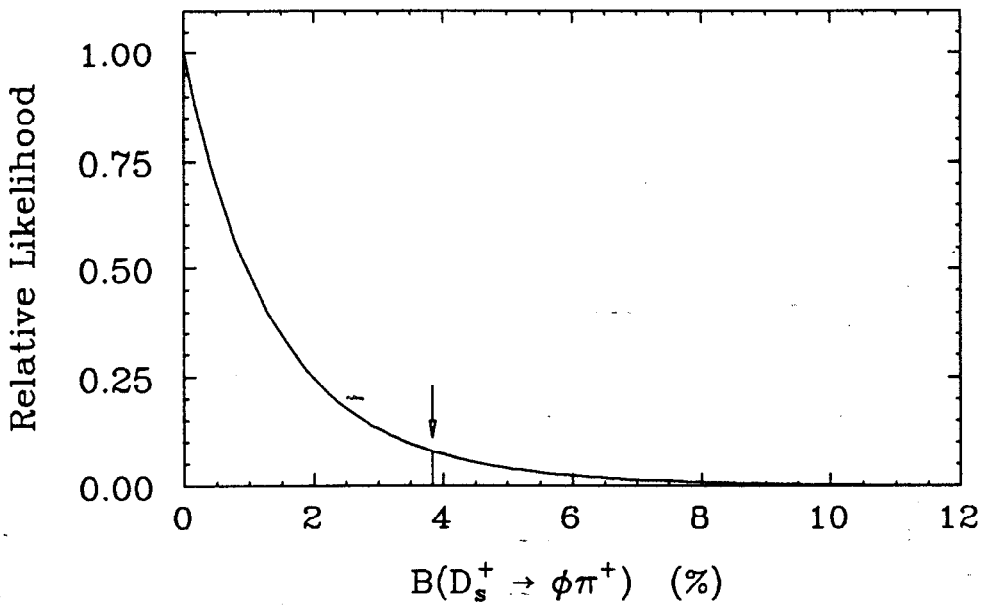

Figure 6.16 Group 1 likelihood function $\ell(B_{\phi\pi^+})$. The 90% CL point is indicated by the arrow.

Results

The total background contribution to the signal regions of Group 1 is predicted from the fit to Fig. 6.8(a) to be $\nu_b = 0.5$ events. With $\mathbf{u}$, $\mathbf{S}$, and ϵ_{ij} as given in Tables 6.8 and 6.9, and $n_{obs} = 0$, the likelihood function $\ell(B_{\phi\pi^+})$ shown in Fig. 6.16 is obtained, which yields $B_{90} = 3.8\%$. After including the systematic errors (7%) and Monte Carlo statistical errors (2%), the limit on the $D_s^+ \to \phi\pi^+$ branching fraction is

$$B_{\phi\pi^+} < 4.1\% \qquad (90\%\ \text{CL}).$$

Since $n_{obs} = 0$ the result does not depend on ν_b.

The background estimate for Group 2 is $\nu_b = 0.9$ events. The resulting likelihood function $\ell(B_{\eta\pi^+})$ is displayed in Fig. 6.17, with $B_{90} = 18\%$. After including the systematic errors (10%) and Monte Carlo statistical errors (1%), the upper limit on

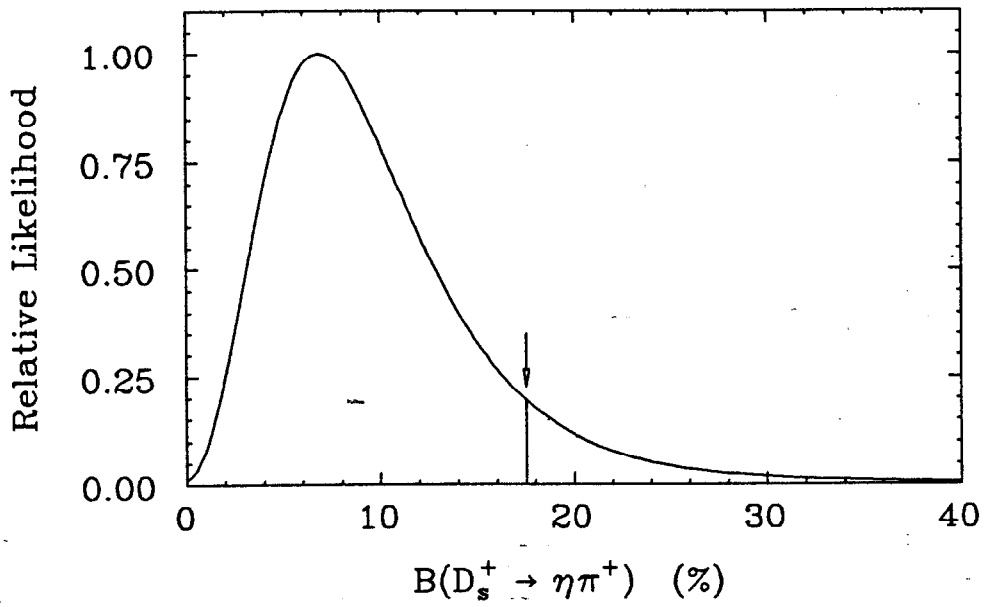

Figure 6.17 Group 2 likelihood function $\ell(B_{\eta\pi^+})$. The 90% CL point is indicated by the arrow.

the $D_s^+ \to \eta\pi^+$ branching fraction is

$$B_{\eta\pi^+} < 20\% \qquad (90\%\ \text{CL}).$$

The background prediction for the Group 3 signal regions is $\nu_b = 0.8$ events. The resulting likelihood function $\ell(B_{\eta'\pi^+})$ is shown in Fig. 6.18, with $B_{90} = 19\%$. After including the systematic errors (10%) and Monte Carlo statistical errors (1%), the upper limit on the $D_s^+ \to \eta'\pi^+$ branching fraction is

$$B_{\eta'\pi^+} < 22\% \qquad (90\%\ \text{CL}).$$

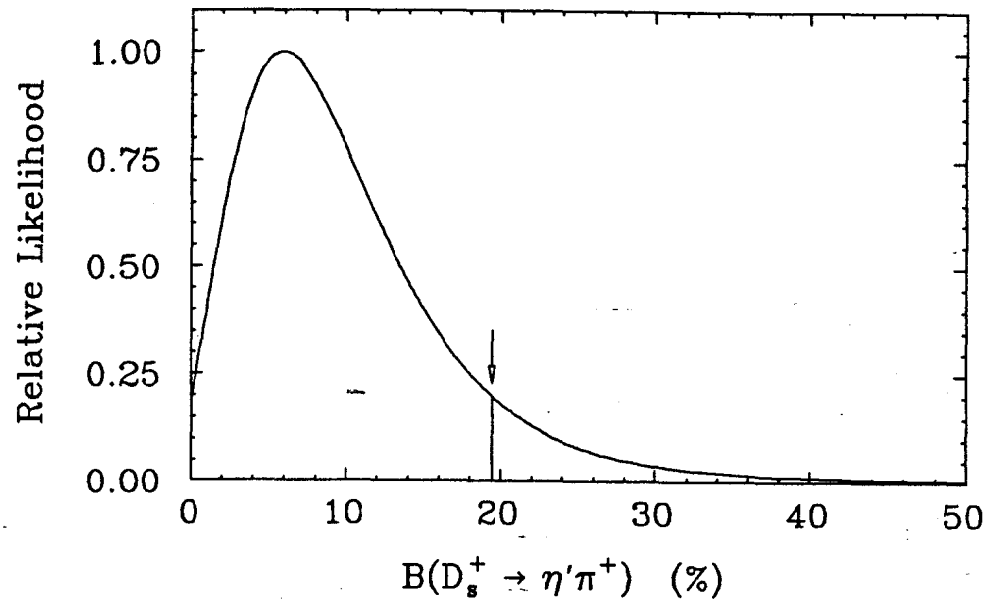

Figure 6.18 Group 3 likelihood function $\ell(B_{\eta'\pi^+})$. The 90% CL point is indicated by the arrow.

7
Summary and Conclusions

In summary, the reactions $e^+e^- \to D_s^{*\pm}D_s^{\mp}$, $D_s^+ \to \phi\pi^+$ and $\bar{K}^{*0}K^+$ have been studied, and limits on the absolute branching fractions for $D_s^+ \to \phi\pi^+$, $\eta\pi^+$, and $\eta'\pi^+$ have been established.

The reaction $e^+e^- \to D_s^{*\pm}D_s^{\mp}$ has been observed, with $D_s^+ \to \phi\pi^+$. The decay angular distributions observed are consistent with expectations for $J^P(D_s^*) = 1^-$ and $J^P(D_s) = 0^-$. The following results are obtained:

$$M(D_s) = 1972.4 \pm 3.7 \pm 3.7\,\mathrm{MeV}/c^2,$$

$$M(D_s^*) = 2111.3 \pm 2.1 \pm 2.8\,\mathrm{MeV}/c^2,$$

$$M(D_s^*) - M(D_s) = 141.9 \pm 2.1 \pm 3.3\,\mathrm{MeV}/c^2,$$

$$\Gamma(D_s^*) < 22\,\mathrm{MeV}/c^2 \quad (90\%\ \mathrm{CL}),$$

$$\frac{\sigma(e^+e^- \to D_s^+D_s^-)}{\sigma(e^+e^- \to D_s^{*+}D_s^- + D_s^{*-}D_s^+)} < 0.21 \quad (90\%\ \mathrm{CL}),$$

$$\sigma(e^+e^- \to D_s^{*+}D_s^- + D_s^{*-}D_s^+)B(D_s^+ \to \phi\pi^+) = 26 \pm 6 \pm 5\,\mathrm{pb}.$$

The D_s^* mass measurement agrees with earlier measurements which had considerably larger uncertainties. The more recent measurement by ARGUS[76] of the D_s^*-D_s mass difference is even more precise: $142.5 \pm 0.8 \pm 1.5\,\mathrm{MeV}/c^2$. The prediction of Reference 27 is in good agreement with experiment if the QCD scale parameter

Λ is taken to be around 120 MeV.

The decay $D_s^+ \to \bar{K}^{*0}K^+$ is also measured:

$$\sigma(e^+e^- \to D_s^{*+}D_s^- + D_s^{*-}D_s^+)B(D_s^+ \to \bar{K}^{*0}K^+) = 22 \pm 6 \pm 6\,\text{pb},$$

$$\frac{B(D_s^+ \to \bar{K}^{*0}K^+)}{B(D_s^+ \to \phi\pi^+)} = 0.84 \pm 0.30 \pm 0.22.$$

The world average for this ratio of branching fractions, 0.93 ± 0.11, is larger than the predicted values, 0.55[19] and 0.74,[77] although final state interactions are not accounted for, and other theoretical uncertainties are rather large.

No double tag events are observed, leading to the following upper limits at the 90% CL:

$$B(D_s^+ \to \phi\pi^+) < 4.1\%,$$

$$B(D_s^+ \to \eta\pi^+) < 20\%,$$

$$B(D_s^+ \to \eta'\pi^+) < 22\%.$$

The branching fraction for $D_s^+ \to \phi\pi^+$ is predicted to be approximately 3.5%,[19,77] although much smaller values are expected in some models.[78] The upper limit on $B(D_s^+ \to \phi\pi^+)$ is consistent with the values of 2–3% which are typically used in the interpretation of $B \to D_s$ measurements.

Appendix
Multiple Coulomb Scattering and Energy Loss Corrections

In this appendix I describe the corrections which are applied to charged track parameters and their covariances to account for multiple Coulomb scattering and energy loss in the material of the detector.

The energy loss formula[79] is a rough interpolation of data[80] for π's, K's, and p's; we assume that dE/dx is a function of β only, independent of particle species:

$$\Delta p = \begin{cases} \overline{\Delta p}_{\min} \sec\lambda \left(\frac{\beta}{0.94}\right)^{-2.74} & (\beta < 0.94) \\ \overline{\Delta p}_{\min} \sec\lambda & (\beta \geq 0.94) \end{cases} . \qquad \text{A.1}$$

Track parameters measured in the drift chamber are corrected for the average energy loss in each of the detector components listed in Table A.1, proceeding inward to the interaction point. The material is assumed to be arranged in thin cylinders at the indicated radii r. For each component the incident particle velocity β_{in} is determined from the integral equation

$$\int_{\beta_{\text{out}}}^{\beta_{\text{in}}} \left(\frac{\beta}{0.94}\right)^{-2.74} \gamma^3 d\beta = \frac{\overline{\Delta p}_{\min}}{M} \sec\lambda,$$

where β_{out} is the velocity after passage through the material and where M is the assumed particle mass. The integral is evaluated numerically for $\beta = 0$ to 0.94; the results are saved in a lookup table which can be rapidly interpolated to apply the

Table A.1 Summary of material amounts for the inner detector components; r is the mean distance from the interaction point, $\overline{\Delta p}_{\rm min}$ is the mean momentum loss for a minimum ionizing track and X/X_0 the material amount in radiation lengths, for a radial trajectory through the detector at $\theta = \pi/2$. The quantity αt is defined in the text.

	r (m)	$\overline{\Delta p}_{\rm min}$ (MeV)	$\Sigma\alpha t$ (MeV)	X/X_0
Beam pipe	0.077	0.44	0.018	0.0040
Trigger chamber (layer 1)	0.115	0.49	0.020	0.0071
Inner wall of main drift chamber	0.145	0.13	0.005	0.0017
Gas and wires (layers 2–5)	0.409	0.16	0.007	0.0050
Total		1.22	0.046	0.0178

energy loss corrections. For $\beta \geq 0.94$ equation A.1 is used to obtain $\beta_{\rm in}$. The track parameter corrections are then

$$\kappa \leftarrow \frac{\sqrt{1-\beta_{\rm in}^2}}{M\beta_{\rm in}} \sec\lambda,$$

$$\phi \leftarrow \phi + 0.3Bqr(\kappa_{\rm in} - \kappa_{\rm out}),$$

$$\xi \leftarrow \xi + \frac{0.3Bqr^2}{2}(\kappa_{\rm in} - \kappa_{\rm out}),$$

where B is the magnitude of the solenoidal magnetic field and q is the charge of the incident particle in units of the positron charge.

The size of the momentum loss fluctuations are estimated using[⋆]

$$\sigma_p = \frac{2\alpha t}{\beta^3} \sec\lambda,$$

where $\alpha = (0.153\,{\rm MeV}/c)\,Z/A\,{\rm g}^{-1}\,{\rm cm}^2$, and t is the material thickness in $\mathrm{g\,cm^{-2}}$. The covariance matrix element $\sigma^2_{x_i x_j}$ ($x_i = \{\phi, \kappa, s, \xi, \eta\}$) from the helix fit is then

⋆ The fluctuations are non-Gaussian; the variance of the dimensionless λ variable in Ref. 81 is taken to be $\sigma^2 = 4$ for the calculation of corrections to the track parameter covariance matrix.

increased by the amount

$$\Delta\sigma^2_{x_i x_j} = \sigma_p^2 \frac{\partial x_i}{\partial p} \frac{\partial x_j}{\partial p},$$

where

$$\frac{\partial \phi}{\partial p} = -\frac{0.3Bqr}{p^2} \sec\lambda,$$

$$\frac{\partial \kappa}{\partial p} = -\frac{1}{p^2} \sec\lambda,$$

$$\frac{\partial \xi}{\partial p} = -\frac{0.3Bqr^2}{2p^2} \sec\lambda,$$

$$\frac{\partial s}{\partial p} = \frac{\partial \eta}{\partial p} = 0.$$

Multiple Coulomb scattering introduces an uncertainty on the track direction which is given approximately by[5]

$$\sigma^2_{\rm mcs} \cong \frac{(14.1\,{\rm MeV}/c)^2}{\beta^2 p^2} \frac{X}{X_0}, \qquad \text{A.2}$$

where X/X_0 is the number of radiation lengths of material traversed, and where the particle trajectory is projected onto a plane containing the incident track momentum direction.

Material encountered before the first drift chamber measurement is treated as follows. For $\beta < 0.94$ we account for the change in β within the material by evaluating

$$\sigma^2_{\rm mcs} = \frac{(14.1\,{\rm MeV})^2}{M\overline{\Delta p}_{\rm min}} \frac{X}{X_0} \int_{\beta_{\rm out}}^{\beta_{\rm in}} \left(\frac{\beta}{0.94}\right)^{2.74} \beta^{-4}\gamma\, d\beta;$$

for very fast tracks equation A.2 is again used. Assuming the track z information is derived from the stereo layers, the non-zero covariance matrix contributions (at the

point of closest approach to the z axis) are

$$\Delta\sigma^2_{\phi\phi} = \sigma^2_{\rm mcs} \sec^2\lambda,$$
$$\Delta\sigma^2_{\phi\xi} = \sigma^2_{\rm mcs}\, r \sec^2\lambda,$$
$$\Delta\sigma^2_{\xi\xi} = \sigma^2_{\rm mcs}\, r^2 \sec^2\lambda,$$
$$\Delta\sigma^2_{ss} = \sigma^2_{\rm mcs} \sec^4\lambda,$$
$$\Delta\sigma^2_{s\eta} = \sigma^2_{\rm mcs}\, r \sec^4\lambda,$$
$$\Delta\sigma^2_{\eta\eta} = \sigma^2_{\rm mcs}\, r^2 \sec^4\lambda.$$

The drift chamber wires and gas must be treated differently from material traversed before the first drift chamber cells. For material between the first and last track measurements, corresponding to a path length L_{xy} in the xy-plane, the contributions to the covariance matrix elements for the track parameters *at the location of the first measurement* are:

$$\Delta\sigma^2_{\phi\phi} = 0.21\,\sigma^2_{\rm mcs} \sec^2\lambda,$$
$$\Delta\sigma^2_{\phi\kappa} = 0.19\,\sigma^2_{\rm mcs} \frac{q\sec^2\lambda}{0.3BL_{xy}},$$
$$\Delta\sigma^2_{\kappa\kappa} = 1.37\,\sigma^2_{\rm mcs} \frac{\sec^2\lambda}{(0.3BL_{xy})^2},$$
$$\Delta\sigma^2_{\phi\xi} = 0.014\,\sigma^2_{\rm mcs}\, L_{xy} \sec^2\lambda,$$
$$\Delta\sigma^2_{\kappa\xi} = 0.0084\,\sigma^2_{\rm mcs} \frac{q\sec^2\lambda}{0.3B},$$
$$\Delta\sigma^2_{\xi\xi} = 0.0012\,\sigma^2_{\rm mcs}\, L^2_{xy} \sec^2\lambda,$$
$$\Delta\sigma^2_{ss} = \frac{1}{3}\,\sigma^2_{\rm mcs} \sec^4\lambda.$$

The coefficients are determined by Monte Carlo simulation, assuming straight tracks which pass through a gas and are measured in 25 equally-spaced planes. The coefficients vary slowly with the number and spacing of the measurements.[82] In the last formula $\sigma^2_{\rm mcs}$ is evaluated for the amount of material between the z measurements

in layers 4 and 6. This accounts for the independent scattering in ϕ and in λ. The error matrix thus obtained is "swum" to the point of closest approach to the z-axis using the formulae of reference 83, which may be approximated as follows:

$$\Delta\sigma'^2_{x_i x_j} = \sum_{k,\ell} \frac{\partial x'_i}{\partial x_k} \frac{\partial x'_j}{\partial x_\ell} \Delta\sigma^2_{x_k x_\ell},$$

$$\frac{\partial\phi'}{\partial\phi} = \frac{\partial\kappa'}{\partial\kappa} = \frac{\partial s'}{\partial s} = \frac{\partial\xi'}{\partial\xi} = \frac{\partial\eta'}{\partial\eta} = 1,$$

$$\frac{\partial\phi'}{\partial\kappa} = -0.3Bqa_{xy},$$

$$\frac{\partial\xi'}{\partial\phi} = -a_{xy},$$

$$\frac{\partial\xi'}{\partial\kappa} = 0.3Bqa^2_{xy}/2,$$

$$\frac{\partial\eta'}{\partial s} = a_{xy};$$

a_{xy} is the signed xy path length of the swim (< 0 for swimming back to interaction point). The other $\partial x'_i/\partial x_k$ are zero.

References

1. S. Weinberg, Phys. Rev. Lett. **19**, 1264 (1967).

2. A. Salam, in *Elementary Particle Theory*, edited by N. Svartholm (Almquist and Wiksells, Stockholm, 1969), p. 367.

3. S.L. Glashow, J. Iliopoulos, and L. Maiani, Phys. Rev. D **2**, 1285 (1970).

4. M. Kobayashi and T. Maskawa, Prog. Theor. Phys. **49**, 652 (1973).

5. G.P. Yost *et al.* (Particle Data Group), Phys. Lett. B **204**, 1 (1988).

6. N. Cabibbo, Phys. Rev. Lett. **10**, 531 (1963).

7. G. 't Hooft, Nucl. Phys. B **33**, 173 (1971); **35**, 167 (1971).

8. G. Arnison *et al.*, Phys. Lett. B **122**, 103 (1983); M. Banner *et al.*, Phys. Lett. B **122**, 476 (1983); G. Arnison *et al.*, Phys. Lett. B **126**, 398 (1983); P. Bagnaia *et al.*, Phys. Lett. B **129**, 130 (1983).

9. D.J. Gross and F. Wilczek, Phys. Rev. D **8**, 3633 (1973); H.D. Politzer, Phys. Rep. **14C**, 129 (1974).

10. B.J. Bjørken and S.L. Glashow, Phys. Lett. **11**, 255 (1964).

11. J.J. Aubert *et al.*, Phys. Rev. Lett. **33**, 1404 (1974); J.-E. Augustin *et al.*, Phys. Rev. Lett. **33**, 1406 (1974).

12. G.S. Abrams *et al.*, Phys. Rev. Lett. **33**, 1453 (1974).

13. G. Goldhaber *et al.*, Phys. Rev. Lett. **37**, 255 (1976); I. Peruzzi *et al.*, Phys. Rev. Lett. **37**, 569 (1976); J.E. Wiss *et al.*, Phys. Rev. Lett. **37**, 1531 (1976).

14. M.K. Gaillard, B.W. Lee, and J.L. Rosner, Rev. Mod. Phys. **47**, 277 (1975).

15. R. Brandelik *et al.*, Phys. Lett. B **70**, 132 (1977); **80**, 412 (1979).

16. R. Partridge *et al.*, Phys. Rev. Lett. **47**, 760 (1981).

17. A. Chen *et al.*, Phys. Rev. Lett. **51**, 634 (1983).

18. B. Guberina *et al.*, Phys. Lett. **89B**, 111 (1979); Y. Koide, Phys. Rev. **D20**, 1739 (1979); G. Altarelli and L. Maiani, Phys. Lett. **118B**, 414 (1982).

19. M. Bauer, B. Stech and M. Wirbel, Z. Phys. C **34**, 103 (1987). Revised values of $a_1 = 1.2$ and $a_2 = -0.5$ are taken from B. Stech, preprint HD-THEP-87-18, 1987 (unpublished).

20. I.I.Y. Bigi and M. Fukugita, Phys. Lett. B **91**, 121 (1980).

21. H. Albrecht *et al.*, Phys. Lett. B **158**, 525 (1985); C. Bebek *et al.*, Phys. Rev. Lett. **56**, 1893 (1986); R.M. Baltrusaitis *et al.*, Phys. Rev. Lett. **56**, 2136 (1986).

22. J. Donoghue, Phys. Rev. D **33**, 1516 (1986).

23. J.C. Anjos *et al.*, Phys. Rev. Lett. **62**, 125 (1989).

24. H. Albrecht *et al.*, Phys. Lett. B **195**, 102 (1987).

25. J.C. Anjos *et al.*, FERMILAB-Pub-89/23-E (1989).

26. M. Frank and P.J. O'Donnell, Phys. Lett. B **159**, 174 (1985).

27. K. Igi and S. Ono, Phys. Rev. D **32**, 232 (1985).

28. M. Althoff *et al.*, Phys. Lett. B **136**, 130 (1984).

29. H. Albrecht *et al.*, Phys. Lett. B **146**, 111 (1984).

30. M. Derrick *et al.*, Phys. Rev. Lett. **54**, 2568 (1985).

31. H. Albrecht *et al.*, Phys. Lett. B **153**, 343 (1985).

32. R. Bailey *et al.*, Phys. Lett. B **139**, 320 (1984).

33. H. Aihara *et al.*, Phys. Rev. Lett. **53**, 2465 (1984).

34. B. Richter, SLAC-PUB-780 (1970).

35. J. Voss *et al.*, SLAC-PUB-965 (1971); B. Richter, SLAC-PUB-1128 (1972).

36. K. Wille, SLAC/AP-9 (1984).

37. G. Fischer, private communication.

38. D. Bernstein *et al.*, Nucl. Instrum. Methods **226**, 301 (1984).

39. J. Adler *et al.*, Nucl. Instrum. Methods **A276**, 42 (1989).

40. J. Roehrig *et al.*, Nucl. Instrum. Methods **226**, 319 (1984).

41. J.S. Brown *et al.*, Nucl. Instrum. Methods **221**, 503 (1984).

42. W. Toki *et al.*, Nucl. Instrum. Methods **219**, 479 (1984); R. Fabrizio *et al.*, Nucl. Instrum. Methods **227**, 220 (1984).

43. J.J. Thaler *et al.*, IEEE Trans. Nucl. Sci. **NS-30**, 236 (1983).

44. J. Adler *et al.*, Phys. Lett. B **208**, 152 (1988).

45. M.W. Coles *et al.*, Phys. Rev. D **26**, 2190 (1982).

46. C. Simopoulos, Ph.D thesis, U. of Illinois (1987).

47. E. Eichten *et al.*, Phys. Rev. D **21**, 203 (1980); W. Lockman, Mark III Memorandum, 30 March 1987.

48. J.J. Becker, Ph.D. thesis, U. of Illinois (1984).

49. T. Freese, private communication.

50. M. Burchell, Mark III Memorandum 10/88-5 (1988).

51. J.J. Becker *et al.*, Nucl. Instrum. Methods **A235**, 502 (1985).

52. L. Parrish, Mark III Memorandum 7/88-4 (1988).

53. F.A. Berends *et al.*, Acta Phys. Pol. **B14**, 413 (1983); S. Jadach and Z. Was, Acta Phys. Pol. **B15**, 1151 (1984); **B16**, 483(E) (1985); Y.-S. Tsai, Phys. Rev. D **4**, 2821 (1971); **13**, 771(E) (1976).

54. R. Kleiss, computer code `BHABHA`, `VIRSOF`, `REPI` (1982); F.A. Berends *et al.*, Nucl. Phys. **B68**, 541 (1974); H. Burkhardt, TASSO Note 192 (1981).

55. T. Sjöstrand, Comput. Phys. Commun. **39**, 347 (1986).

56. J.C. Anjos *et al.*, Phys. Rev. Lett. **58**, 1818 (1987).

57. S. Barlag *et al.*, CERN-EP/88-103 (1988).

58. M.P. Alvarez *et al.*, CERN-EP/88-148 (1988).

59. G.T. Blaylock *et al.*, Phys. Rev. Lett. **58**, 2171 (1987).

60. A weighted average of $M(D_s) = 1971.4 \pm 1.7\,\mathrm{MeV}/c^2$ was obtained from M. Aguilar-Benitez *et al.* (Particle Data Group), Phys. Lett. **170B**, 1 (1986), and H. Becker *et al.*, Phys. Lett. B **184**, 277 (1987).

61. F. Berends and R. Kleiss, Nucl. Phys. B **178**, 141 (1981). The cross section for $e^+e^- \to D_s^{*\pm}D_s^{\mp}$ is assumed to be constant between threshold and 4.14 GeV. The size of the systematic error introduced by this assumption is estimated by removing the initial-state radiation entirely.

62. H. Albrecht *et al.*, Phys. Lett. B **179**, 398 (1986).

63. W. Toki, in *Proceedings of the Fourteenth SLAC Summer Institute on Particle Physics,* 1986, edited by E.C. Brennan, SLAC-312 (1987).

64. J. Adler *et al.*, Phys. Lett. **196B**, 107 (1987).

65. J.C. Anjos *et al.*, Phys. Rev. Lett. **60**, 897 (1988).

66. G. Moneti, in *Proceedings of the XXIII International Conference on High Energy Physics,* Berkeley, 1986, edited by S. Loken (World Publishing, Singapore, 1987).

67. W. Braunschweig *et al.*, Z. Phys. C **35**, 317 (1987).

68. H. Albrecht *et al.*, Phys. Lett. B **187**, 425 (1987).

69. J.A. McKenna, Ph.D. thesis, University of Toronto, 1987.

70. S. Abachi *et al.*, ANL-HEP-CP–86-71 (1986).

71. J. Adler *et al.*, SLAC-PUB-4952 (1989).

72. G. Wormser, talk at XXIV Rencontres de Moriond: Progress in Hadron Physics, March 1989.

73. G. Wormser *et al.*, Phys. Rev. Lett. **61**, 1057 (1988).

74. I.E. Stockdale, in proceedings of the International Symposium on Production and Decay of Heavy Flavors, Stanford, September 1987.

75. J. Hauser, Ph.D. thesis, California Institute of Technology, 1985.

76. H. Albrecht *et al.*, Phys. Lett. B **207**, 349 (1988).

77. B.Yu. Blok and M.A. Shifman, Yad. Fiz. **45**, 211 (1987); **45**, 478 (1987); **45**, 841 (1987); **46**, 1310 (1987) [Sov. J. Nucl. Phys. **45**, 135 (1987); **45**, 301 (1987); **45**, 522 (1987); **46**, 767 (1987)].

78. S.P. Rosen, Phys. Lett. B **218**, 353 (1989).

79. R. Schindler, Mark III Memorandum, 4 February 1983; D. Hitlin, Mark III Memorandum 6/83-4 (1983).

80. W.P. Trower, B.H. Willis, C.V. Stableford, eds., report UCRL-2426 (1966).

81. L. Landau, J. Phys. U.S.S.R. **8**, 201 (1944).

82. R.L. Gluckstern, Nucl. Instrum. Methods **24**, 381 (1963).

83. A.D. Johnson and G.H. Trilling, LBL Note TG-301 (1979).